https://ntrs.nasa.gov/search.jsp?R=19950008198 2020-06-16T10:21:14+00:00Z

NASA-CR-197025

MCAT Institute
Annual Report

Numerical Simulation of the SOFIA Flowfield

Stephen P. Klotz

July 1994

NCC 2-636

MCAT Institute
3933 Blue Gum Drive
San Jose, CA 95127

(NASA-CR-197025) NUMERICAL SIMULATION OF THE SOFIA FLOWFIELD Annual Report (MCAT Inst.) 75 p

N95-14612

Unclas

G3/02 0030164

NUMERICAL SIMULATION OF THE SOFIA FLOWFIELD

Abstract

This report provides a concise summary of the contribution of computational fluid dynamics (CFD) to the SOFIA (Stratospheric Observatory for Infrared Astronomy) project at NASA Ames and presents results obtained from closed- and open-cavity SOFIA simulations. The aircraft platform is a Boeing 747SP and these are the first SOFIA simulations run with the aircraft empennage included in the geometry database. In the open-cavfity run the telescope is mounted behind the wings. Results suggest that the cavity markedly influences the mean pressure distribution on empennage surfaces and that 110-140 decibel (db) sound pressure levels are typical in the cavity and on the horizontal and vertical stabilizers. A strong source of sound was found to exist on the rim of the open telescope cavity. The presence of this source suggests that additional design work needs to be performed in order to minimize the sound emanating from that location. A fluid dynamic analysis of the engine plumes is also contained in this report. The analysis was part of an effort to quantify the degradation of telescope performance resulting from the proximity of the port engine exhaust plumes to the open telescope bay.

Nomenclature

C_{force}	=	force coefficient, $2F/\rho_\infty V_\infty^2$
C_{mom}	=	moment coefficient, $2Mo/\rho_\infty V_\infty^2 S\ell$
C_p	=	pressure coefficient, $2(p-p_\infty)/\rho V_\infty^2$
d	=	plume width
F	=	aerodynamic force
ℓ	=	characteristic length, one(1) ft
L	=	length of the aircraft fuselage
M	=	Mach number
Mo	=	moment
p	=	static pressure
psd	=	power spectral density
spl	=	sound pressure level
S	=	surface area
T	=	temperature
V	=	(streamwise) velocity
(x',z')	=	engine plume coordinate system (x´ is the streamwise coordinate, measured from the tip of the center cone and z´ is the radial coordinate)
x''	=	distance from the leading edge, measured parallel to the longitudinal axis of the fuselage

Greek symbols

α	=	temperature ratio

β	=	plume spread angle
γ	=	ratio of specific heats, 1.4
δ	=	plume spread rate
η	=	normalized radial dimension
λ	=	velocity ratio
ρ	=	atmospheric density
σ	=	plume spread parameter

Superscript

$'$	=	fluctuating (turbulent) value

Subscripts

c	=	hot engine exhaust
cf	=	potential core of the fan plume
ch	=	chord
cl	=	centerline
cp	=	potential core of the hot engine exhaust plume
f	=	fan
fc	=	fan to hot engine exhaust (ratio)
fwhm	=	full-width-at-half-maximum
if	=	free-stream to fan exhaust (ratio)
max	=	maximum
sej	=	single-equivalent jet
th	=	thermal
(x,y,z)	=	aircraft coordinate system (x is measured along the longitudinal axis of the fuselage from the nose of the aircraft to the tail, y is measured from the fuselage out the starboard wing, and z points in the vertical direction)
(x''', y''', z''')	=	telescope coordinate system; x''', y''', and z''' pass through the center of the telescope air bearing and are parallel to the aircraft coordinates x, y, and z, respectively
∞	=	free-stream
0.5	=	location of the half-maximum

Introduction

This report describes computational fluid dynamics (CFD) research in the SOFIA (Stratospheric Observatory For Infrared Astronomy) project at the NASA Ames Research Center. The research has entailed using CFD technology for simulating the flow field in the vicinity of SOFIA. Computations ultimately will be used to assess effects of the open telescope cavity on the fuel consumption, in-flight safety, and fatigue of the aircraft platform (a Boeing 747). An important part of the work completed to date has involved validating CFD capability in transonic cavity-flow applications by comparing computational results to wind-tunnel experiments. CFD has also been used to evaluate whether mounting the

telescope in a cavity behind the wings is technically viable, rather than forward of the wings and behind the cockpit. The latter was the first configuration proposed for SOFIA.

This report contains results of open and closed-cavity SOFIA simulations at 747SP cruise flight conditions. The telescope is mounted behind the wings and the simulations are the first to be completed in the SOFIA project with the empennage included in the geometry database. As noted in subsequent discussion, the impact of the open telescope cavity on the flow field in the vicinity of the horizontal and vertical stabilizers is of importance to design engineers concerned with control of the aircraft platform and fatigue of empennage surfaces.

Background

Since it began five years ago the SOFIA CFD program has been tasked with accomplishing four objectives. The first entailed developing and validating CFD capability in transonic cavity-flow applications and has been largely accomplished. The second involved simulating the flow field in the vicinity of SOFIA in order to assess effects of the open telescope cavity on the sensitivity and resolution of the infrared telescope (i.e., its so-called seeing) and on aircraft performance (i.e., its control, safety, and fuel consumption). The first part of this objective has been largely met as well. The third objective involves addressing technical issues regarding effects of the open cavity on fatigue of the aircraft and effects of different cavity-door designs on telescope performance and stability of the cavity-port shear layer. This objective has not been accomplished and will remain the focus of future effort. The last objective follows immediately from the first three. Once it becomes operational, SOFIA will be based at NASA Ames. During the projected twenty-year lifetime of the SOFIA program, a validated design tool will be needed to assess effects of design changes which might be contemplated for improving telescope seeing or for enhancing aircraft performance. Since wind-tunnel experiments are much more costly and time-consuming to run than computer simulations, CFD is the logical choice for that design tool.

SOFIA was one of fifteen projects chosen in 1991 by the National Research Council as crucial to continued progress in astronomical science during the next decade. SOFIA is planned as a successor to the Kuiper Airborne Observatory (KAO) currently based at Ames and will consist of an infrared, 2.5 meter Cassegrain telescope mounted in a Boeing 747SP or Boeing 747-200. When it becomes operational, the capability of SOFIA will be significantly greater than the KAO's and SOFIA will offer advantages which earth- and space-based instruments cannot. Specifically, SOFIA will operate at an altitude above most of the absorbing water vapor in the atmosphere. Consequently, SOFIA will be capable of collecting data which is not measurable from the earth's surface. Furthermore, SOFIA will function as a mobile observatory which can be used to collect data from transient astronomical events at remote locations around the world. Although a space-based telescope would undoubtedly possess more sensitivity, SOFIA's telescope will cost considerably

less and have a larger diameter mirror with greater resolution. Moreover, SOFIA will be considerably less expensive to service, since maintaining, upgrading, and modifying its instrumentation will be comparatively easier, less costly, and less time-consuming. As has the design of the KAO, the design of SOFIA will allow installation of state-of-the-art instruments throughout the operating life of the aircraft, and will provide a test platform for new instrumentation which may eventually be used on space-based platforms.

Nevertheless, the use of an aircraft as an observation platform creates a number of technically challenging problems. Solid materials typically have a very narrow transmittance bandwidth for infrared radiation. Consequently, since the spectrum of radiation from the sky and celestial sources is very broad, the SOFIA telescope will be mounted in a fuselage cavity which will be uncovered and open to the atmosphere when data is being collected. The effect of the open cavity on the in-flight performance and safety of the aircraft, as well as on the optical resolution and pointing accuracy of the instrument, were technical questions which arose in the preliminary design of SOFIA. Fortunately, the design criteria for optimizing aircraft performance are the same as those for optimizing telescope performance. Performance of the telescope will be enhanced by a cavity configuration which results in a stable, attached cavity-port shear layer. Aircraft fatigue will also be reduced by such a design, and control of the aircraft will be improved as well.

The issue of an aft telescope mount arose in 1991 as part of an effort to identify a less expensive, yet technically viable aircraft cavity and telescope design. In the SOFIA design first proposed, the telescope was mounted forward of the wings immediately behind the aircraft cockpit. However, mounting the telescope behind the wings has distinct cost advantages because an aft mount will require a simpler cavity door design, installation of one less pressure bulkhead in the aircraft, and fewer modifications of aircraft control and power systems. Nevertheless, technical problems which are not severe in a forward-mount configuration may be important and difficult to overcome with a telescope mounted farther aft. The dynamic steadiness of the cavity-port shear layer and acoustic levels in the cavity are influenced by the thickness of the fuselage boundary layer upstream of the cavity aperture. Since the boundary layer is much thicker and more turbulent behind the wings than forward of them, the shear layer across the cavity port is also thicker and more turbulent in an aft-mount configuration. Consequently, shear-layer turbulence levels (as measured by turbulent kinetic energy) will be greater and light passing through the thicker layer will be diffracted more. Most of the SOFIA design effort completed to date has presumed that a Boeing 747SP would be the aircraft platform for the SOFIA telescope. However, if the telescope is mounted behind the wings, the SP may not be suitable for this purpose. There are two reasons. First, an adverse pressure gradient exists on the SP fuselage immediately downstream of the cavity and a region of separated flow is evident in the aft-cavity CFD simulations run to date. Second, the cavity aperture on an SP cannot be fitted with an external door because movement of the door is restricted by the aircraft's vertical stabilizer. An SP can be fitted with an internal cavity door, but an internal door restricts space in the cavity and decreases the allowable focal

length of the telescope. These issues have recently led the SOFIA project to consider the Boeing 747-200 as a possible platform for SOFIA.

To date CFD has been an integral part of a general test and analysis program in the SOFIA project. CFD has provided a unique tool for evaluating design concepts and has provided estimates of unsteady telescope loads, which were not measured in the 1990 wind-tunnel experiments conducted at NASA Ames. A second set of experiments was begun in June, 1994. The focus of these experiments was the aft-mount telescope configuration and a comparison of the flow field characteristics in the vicinity of the telescope cavity mounted on both the 747SP and 747-200 aircraft platforms.

Wind-tunnel experiments were run in 1990 on a sting-mounted, clipped-wing aircraft model and were used to validate NASA Ames CFD capabilities in the SOFIA project. The experiments focused on investigating resonance characteristics of the open telescope bay in a forward-mount configuration and were tasked specifically with obtaining a design which results in a stable shear layer across the cavity port at transonic Mach numbers. A stable shear layer reduces density fluctuations in the optical path of the telescope and aero-acoustic and aerodynamic fatigue resulting from pressure fluctuations in and around the open telescope bay. Moreover, effects of flow-field oscillations on the empennage and, consequently, control of the aircraft are undoubtedly mitigated when the shear layer is stable. A cavity-port ramp design which generates a stable shear layer was identified in the experiments and numerical simulations captured the essential characteristics of the flow-field resonance generated by that design, thereby validating the CFD effort. The ramp will probably need to be modified when the telescope is mounted behind the wings, in part because the direction of flow over the cavity will be different in that configuration. Moreover, the installation of an aperture door will undoubtedly impact the design of the ramp.

The experiments in 1990 measured only surface pressures in the telescope cavity, but CFD can be used to examine the physics of the flow in a more detailed manner than experiments can. Indeed, numerical simulations provide information which experiments generally cannot - integrated pressure data, from which aerodynamic loads on the telescope can be computed, temperature and density data in the cavity and across the cavity-port shear layer, by which thermal and density effects on the aero-optics of the SOFIA telescope may be examined, and fluctuating pressures in and around the telescope cavity, by which aero-acoustic fatigue of the aircraft may be quantified. (CFD has already provided estimates of unsteady telescope loads, which were not measured in the experiments.) CFD can therefore be expected to have a major impact on the future direction and progress of the SOFIA program, since experiments are costly and cannot be planned or scheduled without significant lead times.

The cavity-port design identified in the 1990 experiments has been used in all subsequent numerical and experimental work in the SOFIA project. However, an important result of the open-cavity simulation described in this report points

to the need for design modifications in order to eliminate a strong source of acoustic energy on the rim of the open telescope bay.

Geometry

Boeing provided NASA with a complete 747SP surface definition in the fall of 1992. The data included the geometry of the aircraft empennage, which had not been available before. All of the CFD simulations completed prior to that time were run with a sting-mounted fuselage and geometry derived from sources secondary to Boeing, i.e., a CAD definition of the Microcraft wind-tunnel model used in the 1990 experiments, a coarse 747-200 surface definition which has been used in panel code simulations, United Technologies Pratt and Whitney JT9D engine sketches, and NASA blueprints. The Boeing data was used to verify location, length, and angle-of-attack of the wings, the definition of the wing-root fairings, and fuselage taper in the region behind the wings and in front of the empennage where the cavity is to be located in the aft-mount configuration. Data was not used to refine the surface definition of the wingtips and nacelle and engine geometries, which were flow-through in the data bases previously supplied to NASA, but which were modified for powered conditions from information in Boeing and Pratt and Whitney sketches. These parts of the surface definition are not of critical interest to the design of the cavity. Unfortunately, the surface definitions provided by Boeing included only unloaded wing geometry. As a result, the loaded wing geometry of the panel code definition was used in the simulations described in this report, but no attempt was made to verify that the loading was appropriate for 747SP cruise conditions.

Atwood[1,2,3,4] used GRIDGEN2D and HYPGEN software to construct the surface and volume grids in his SOFIA simulations and most of these grids did not need to be modified for use in the CFD simulations of this report. Atwood subsequently constructed empennage grids from the Boeing data obtained in 1992, and used them to start a closed-cavity computation on a half-model with symmetry about the $y = 0$ plane through the longitudinal axis of the fuselage. This simulation was not completed, but its solution was used to initialize the flow field in the closed-cavity simulation of this report.

The closed- and open-cavity CFD simulations of this report were run on a full aircraft platform. The empennage surfaces on the starboard side of the aircraft were generated by reflecting Atwood's half-model grids about the $y = 0$ plane.

Method

The two simulations described in this report were run at SOFIA cruise conditions ($M = 0.85$ at an altitude of 41,000 feet). The engines were powered and simulations included the engine inflow and outflow boundary conditions used by Atwood[3], for which Pratt and Whitney provided engine thrusts and mass flow rates through the fan and hot engine cores. The Pratt and Whitney data were also used to compute tail cone surface temperatures.

The simulations were run on the Cray C-90 supercomputers in the Central Computing and Numerical Aerodynamic Simulation Facilities at NASA Ames. OVERFLOW was used to compute the solutions. OVERFLOW contains implicit, approximately-factored algorithms and has been used to run all SOFIA cavity-flow simulations completed to date. The diagonalized Beam-Warming numerical scheme and the Baldwin-Lomax turbulence model in OVERFLOW were used in all calculations. The effects of turbulence in the cavity-port shear layer were simulated by the Baldwin-Lomax shear-layer model, which has been described by Atwood[3].

The closed-cavity simulation was run on a computational domain containing thirty-eight grids and approximately 1.1×10^6 grid points. The domain in the open-cavity simulation consisted of forty-five grids and approximately 2.5×10^6 grid points. An overset grid interface routine (PEGASUS) was used to establish inter-grid communication and compute the grid-boundary interpolation coefficients required by OVERFLOW.

The open-cavity simulation was run time-accurately. The closed-cavity solution provided initial conditions at all points in the computational domain, with the exception of the flow field in the cavity. The cavity flow field was initialized by Atwood's[3,4] simulations, which were run on cavity grids identical to those in this computation. The time step was approximately 1.35×10^{-4} seconds in this run. A data record one(1) second long, on which oscillations with frequencies less than two(2) hertz cannot be resolved, requires approximately 7.4×10^3 time steps. Since the CPU cost to run OVERFLOW is approximately 7×10^{-6} sec per time step per grid point, a one-second data record requires approximately thirty-five C-90 CPU hours to compute solutions on domains containing 2.5×10^6 grid points.

If they exist, oscillations with frequencies of O(1) hertz are of particular concern to design engineers in the SOFIA project. Telescope motions excited by flow field phenomena at these frequencies can be eliminated by proper design of the tracking mechanisms. However, a one-second data record is too short for computing reliable statistics of motions at these frequencies.

Results

Closed-Cavity Simulation

The simulations reported by Atwood[3,4] were used to initialize the closed-cavity run, which was the first SOFIA CFD computation to include the aircraft empennage in the geometry database. The simulation was run approximately 3.8×10^3 steps after initialization until the C_p distributions on the fuselage had achieved steady-state equilibrium. Fig. 1 contains plots of experimental and computed, steady-state C_p distributions on the top, port side, and bottom of the fuselage during flight. The experimental data was provided by Boeing[5] and used by Atwood[3,4] to validate CFD results on a sting-mounted aircraft without empennage. However, the data was probably taken from measurements at an altitude lower than the 41,000 foot cruise altitude of the SOFIA CFD simulations.

For the purpose of plotting, the starboard side C_p distribution is identical to that on the port side of the aircraft and is not shown in Fig. 1. However, C_p distributions on empennage stabilizer surfaces were slightly asymmetrical and suggest that the simulation had not reached steady-state everywhere in the computational domain. Nevertheless, it is clear that CFD reproduces very well the pressure distribution on the fuselage and, in particular, in the empennage region, where one would expect the flow field to be strongly influenced by an open telescope cavity.

Plume Fluid Dynamics

If the telescope is mounted behind the wings, infrared radiation (IR) from the hot exhaust plumes of the port engines may scatter onto the primary mirror of the instrument and degrade its performance. This problem was the subject of an independent investigation by the SOFIA project, which was tasked with quantifying the degradation, if any. Part of the investigation involved experiments with the Shuttle Carrier Aircraft, which is a modified Boeing 747-100 powered by Pratt and Whitney JT9D engines - the engines most likely to be used to power SOFIA as well. Results of the investigation suggested that the IR emission from engine exhausts would not significantly degrade telescope performance, except possibly at very low telescope elevation angles (Dinger et al.[6]).

Attention in this report will focus on the exhaust plume of the port outboard engine, because thermal IR scattering from this engine to the telescope mirror is significantly greater than that from the inboard engine. In the experiments the exhaust plumes of both inboard and outboard engines were imaged by IR cameras mounted in the NASA Ames Lear Jet, which flew alongside the Shuttle Carrier (Dinger et al.[6]).

The brightness distribution of the jet exhaust is dictated by the mixing and subsequent cooling of the gases in the plume behind the aircraft. Empirical correlations suggested by Antonia and Bilger[7], Morris[8], Lau[9], and Tanna and Morris[10] were used to construct a simple model describing the evolution of the plumes, ie., their spread rate, length of potential core, and mean and turbulent temperature distributions. Model predictions were then compared with measurements of peak temperatures, plume full-width-at-half-maximum d_{fwhm}, and an estimate of the length of the hot potential core. More recently, results from the closed-cavity CFD simulation were also compared with predictions of the model. All of the comparisons serve to validate CFD and the empirical model. The validation provides a rational basis for their future use should questions again arise with regards to effects of SOFIA's engine emissions on performance of the telescope.

Appendix A contains a summary of the equations used in the empirical formulation of the model and Figs. 2 and 3 contain sketches of the model's construct. Mixing of the fan and hot exhausts along the tail cone was neglected and. the jet at the downstream tip of the cone was assumed to consist of a hot,

circular core of area equal to the area of the nozzle exit, surrounded by a concentrically circular jet of area equivalent to the exhaust area of the fan. The radii r_c and r_f of the concentric disks are depicted in Fig. 2. Velocities and temperatures at this location ($x' = 0$) were assumed to be equal to the corresponding velocities V_f and V_c, and temperatures T_f and T_c, of the fan and engine exhausts, respectively, for which data was available from the experiments or was provided by Pratt and Whitney. This construct provided an upstream boundary condition for the model.

Downstream of the potential core the plume evolves as a fully-developed jet with radial temperature and velocity distributions which are approximately Gaussian, but which can be represented by a sinusoidal distribution suggested by Morris[10]. The thrust of the fully-developed jet was required to be the same as the thrust of the coannular jet at the $x' = 0$ upstream boundary (Tanna and Morris[10]). This requirement leads to the concept of the so-called single-equivalent jet (Ko and Kwan[11]), which provided an estimate of the cross-sectional area of the jet at the end of the potential core. The spread rate correlations in Appendix A cannot be used to estimate the size of the fully-developed jet at the end of the potential core, because the region between x'_{cf} and x'_{cp}, where the fan and hot engine exhaust plumes mix, is not self-preserving. The spread rate correlations strictly apply to self-preserving jets, only.

Potential core lengths

The radial spreading of the plume and the erosion of its constant-velocity and constant-temperature inner region are results of the intense mixing of the fan and hot engine exhaust gases, which occurs over considerable distance downstream of the engine nozzle. The centerline temperature decreases downstream of the potential core, whose length is a function of Mach number in the core gases and fan and engine temperatures, velocities, and sizes. The model makes use of a correlation suggested by Tanna and Morris[10] to estimate the lengths x'_{cf} and x'_{cp} of the fan and hot exhaust potential cores.

A potential core length x'_{cp} of 7.7 meters is predicted by the model for the nominal flight conditions of the Shuttle Carrier experiments, most of which were conducted at $M = 0.6$ and an altitude of 35,000 feet. (Some data were collected at an altitude of 26,000 feet, but no comparisons were made with these measurements.) This value corresponds well with the 7-8 meter length apparent in the peak short-wave band (SWB) and long-wave band (LWB) temperature distributions reported by Dinger et al.[6].

Plume width

In the region of the potential core, which ends at $x'/r_c = 17.1$, approximately (Fig. 4), the model predicts a nearly-constant plume width d_{fwhm} of approximately 0.9 meters for the conditions of the Shuttle Carrier experiments. This result agrees reasonably well with the LWB average of 0.7 meters, which is

also virtually constant in the same region. Farther downstream the plume spreads at an approximate angle of 7°, but spreading is not apparent in the experimental data.

CFD predictions of plume width from the closed-cavity simulation (at M = 0.85 and an altitude of 41,000 feet) were also compared to the measurements. Results are plotted in Fig. 5. The difference in flight conditions has little effect on the results and agreement between the measurements and CFD predictions is good.

Fig. 6 contains model and CFD predictions of plume width at SOFIA cruise conditions. According to the model, the potential core ends at x'/r_c = 18.0 (x'_{cp} = 8.1 meters). Moreover, the model overpredicts the width of the plume, particularly in the fully-developed region downstream of this location. Nevertheless, the growth rate of the plume (i.e., the rate of change of the plume's width with respect to streamwise distance x') predicted by CFD is similar to that predicted by the model in this regime.

Peak inferred temperature

The peak temperature in the plume occurs along the jet centerline at any downstream location. In the potential core the temperature is constant and equal to 322°C, the static temperature of the hot engine exhaust. LWB measurements are in good agreement with this prediction, but SWB measurements are about 100°C less. The centerline temperature decreases as distance increases downstream of the potential core, but the decrease in the data is much more rapid. For example, a centerline (peak) temperature of 300°C is predicted at a downstream distance of 12 meters, whereas the LWB data suggests that the peak temperature is less than 100°C at the same location.

Peak rms temperature fluctuations

Estimates of rms temperature fluctuations in the plume can be deduced from the well-known Crocco relationship (Cebeci and Smith[12]) and the experimental data of Antonia and Bilger[7], Lau[9], and Smith and Hughes[13]. Appendix A contains an expression for the maximum rms temperature fluctuations in a fully-developed, heated jet. The temperature fluctuations are expressed as a function of the velocity fluctuations, which are maximum at $z' \approx z'_{0.5}$. According to experiment[7,13], $(\sqrt{V'^2})_{max} \approx 0.3(V_{cl} - V_\infty)$ at this location. Moreover, at SOFIA cruise conditions, $f_T \approx 1$. Consequently, $(\sqrt{T'^2})_{max} \approx 0.3(T_{cl} - T_\infty)$. No attempt was made to deduce temperature fluctuations from the image data, although it is possible to do so. Nevertheless, an estimate of $(\sqrt{T'^2})_{max}$, from which density fluctuations can be determined, is important in analysis of telescope seeing.

Plume centerline velocity and temperature distributions

Figs. 7 and 8 contain model and CFD predictions of velocity and temperature on the centerline of the exhaust plume at SOFIA cruise conditions. The centerline values represent maxima in the plume at any streamwise location x'. The model assumes that centerline values of velocity and temperature in the potential core are essentially undiminished from the values in the $x' = 0$ plane. However, at locations farther downstream, the model predicts a much faster rate of centerline decay

Radial velocity and temperature distributions

Figs. 9 through 14 contain plots of radial velocity and temperature distributions in the fully-developed region of the plume at SOFIA cruise conditions. Downwash from the wings distorts the CFD distributions, which would otherwise be symmetric about the $z' = 0$ axis. The CFD predictions shown were computed in the vertical $x'z'$ plane.

Tail Cone Temperatures

All of the SWB and most LWB images in the experimental data were saturated in the vicinity of the engine tail cone downstream of the exhaust nozzle. As a result, the infrared emission of the cone and plume in this region could not be determined directly from most of the data. However, the brightness of the tail cone is a function of its surface temperature, which can be estimated using empirical heat transfer correlations. It is necessary only to assume thermodynamic equilibrium before computing the convective and radiative heat transfer between the cone and hot exhaust gas flowing over it.

Radiative heat transfer rates were calculated assuming an emissivity of 1.0 for the cone and 0.1 for the exhaust gas. Empirical flat-plate correlations suggested by White[14] were used to compute skin friction and corresponding convective heat transfer coefficients. Reynolds number in the calculation of skin friction was based on distance from the turbine exit plane upstream of the engine exhaust nozzle. It is possible to correct coefficients computed from flat-plate correlations for the axisymmetric geometry of the tail cone. The correction involves computing an effective Reynolds number based on experiment (White[14]). However, the correction has negligible effect on surface temperatures in these calculations and was not implemented. It is also possible to account for effects of compressibility (Mach number) on convection, but this correction is insignificant at the conditions of the Shuttle Carrier experiments.

Table I contains the results of calculations for the outboard engine on the port side of the aircraft. Event numbers correspond to changes in engine throttle settings in the experiments. The surface temperatures are significantly higher than those obtained from LWB images and plotted in Fig. V-6 of Dinger et al.[6]. Moreover, surface temperatures deduced from the images are significantly lower (by 80°C, approximately) than the static temperatures of the hot exhaust gas at the exit of the engine nozzle. This result seems implausible, in part

because the core temperature of the exhaust remains undiminished near the jet centerline well downstream of the tail cone.

There is no reason to believe that the discrepancy between measured and computed surface temperatures is the result of poor assumptions or inaccuracies in the heat transfer calculations. For example, neglecting radiation emitted by the exhaust gas has little effect on computed temperatures, since the exhaust gas radiation is a small part of the energy budget. Moreover, a gas emissivity greater than 0.1 results in higher computed temperatures and a larger discrepancy between experimental and calculated values.

If radiation or convection were entirely neglected in the calculations, surface temperatures would be well approximated by the adiabatic wall temperature in the different events. The latter temperatures are listed in Table I and are greater than the surface temperatures computed. However, radiative heat transfer is not negligible at the conditions of the Shuttle Carrier experiments and, in the absence of convection, computed and measured temperatures match only if the exhaust gas emissivity is greater than 1.0. This requirement is physically unrealistic.

Nevertheless, empirical relationships for convective heat transfer coefficients often correlate poorly with available data and it is necessary to consider the possibility that inaccuracies in the calculation of this coefficient are responsible for the difference between measured and calculated tail cone temperatures. The temperatures deduced from the LWB images are correct only if convective heat transfer coefficients are approximately one order of magnitude smaller than the computed ones. Coefficients of such small magnitude are not consistent, however, with available heat transfer data. Consequently, one must conclude that the surface temperatures measured in the Shuttle Carrier experiments are inaccurate.

Open-Cavity Simulation

The open-cavity simulation was initialized from the closed-cavity run on all grids in the computional domain, with the exception of grids in the cavity and in the immediate vicinity of the cavity aperture. The open-cavity simulation of Atwood (1993), which was run on cavity grids identical to those in this simulation, provided the initial flow field for the cavity and cavity aperture grids. After initialization the simulation was run time-accurately for approximately 1.5 seconds (real time) before data was collected. At SOFIA cruise conditions, a 747SP travels approximately seven(7) of its lengths in this period of time. This distance was deemed sufficient for generating a state of statistical quasi-equilibrium in the unsteady flow field in and around the open cavity and on empennage surfaces. The simulation was run another 1.1 seconds of real time during which data was collected for analysis. The 1.1-second data record is sufficiently long for studying the essential characteristics of the unsteady flow, but is too short for calculating accurate statistics of flow field phenomena in a frequency range of a few hertz. Unsteady phenomena in this range are of particular importance to the SOFIA project. They will influence the design of the

telescope air bearing and tracking mechanisms and impact estimates of fatigue loading when the cavity is open to the atmosphere.

Figs. 15 through 22 contain sketches of the aircraft and show locations of the telescope cavity, cross-sections through the cavity and empennage surfaces, and points where spectra of sound pressure levels have been computed. The athwartships plane AA through the fuselage and cavity in Figs. 15 and 16 is shown in Fig. 20. Plane HH through the fore-and-aft symmetry plane of the telescope in Fig. 20 is shown in Fig. 21. Fig. 22 depicts the location of points on the forward and aft cavity bulkheads. The cross-sectional outline of the telescope shown in this figure serves to orient the view (cf. Fig. 20).

Empennage C_p Distributions

The C_p distributions in Figs. 23 through 25 were computed from 1.1-second averages of pressures at points on empennage surfaces. The distributions were then interpolated onto cross-sections parallel to the longitudinal axis of the fuselage. The interpolation was necessary because cross-sections in the computational domain are not generally oriented parallel to the fuselage axis. Cross-sections on the vertical stabilizer are nearly parallel to the axis, but C_p distributions were interpolated on that surface as well, even though interpolation was not as important a consideration.

Surface C_p distributions in planes BB and CC through the vertical stabilizer (Figs. 15 and 18) are shown in Fig. 23. Not surprisingly, there is asymmetry in the distributions when the telescope cavity is open. In plane BB the influence of the open cavity is predominately at mid-chord and farther aft. The influence in plane CC is farther forward. The asymmetry in the distributions suggests that the open cavity affects the flow field over the entire span, and that effects are largely undiminished at cross-sections well away from the fuselage. Moreover, the lower pressure on the starboard side of the stabilizer suggests that a starboard side force is imparted to it, thereby creating moments which yaw the aircraft to port and roll it to starboard.

Fig. 24 contains a plot of C_p distributions in planes EE and GG through the port and starboard horizontal stabilizers (cf. Figs. 17 and 19). The effect of the open cavity is small on the pressure distribution on the lower surface, but pronounced on that of the upper surface, particularly near mid-chord. The C_p distributions in planes DD and FF of Figs. 17 and 19 are plotted in Fig. 25. The asymmetry of the pressure coefficients on the port and starboard stabilizers is less pronounced in these cross-sections than on sections EE and GG farther inboard. Pressures on the upper surfaces of planes FF and GG on the starboard side of the aircraft are lower than pressures on planes DD and EE on the port side. This result suggests that a port roll is imparted to the aircraft when the telescope cavity is open.

Cavity and Telescope Sound Pressure Levels

Figs. 26 through 44 contain plots of sound pressure spectra on empennage surfaces and in the telescope cavity. The figures depict power spectral density (psd) of the sound pressure level (in decibels), defined by

$$spl(db) = 20\log_{10}\frac{\sqrt{p'^2}}{2(10^{-5})},$$

as a function of frequency, where $\sqrt{p'^2}$ is the root-mean-square (rms) static pressure, in N/m^2.

The spectra were computed from 1638 points stored at approximately 6.8×10^{-4} second intervals in the 1.1-second data record. The record was zero-padded to a length of 2048 points and a Welsh window applied[15]. The Nyquist frequency was 739 hz. Hann, Parzen, and Bartlett windowing functions were also applied to the data in order to determine what effect, if any, different windows had on the spectral representations of the data. The different functions affected some spectra at frequencies greater than 100 hz. However, the energy content in sound pressure fluctuations at these frequencies is typically several orders of magnitude smaller than the energy content of the lower frequency fluctuations of primary interest in the design of the SOFIA telescope. Moreover, in the frequency range where the different windowing functions had some effect on spectra, numerical dissipation is significant (Atwood[3]).

Spectra at points PH1, PH2, PH3, and PH4 on the upper surface of the port horizontal stabilizer (cf. Figs. 17 and 19) are shown in Fig. 26. The sound pressure level is greatest at PH4 and least at PH3, but greater at PH1 than PH2, as is evident from examining the values tabulated in Table 2. This result is surprising. One might expect the sound pressure level to be greatest at PH3, which is farther upstream and closer to the cavity than the other points. However, PH4 is located more directly downstream of the cavity and PH3 is shielded from sound emanating from sources deep in the cavity, unlike PH1 and PH2.

Spectra at points SH1, SH2, SH3, and SH4 on the upper surface of the starboard horizontal stabilizer are shown in Fig. 27. The sound pressure level is greatest at SH4 and least at SH3 (cf. Table 2). Not surprisingly, the sound pressure levels are greater on the port stabilizer than on the starboard stabilizer. This result is obvious from examining Table 2 and is made clear by replotting the spectra in Figs. 26 and 27 in pairs which represent mirror images of one another with respect to the centerline of the fuselage. Spectra at points PH1 and SH1 are replotted in Fig. 28, at points PH2 and SH2 in Fig. 29, at points PH3 and SH3 in Fig. 30, and at points PH4 and SH4 in Fig. 31.

Spectra of sound pressure levels on the vertical stabilizer are plotted in Figs. 32 through 35. As is evident from the values listed in Table 2, sound pressure levels on the port side of the stabilizer are highest at VP4 and lowest at VP1,

and higher at VP3 than VP2. Point VP3 is the least shielded of all the points from sound sources deep in the cavity and the sound pressure level at this point is higher than at VP2 and VP3. However, VP4 is closer than VP3 to the unsteady wake of the cavity. Not surprisingly, sound pressure levels are higher on the port side of the stabilizer than at image points on the starboard side. This result is evident from examining the spectra and values tabulated in Table 2.

Figs. 16 and 20 through 22 contain sketches of the cavity environment and locations of points where spectra of sound pressure levels have been computed. (Plane HH in Fig. 20 is depicted in Fig. 21.) The spectra are plotted in Figs. 36 through 44 and Table 3 contains a tabulation of the sound pressure levels at the various points.

The sound pressure levels at points T2 and T3 on the primary mirror of the telescope are identical and the spectra in Fig. 36 are similar. Although fluctuating pressures are responsible for structural loads on surfaces, as well as sound pressure levels, the similar spectra and identical sound pressure levels at these points do not necessarily suggest that there is negligible asymmetric loading of the primary mirror. A phase relationship between fluctuations at these points would suggest asymmetry in the loading.

Points S1 and T1 are located on the secondary and tertiary mirrors of the telescope, respectively. Spectra of sound pressure levels at these points are plotted in Fig. 37. The sound pressure level on the tertiary mirror is slightly higher than on the secondary mirror, even though T1 is shielded from sound sources on the cavity aft ramp in the vicinity of points C4 and A3. Wave reflections in the azimuth tube of the instrument may be responsible for this result.

Spectra at T1 and T4 and shown in Fig. 38. The sound pressure level on the base of the telescope, which is shielded from sound sources in the cavity-port shear layer is identical to that at points T2 and T3 on the primary mirror (cf. Table 2).

Spectra of sound pressure levels at points C3 and C4 on the aft ramp of the cavity are plotted in Fig. 39. The sound pressure level is higher at C3 and the power spectrum at that point indicates a significant contribution from a broad frequency band with peak at approximately 80 hz. Fig. 40 contains a plot of spectra at the center of the aft ramp (point C4). Spectra from the simulation reported by Atwood[3] and from the wind-tunnel experiments conducted at NASA Ames in 1990 are also plotted. Atwood scaled the experimental data, which were taken with the telescope bay mounted forward of the wings, to the flight conditions of the CFD simulations. However, neither the wind-tunnel model nor the geometry in Atwood's simulation contained the aircraft empennage. A frequency peak at 110 hz exists in the experimental data and Atwood's simulation; the peak is not evident when the empennage is included in the geometry.

Spectra of sound pressure levels at points A1, A2, A3, A4, and A5 in Fig. 16 are contained in Figs. 41 through 43. Point A1 is located on the fuselage slightly upstream of the edge of the telescope cavity. Point A4 is located on the fuselage and downstream of the cavity. Points A2, A3, and A5 are located on the cavity rim. The sound pressure level at point A1 is, not surprisingly, lower than at the other points on the fuselage and rim of the cavity (cf. Table 3). The sound pressure levels and spectra at points A3 and A4 (Fig. 42) are similar and exhibit the broad-band structure evident in the spectrum at point C3 (Fig. 39) in the vicinity of 80 hz. The spectra at points A2 and A5 are plotted in Fig. 43. The spectrum at A5 also exhibits the broad-band peak at 80 hz. However, the spectrum at A2 contains very energetic peaks at 100 and 200 hz, the latter of which is a harmonic of the first. A significant source of sound thus exists on the edge of the cavity where A2 is located. As shown in Fig. 20, the edge of the cavity is sharp in that region and the sound spectrum at A2 suggests that this edge is in an impingement region, unlike the opposite edge in the vicinity of A5, which is characterized by a markedly different spectrum. Further analysis should focus on determining flow patterns over the fuselage in the vicinity of the cavity when it is open to the atmosphere. Doing so may reveal whether an open cavity induces upwash over the fuselage behind the wings and the manner in which the geometry of the cavity edge in the vicinity of point A2 should be modified in order to eliminate the strong source of sound there.

Examination of the spectra in Fig. 44 reveals that the sound pressure level at point C2 on the cavity aft bulkhead is higher than at C1 on the forward bulkhead. Moreover, the mean pressure is higher at C2 than at C1, as indicated by the time history of normalized pressure in Fig. 45. This result has an important implication for loads on the telescope, as discussed in the next subsection.

Telescope Loads

Figs. 46 and 47 contain plots of the time histories of integrated force and moment coefficients, respectively, on the telescope and Table 4 contains a summary of the mean and root-mean-square loads (forces and moments) computed from the data record. The lift, drag, and side forces on the telescope are components of force in the aircraft *(x,y,z)* frame of reference. Moments and moment coefficients are referenced with respect to the (x''', y''', z''') coordinate axes, which are parallel to the aircraft axes, but which pass through the center of the telescope air bearing. SOFIA design engineers reference telescope moments with respect to axes through the air bearing, which is a counter-weight mechanism mounted forward of the instrument in the aircraft. The bearing isolates the telescope bay from the pressurized sections of the aircraft and must support all loads on the telescope, including the weight of the instrument when the aircraft is on the ground. The center of the bearing is located on the $y = 0$ symmetry plane, 10" forward of the forward bulkhead of the cavity and 6" above the longitudinal axis of the fuselage.

The forces tabulated in Table 4 are small and drag is in the upstream direction. This result is consistent with the fact that pressure is higher on the aft bulkhead

of the cavity than on the forward bulkhead (Fig. 45). Power spectra of fluctuating forces are contained in Fig. 48. In all spectra a peak containing significant energy occurs between 25 and 30 hz, approximately. A peak with much less energy occurs near 80 hz. Spectra of moments are plotted in Fig. 49. Significant energy occurs in spectral peaks of the pitch and yaw fluctuating moments near 30 hz.

Conclusion

This report contains a brief history of the computational fluid dynamics effort in the SOFIA project and the results of two CFD simulations. Comparisons with experiment demonstrate that CFD reproduces well the C_p distribution on the aircraft fuselage in the vicinity of the empennage, where effects of an open telescope cavity on aircraft fatigue and control are likely to be pronounced. Comparisons with measurements from infrared images of the Shuttle Carrier engine exhaust plumes demonstrate that CFD is capable of providing good estimates of plume size near the engine exits. CFD provided a better estimate of the size of the plume than did a simple model of plume dynamics constructed from empirical correlations. Nevertheless, the computational resources required by the latter model are very small and it can be used to generate approximate solutions when approximations are deemed sufficient. For example, the model might be used to calculate plume temperatures in stray-light analyses.

An open-cavity simulation provided estimates of sound pressure levels on empennage surfaces and in the open telescope cavity. The presence of a source of significant acoustic energy on the cavity rim suggests that the cavity aperture should be redesigned in the vicinity of the source. The simulation also provided estimates of telescope loads and moments. Aerodynamic forces on the telescope are small and drag is in the upstream direction. This result is consistent with pressure levels in the cavity. Significant energy exists near 30 hz in all spectra of the fluctuating forces and in the spectra of fluctuating yaw and pitch moments.

The work described in this report has supported a national program of scientific importance. As has been discussed, there are a number of technical issues which need to be addressed in the SOFIA project and for which CFD has proven to be an important design tool. Indeed, since wind-tunnel experiments are time-consuming to prepare for and expensive to run, CFD will likely remain the pre-eminent design tool available to engineers during the lifetime of the SOFIA program.

References

1. Atwood, C.A., Navier-Stokes simulations of unsteady transonic flow phenomena, NASA TM 103962, August, 1992.

2. Atwood, C.A. and VanDalsem, W., A numerical study of complex cavity flows via the Navier-Stokes equations, Paper 324, 11th Australasian Fluid Mechanics Conference, Hobart, Australia, 14-18 December, 1992.

3. Atwood, C.A., Selected computations of transonic cavity flows, 1993 ASME Fluids Engineering Conference, Washington DC, 20-24 June, 1993.

4. Atwood, C.A., Unsteady fluid and optical simulation of transonic aero-windows, Paper AIAA-93-3017, AIAA 24th Fluid Dynamics, Plasmadynamics, and Lasers Conference, Orlando, FL, 6-9 July, 1993.

5. 747SP cruise drag investigation program, Boeing Rpt. D6-34246, 1976.

6. Dinger, A.S., Dunham, E.W., Erickson, E.F., Klotz, S.P., Kock, D., and Yee, R., Evaluation of jet-exhaust emission scattering for the aft telescope configuration on SOFIA, SOFIA project internal report, NASA Ames Research Center, 1 October, 1992.

7. Antonia, R.A. and Bilger, R.W., The heated round jet in a coflowing stream, AIAA Jour., 14(11), 1541-1547, 1976.

8. Morris, P.J., Turbulence measurements in subsonic and supersonic axisymmetric jets in a parallel stream, AIAA Jour., 14(10), 1468-1475, 1976.

9. Lau, J.C., Mach number and temperature effects on jets, AIAA Paper 78-1152, 1978.

10. Tanna, H.K. and Morris, P.J., The noise from normal-velocity-profile coannular jets, Jour. Sound and Vibration, 98(2), 213-234, 1985.

11. Ko, N.W.M and Kwan, A.S.H., The initial region of subsonic coaxial jets, Jour. Fluid Mech., 73(2), 305-332, 1976.

12. Cebeci, T. and Smith, A.M.O., Analysis of Turbulent Boundary Layers, Academic Press, New York, 1974.

13. Smith, D.J. and Hughes, T., Some measurements in a turbulent circular jet in the presence of a co-flowing free stream, The Aeronautical Quarterly, 28, 185-196, 1977.

14. White, F., Viscous Fluid Dynamics, McGraw Hill Book Co., New York, 1974.

15. Press, W.H., Teukolsky, S.A., Vetterling, W.T., and Flannery, B.P., Numerical Recipes in FORTRAN, 2nd Ed., Cambridge University Press, Cambridge, UK,, 1992.

Table 1 Tail Cone Surface Temperatures

event	exhaust gas static temperature (°C)	adiabatic wall temperature (°C)	tail cone temperature (°C)
5	272	336	290
11	266	328	285
3,6,9,12	322	421	357

Table 2 Empennage Sound Pressure Levels

	point	sound pressure level (db)
vertical stabilizer		
	VP1	110.
	VP2	122.
	VP3	129.
	VP4	131.
	VS1	99.
	VS2	103.
	VS3	112.
	VS4	122.
port horizontal stabilizer		
	PH1	127.
	PH2	125.
	PH3	120.
	PH4	134.
starboard horizontal stabilizer		
	SH1	118.
	SH2	120.
	SH3	109.
	SH4	128.

Table 3 Telescope Cavity Sound Pressure Levels

	point	sound pressure level (db)
cavity walls		
	C1	111.
	C2	124.
cavity aft ramp		
	C3	141.
	C4	129.
telescope primary mirror		
	T2	116.
	T3	116.
telescope secondary mirror		
	S1	111.
telescope tertiary mirror		
	T1	114.
telescope base		
	T4	116.
cavity aperture		
	A1	114.
	A2	140.
	A3	135.
	A4	129.
	A5	133.

Table 4 Telescope Forces and Moments*

	force (lbf)	moment (ft-lbf)
F_x	-28.5±21.6	
F_y	83.1±32.1	
F_z	8.53±12.7	
$Mo_{x'''}$		-195.±23.8
$Mo_{y'''}$		204.±127.
$Mo_{z'''}$		776.±232.

* F_x, F_y, F_z drag, side force, and lift in aircraft coordinates (x,y,z)

$Mo_{x'''}$, $Mo_{y'''}$, $Mo_{z'''}$ roll, pitch, and yaw moments about the center of the telescope air bearing; the (x''',y''',z''') coordinates are obtained from the (x,y,z) coordinate system by translation

Appendix A

Empirical Equations Governing the Growth of Coaxial Jet Plumes

Potential core lengths (cf. Fig. 2):

$$x'_{cp} / 2r_c = \frac{(4.2 + 1.1M_c{}^2)\alpha_{fc}{}^{0.2}}{1 - 0.92\lambda_{fc}} - 2.4\lambda_{fc}$$

$$x'_{cf} / 2r_c = \frac{(4.2 + 1.1M_f{}^2)\alpha_{if}{}^{0.2}}{1 - 0.92\lambda_{if}} - 2.4\lambda_{if}$$

where M_c and M_f are the Mach numbers of the hot engine and turbofan exhausts, respectively, and

$$\lambda_{fc} = V_f / V_c$$
$$\alpha_{fc} = T_f / T_c$$
$$\lambda_{if} = V_\infty / V_f$$
$$\alpha_{if} = T_\infty / T_f$$

Plume centerline temperature and velocity ratios:

$$T_{cl} / T_c = 1 - \exp\left[1.4 / (1 - x' / x'_{cp})\right]$$
$$V_{cl} / V_c = 1 - \exp\left[1.4 / (1 - x' / x'_{cp})\right]$$

Plume spread rates:

$$\delta_c = \sqrt{\pi} / \sigma_c$$
$$\delta_f = \sqrt{\pi} / \sigma_f$$
$$\delta_{sej} = \sqrt{\pi} / \sigma_{sej}$$
$$\delta_{th} = 1.4\delta_{sej}$$

where δ_{th} is the spread rate of the thermal plume in a single-equivalent jet

$$\beta_c = \tan^{-1}\delta_c$$

$$\beta_f = \tan^{-1}\delta_f$$

$$\beta_{sej} = \tan^{-1}\delta_{sej}$$

$$\beta_{th} = \tan^{-1}\delta_{th}$$

where, if $\lambda_{fc} \le 0.8$,

$$\sigma_c = \frac{10.0}{(1-0.29M_c{}^2)\left[1+0.5(M_c{}^2-1)(T_c/T_f-1.4)^2\right](1-0.92\lambda_{fc})}$$

$$\sigma_f = \frac{10.0}{(1-0.29M_f{}^2)\left[1+0.5(M_f{}^2-1)(T_f/T_\infty-1.4)^2\right](1-0.92\lambda_{if})}$$

$$\sigma_{sej} = \frac{10.0}{(1-0.29M_c{}^2)\left[1+0.5(M_c{}^2-1)(T_c/T_\infty-1.4)^2\right](1-0.92\lambda_{ic})}$$

or, if $\lambda_{fc} > 0.8$,

$$\sigma_c = \frac{10.0}{(1-0.29M_c{}^2)\left[1+0.5(M_c{}^2-1)(T_c/T_f-1.4)^2\right]}$$

$$\sigma_f = \frac{10.0}{(1-0.29M_f{}^2)\left[1+0.5(M_f{}^2-1)(T_f/T_\infty-1.4)^2\right]}$$

$$\sigma_{sej} = \frac{10.0}{(1-0.29M_c{}^2)\left[1+0.5(M_c{}^2-1)(T_c/T_\infty-1.4)^2\right]}$$

Single-equivalent jet radius:

$$r_{sej} = \sqrt{1+\frac{r_f{}^2T_cV_f{}^2}{r_c{}^2T_fV_c{}^2}}$$

Radial velocity and temperature distributions (fully-developed jet):

$$\frac{V-V_\infty}{V_{cl}-V_\infty} = 0.5\left[1-\sin\frac{\pi\eta}{2}\right], \qquad -1 \le \eta \le 1$$

$$\frac{T-T_\infty}{T_{cl}-T_\infty} = 0.5\left[1-\sin\frac{\pi\eta}{2}\right], \qquad -1 \le \eta \le 1$$

where

$$\eta = (z' - z'_{0.5}) / z'_{0.5}$$

Root-mean-square temperature distribution (fully-developed jet):

$$\frac{\sqrt{T'^2}}{T_{cl} - T_\infty} = f_T \frac{\sqrt{V'^2}}{V_{cl} - V_\infty}, \qquad -1 \le \eta \le 1$$

where

$$f_T = \frac{T_{cl}}{V_{cl}} \frac{V_{cl} - V_\infty}{T_{cl} - T_\infty} \left[\frac{V_{cl}}{T_{cl}} \frac{T_{cl} - T_\infty}{V_{cl} - V_\infty} + \frac{\gamma - 1}{2} M_{cl}^2 \left\{ 1 + V_\infty / V_{cl} - 2V / V_{cl} \right\} \right]$$

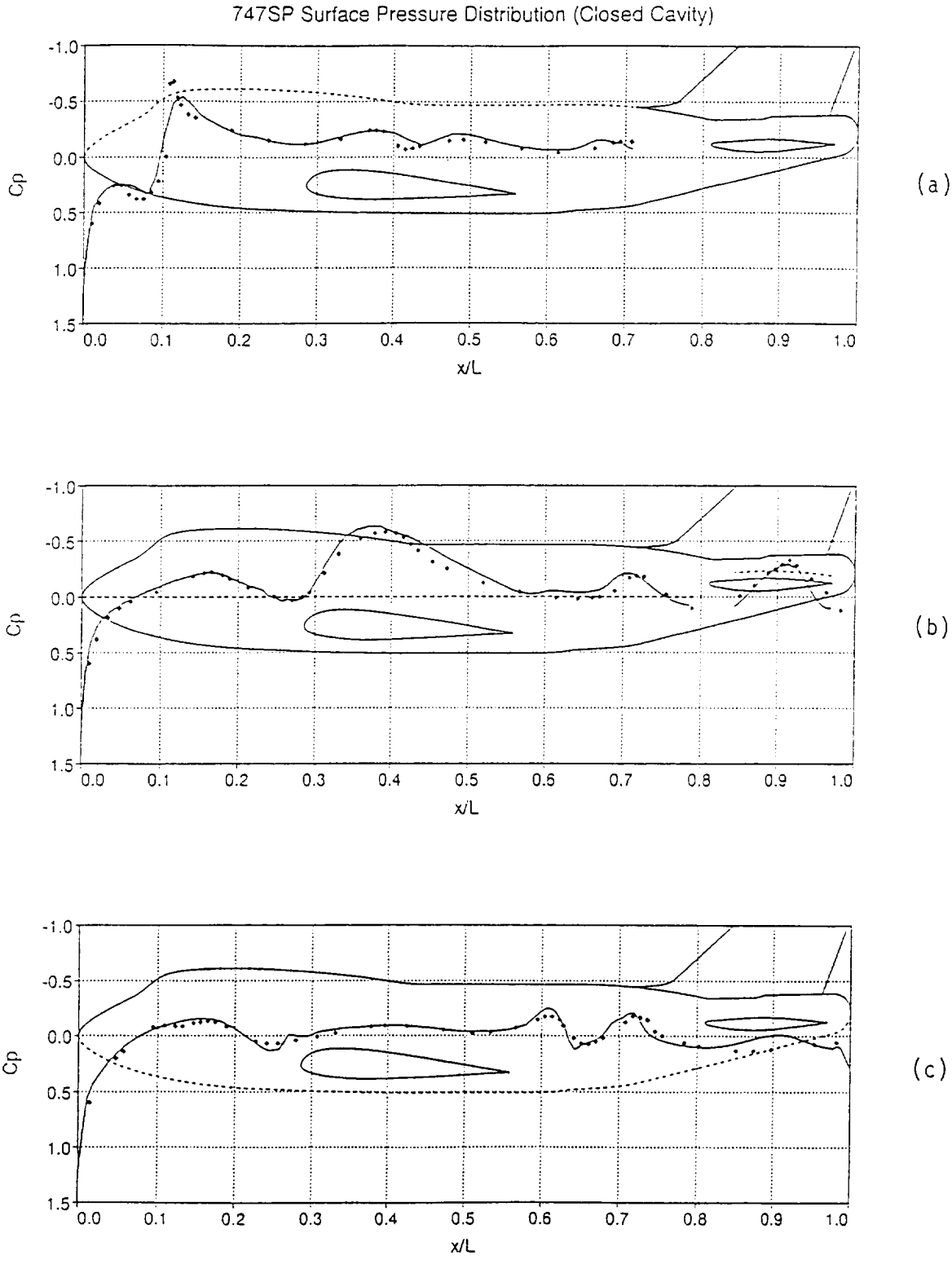

Fig. 1 747SP surface pressure distribution: (a) fuselage top; (b) fuselage side; and (c) fuselage bottom.

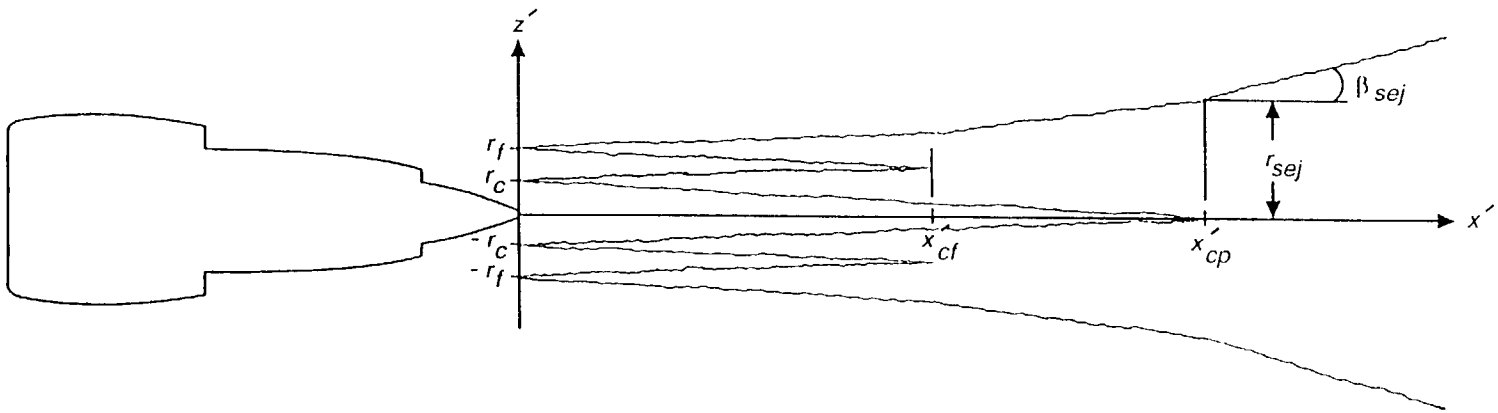

Fig. 2 Engine exhaust plume.

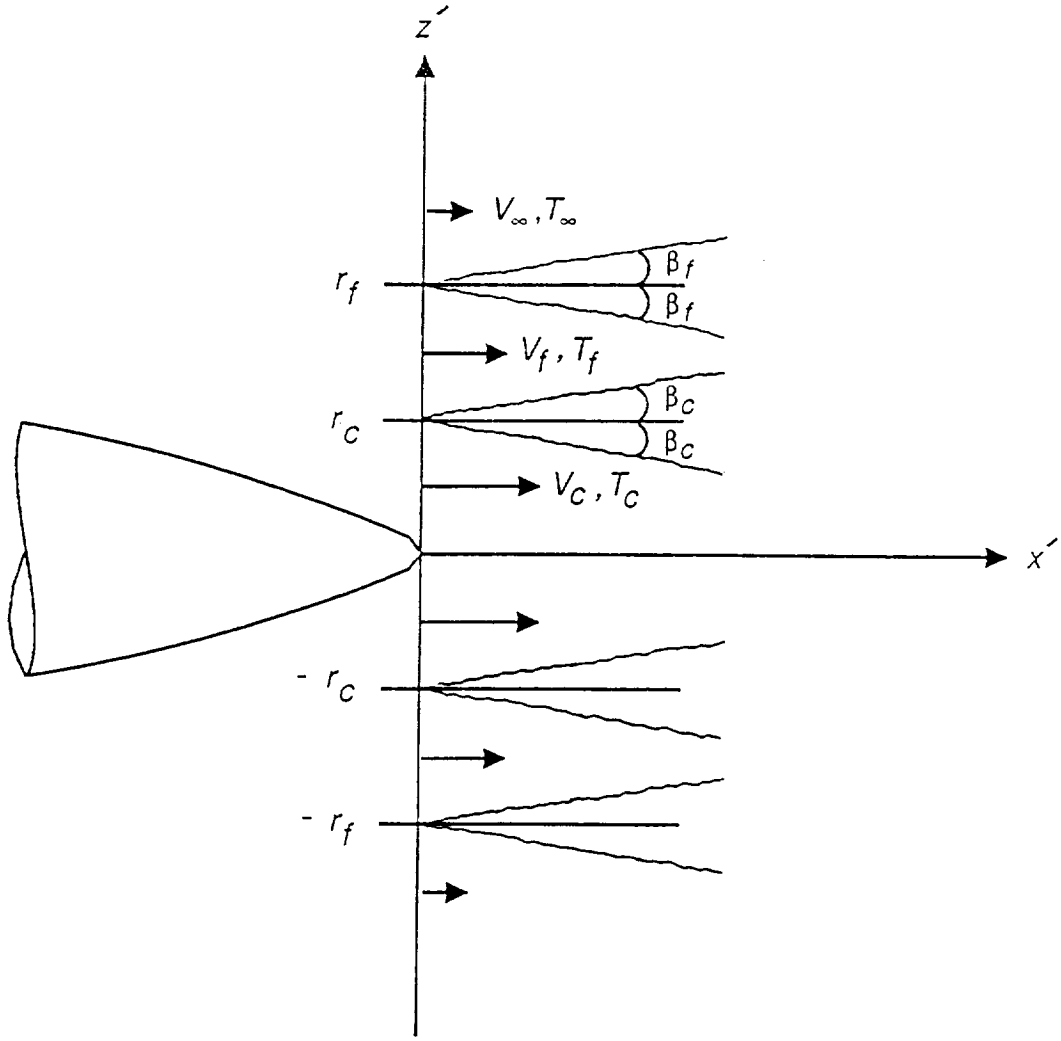

Fig. 3 Sketch of the engine plume near the tip of the tail cone.

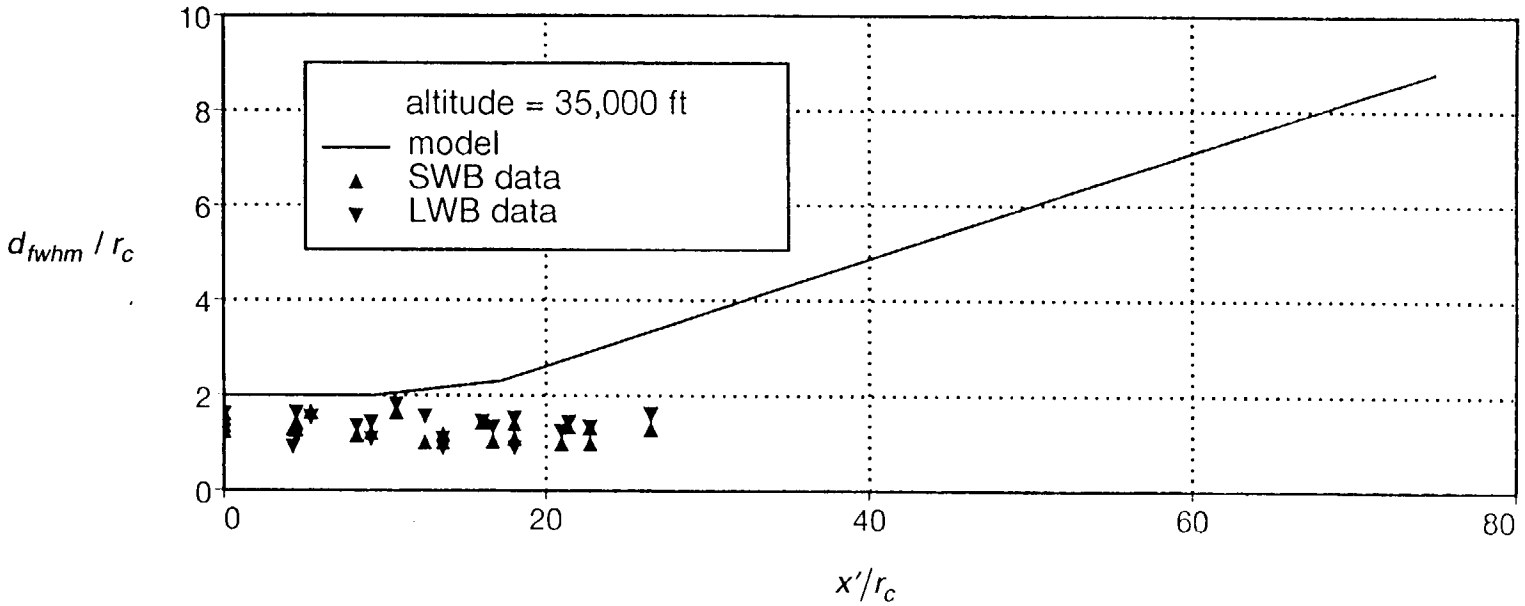

Fig. 4 Thermal plume width at 35,000 feet; IR data and empirical prediction.

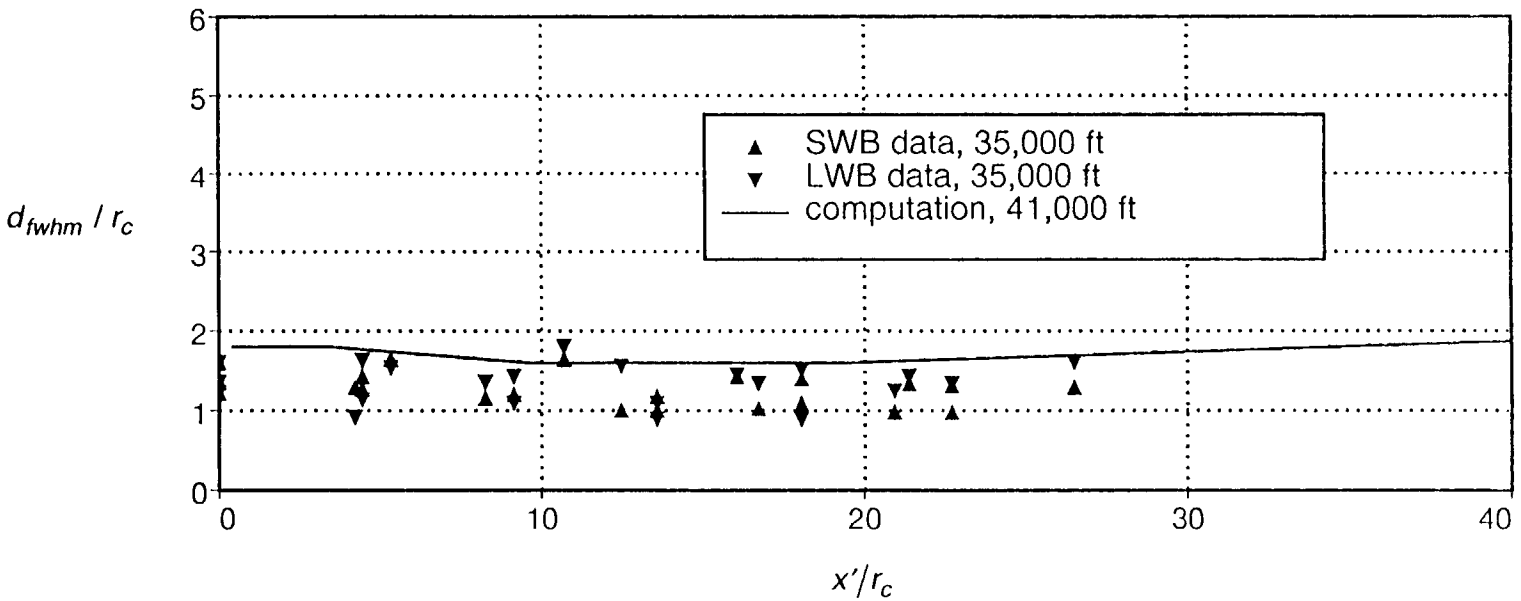

Fig. 5 Thermal plume width; IR data at 35,000 feet and CFD prediction at 41,000 feet.

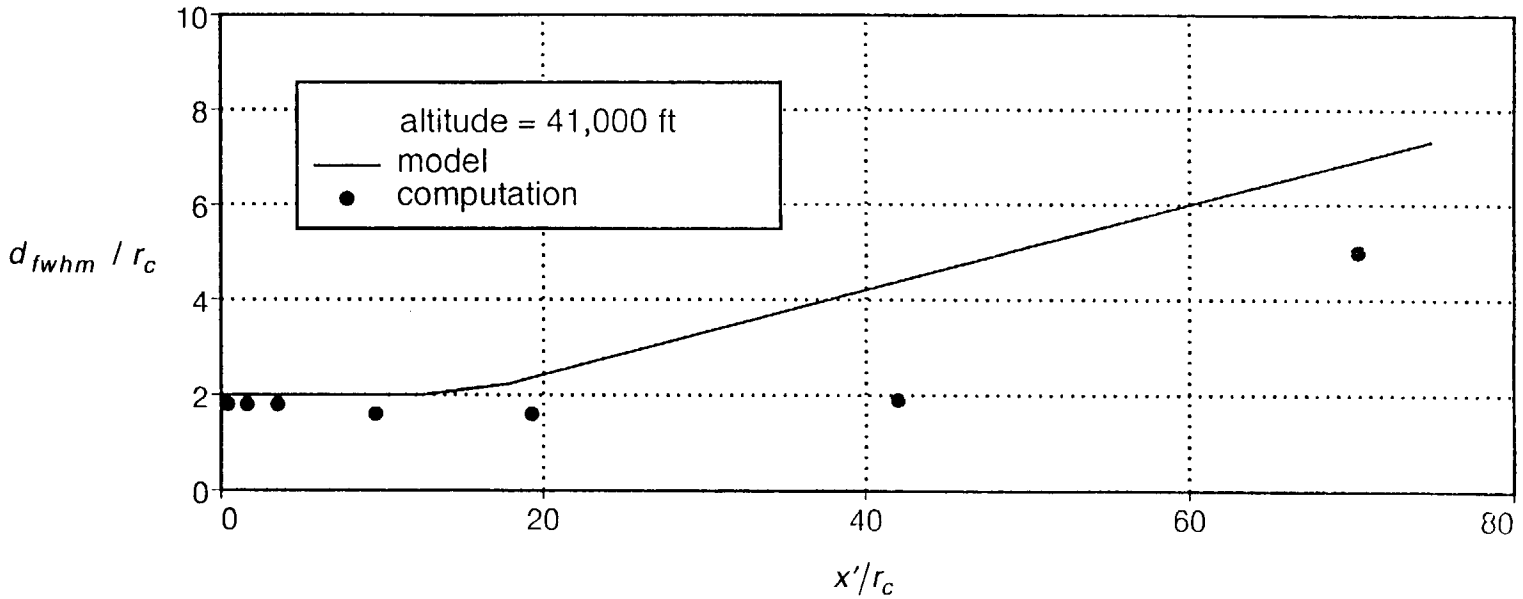

Fig. 6 Thermal plume width at 41,000 feet; empirical and CFD predictions.

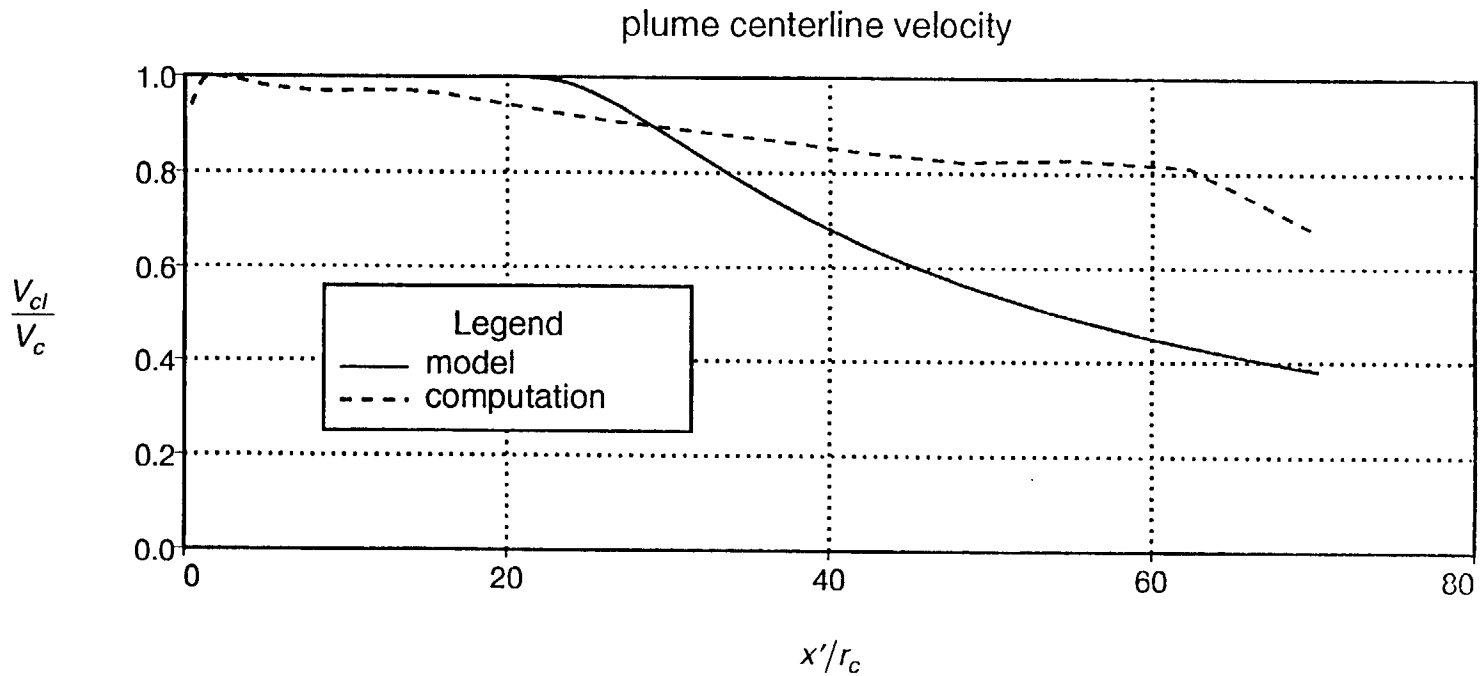

Fig. 7 Plume centerline velocity distributions.

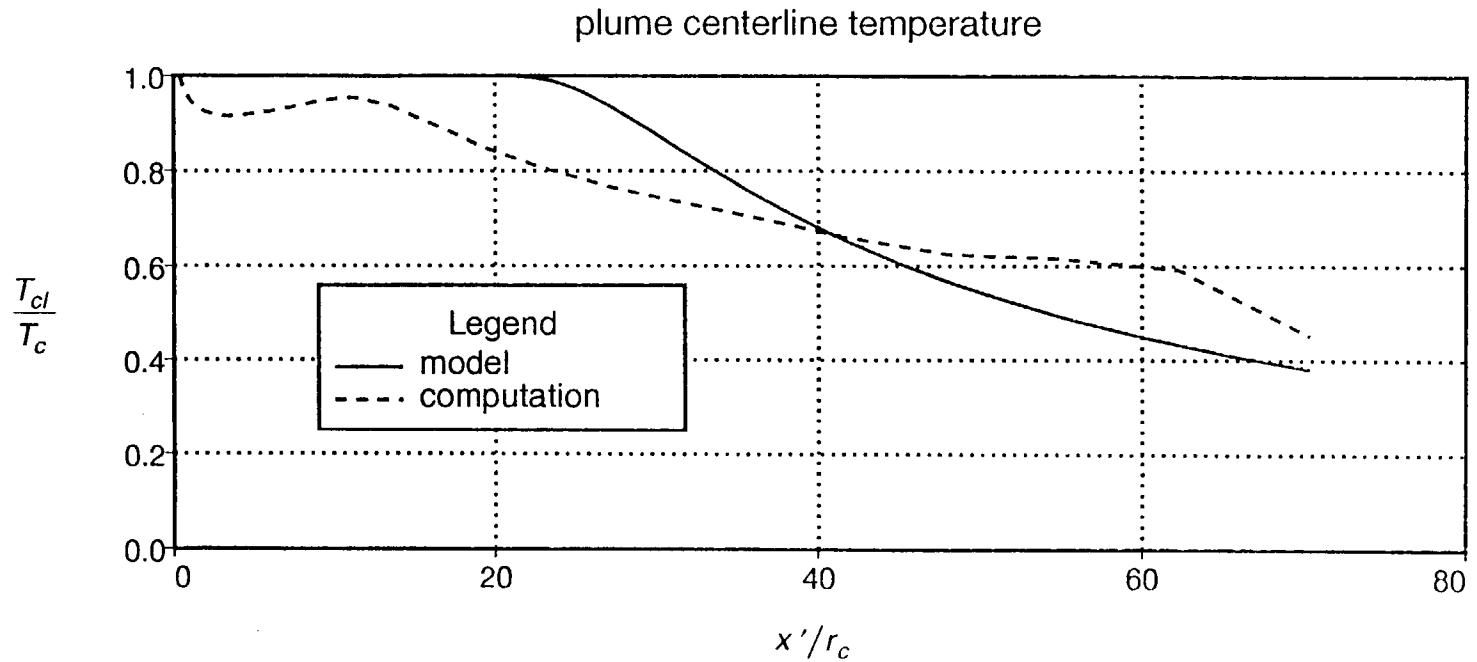

Fig. 8 Plume centerline temperature distributions.

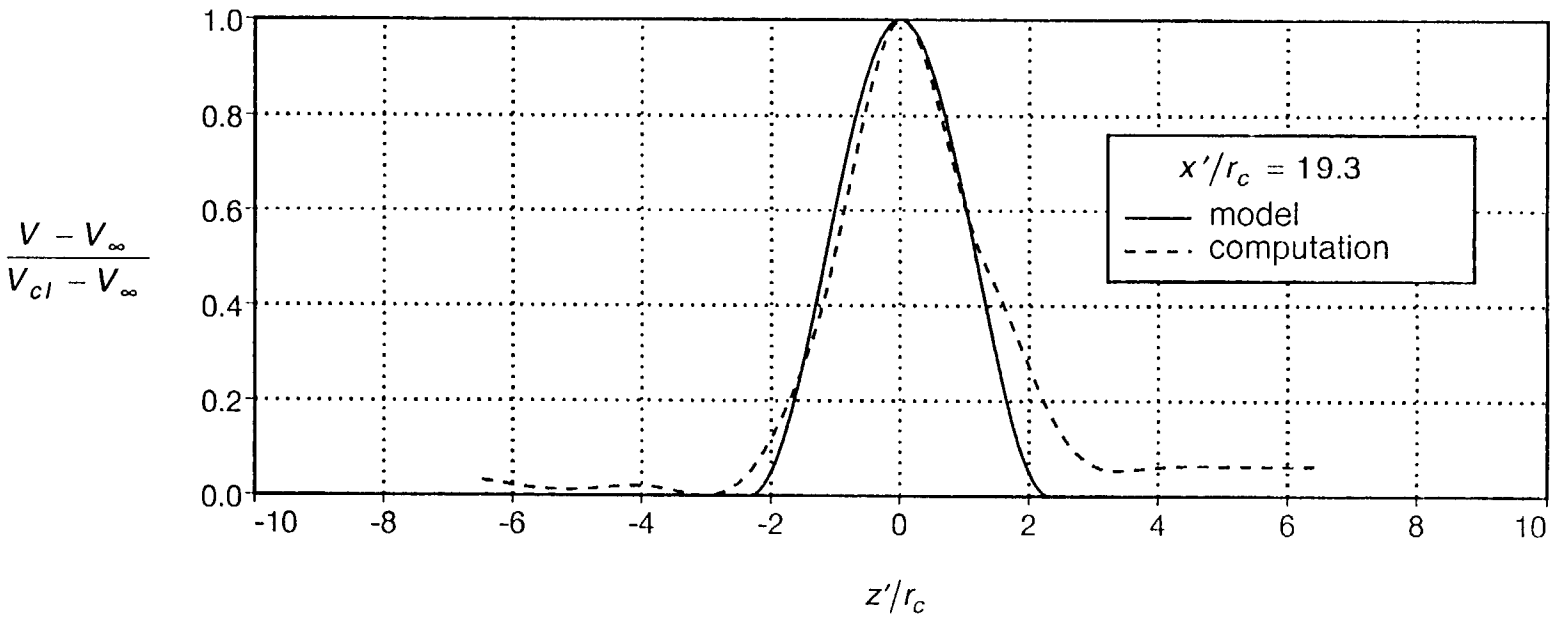

Fig. 9 Plume velocity distributions at $x'/r_c = 19.3$.

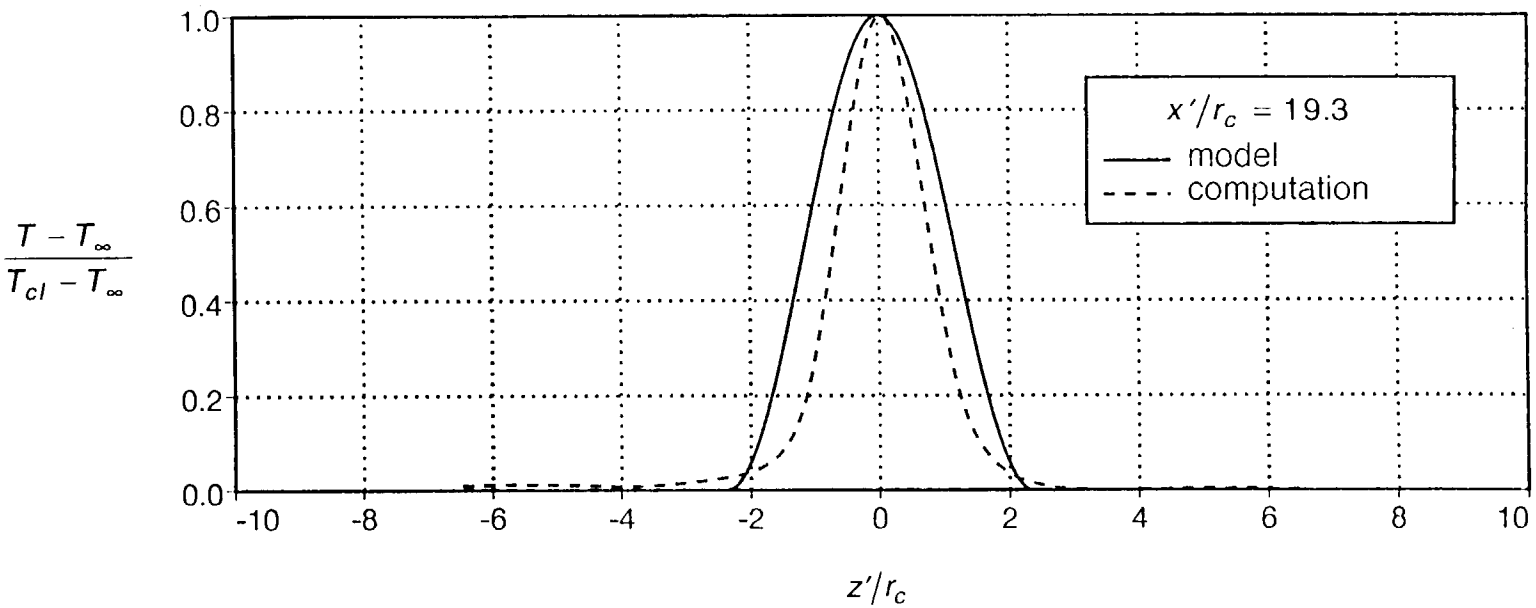

Fig. 10 Plume temperature distributions at $x'/r_c = 19.3$.

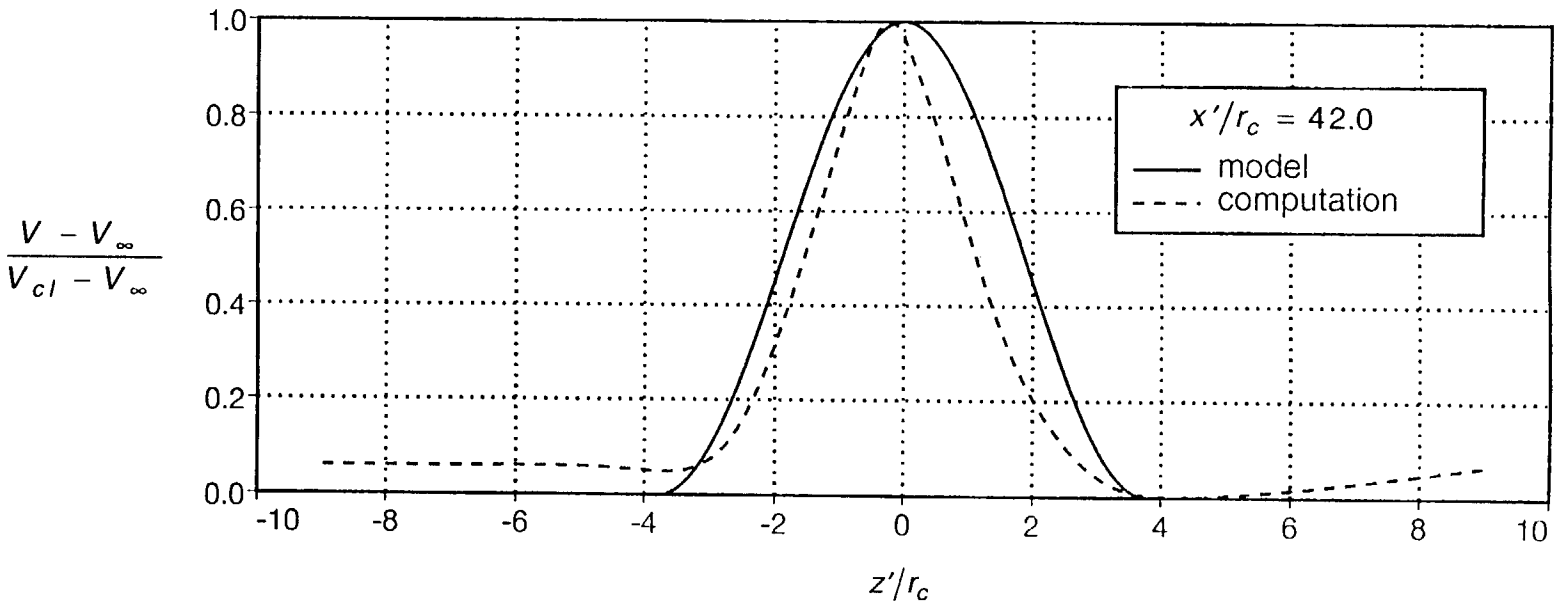

Fig. 11 Plume velocity distributions at $x'/r_c = 42.0$.

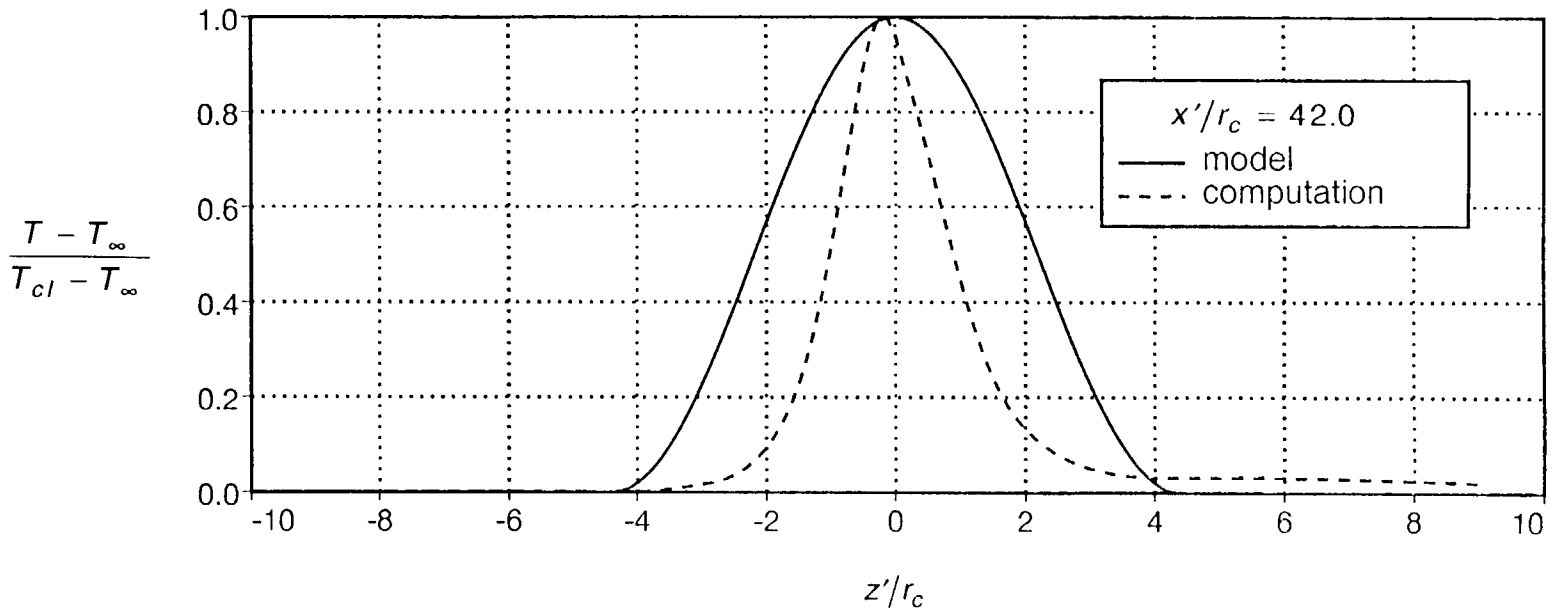

Fig. 12 Plume temperature distributions at $x'/r_c = 42.0$.

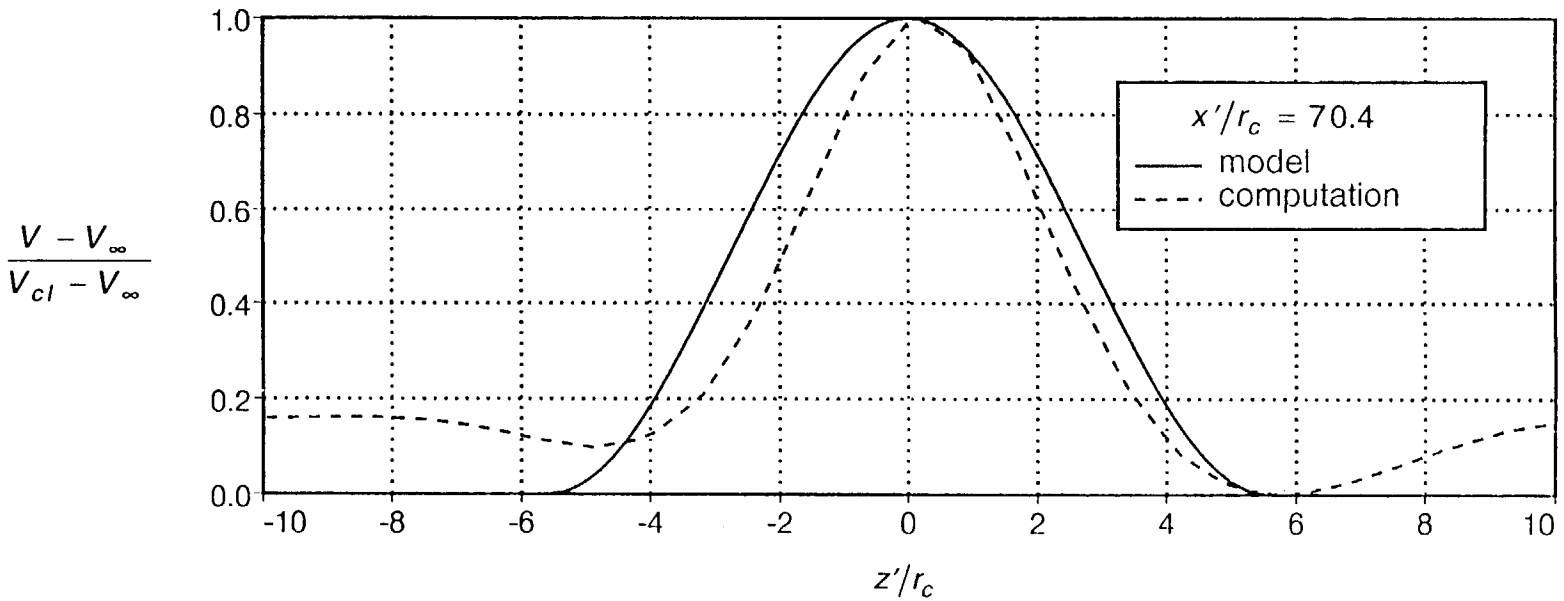

Fig. 13 Plume velocity distributions at $x'/r_c = 70.4$.

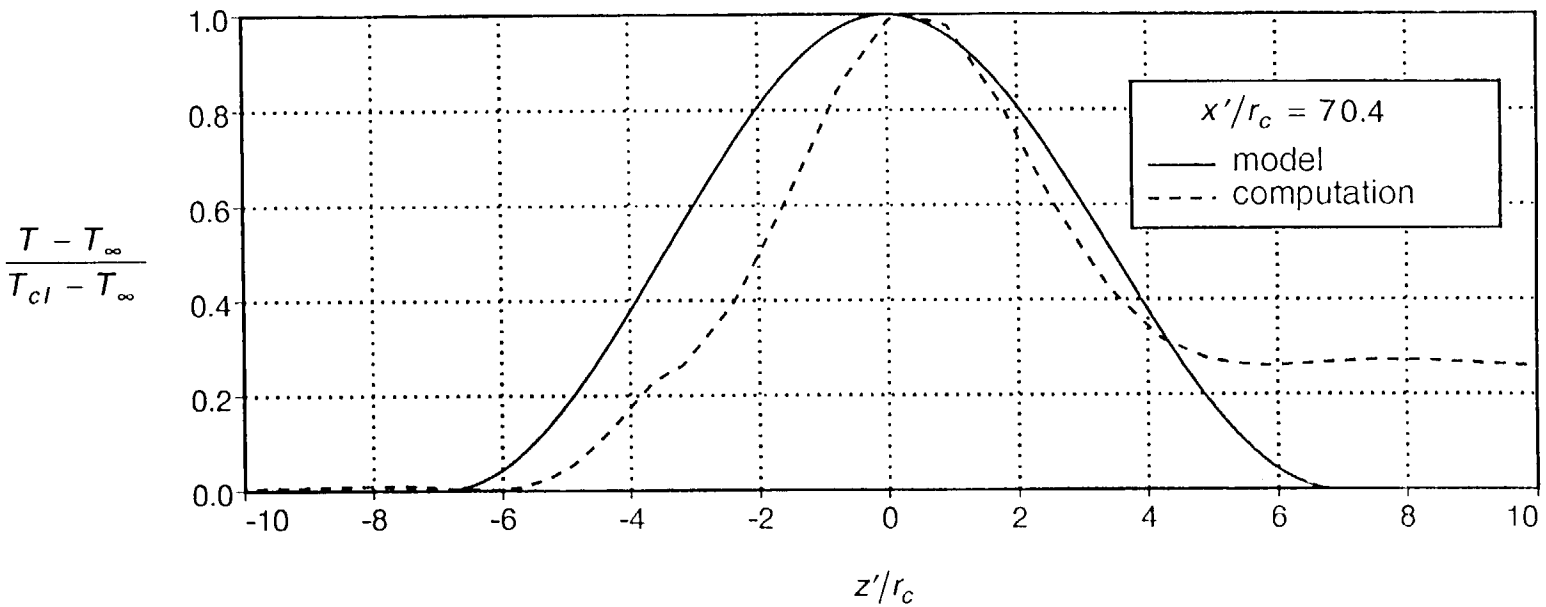

Fig. 14 Plume temperature distributions at $x'/r_c = 70.4$.

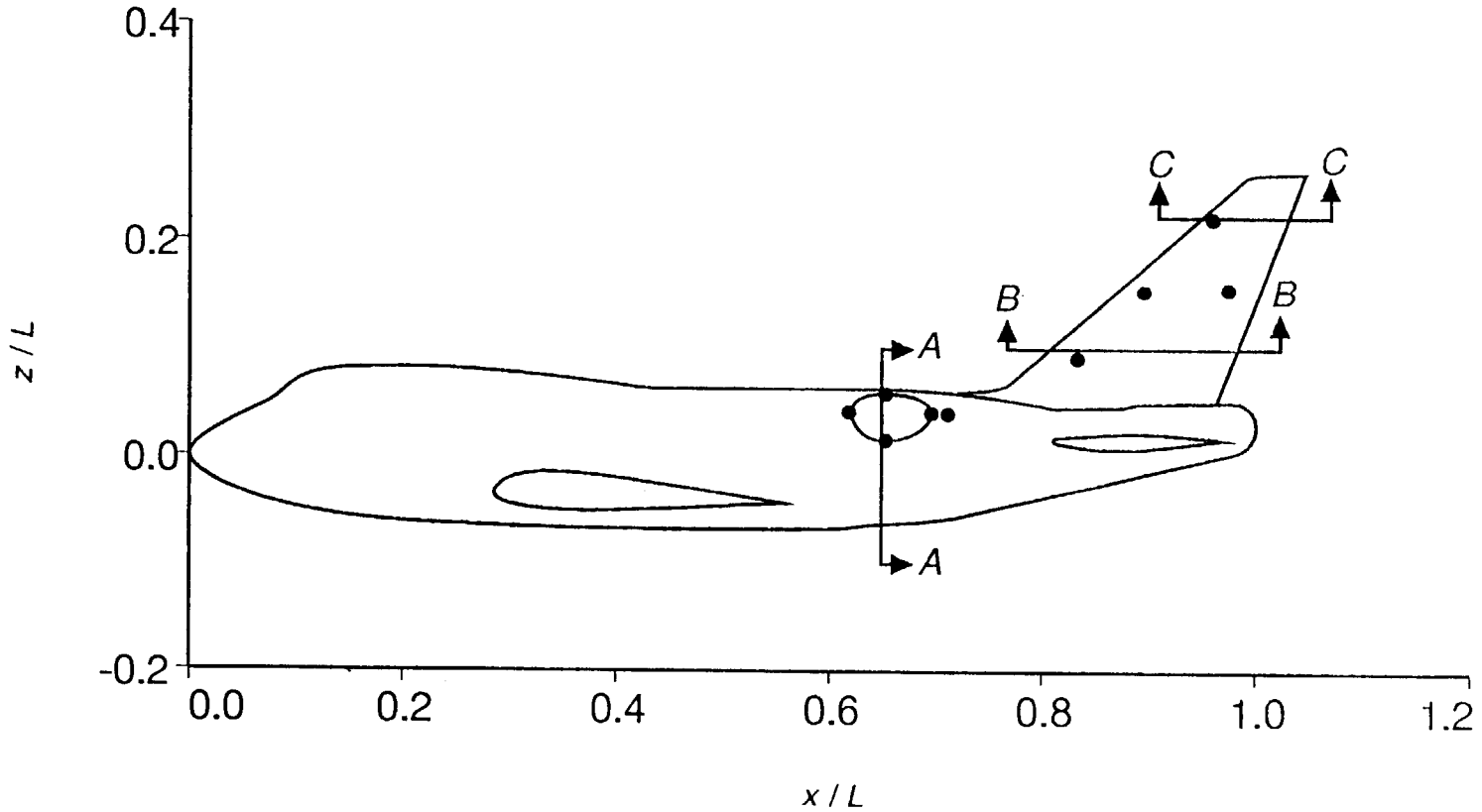

Fig. 15 Sketch of the locations of cross-sectional planes AA, BB, and CC through the cavity and vertical stabilizer.

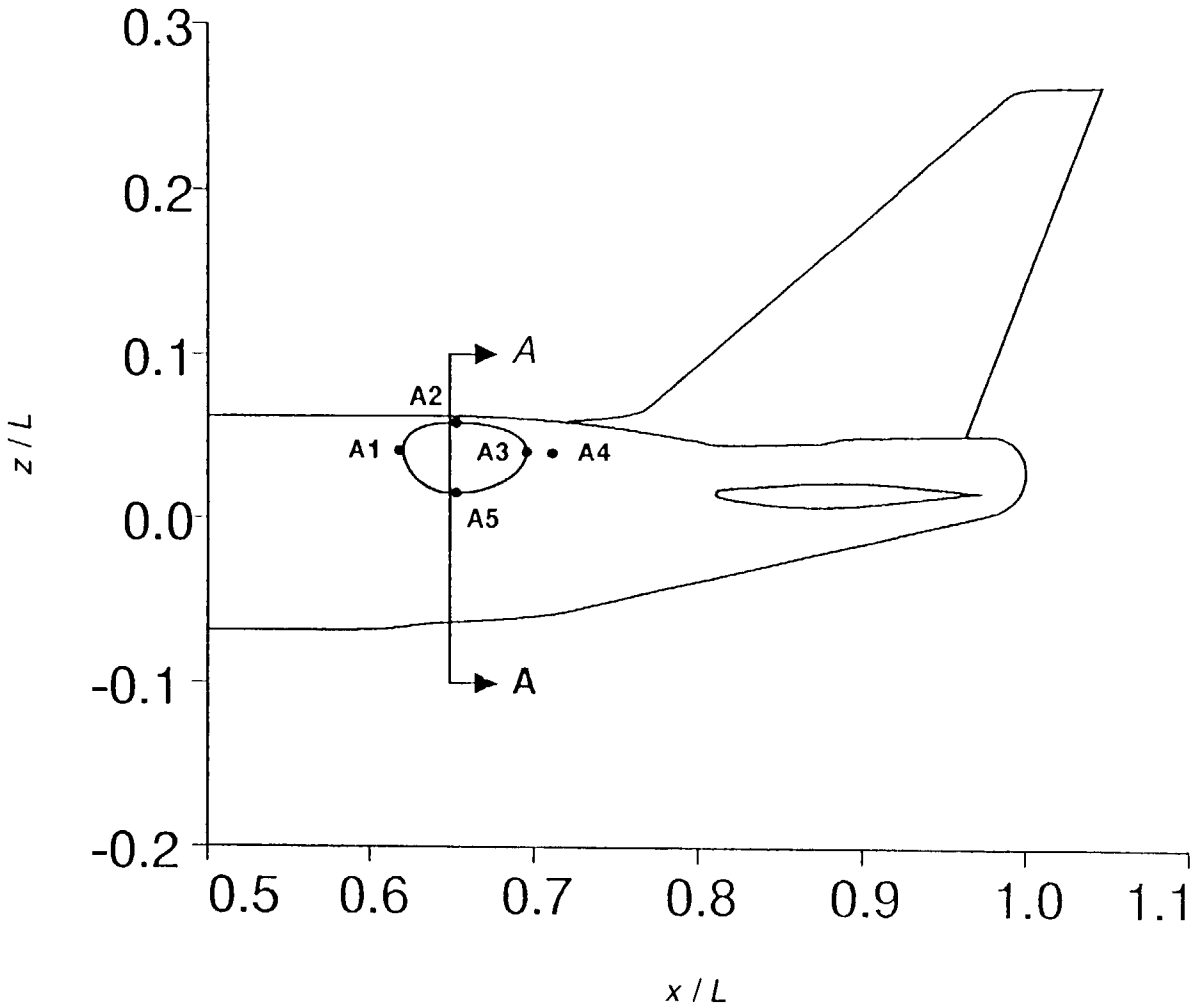

Fig. 16 Sketch of the locations of points A1, A2, A3, A4, and A5 on the fuselage.

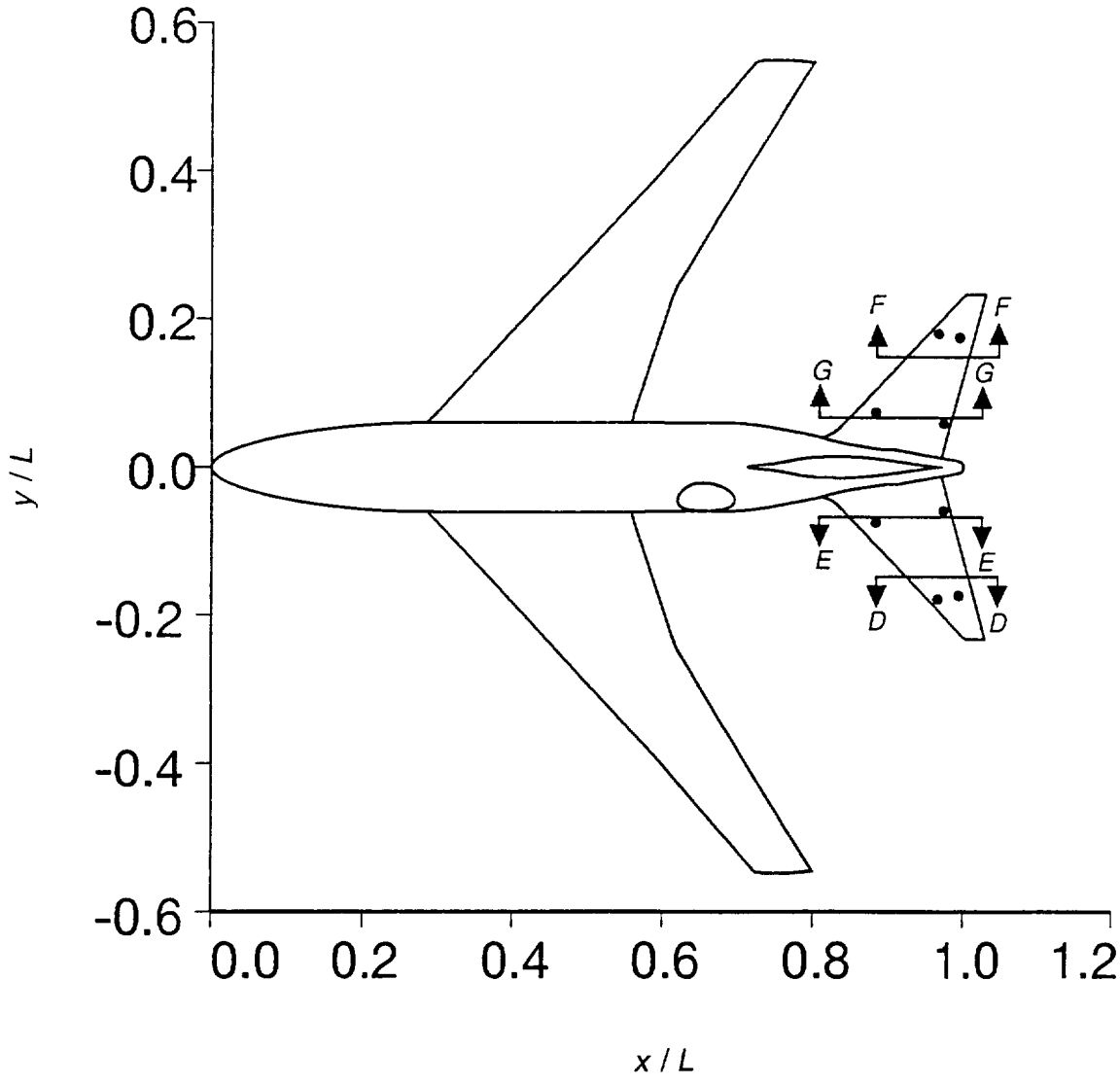

Fig. 17 Sketch of the locations of cross-sectional planes DD, EE, FF, and GG on the horizontal stabilizers.

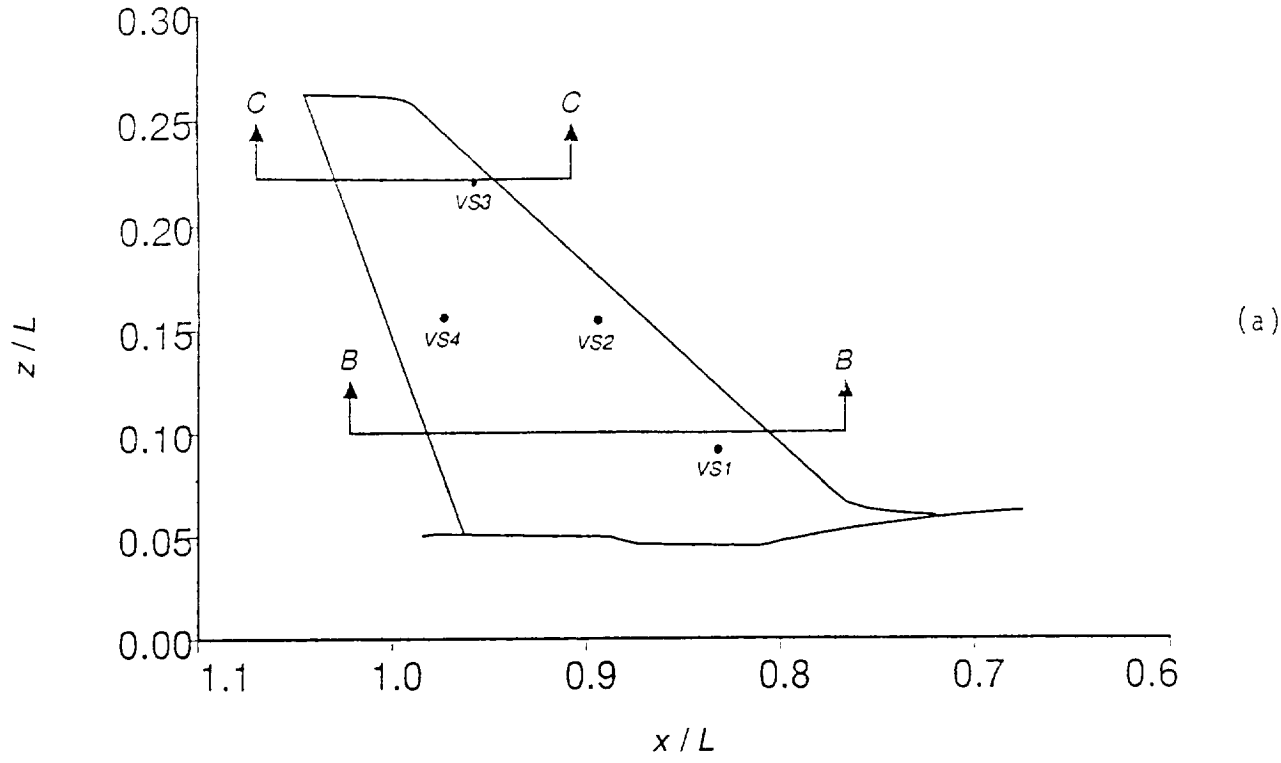

(a)

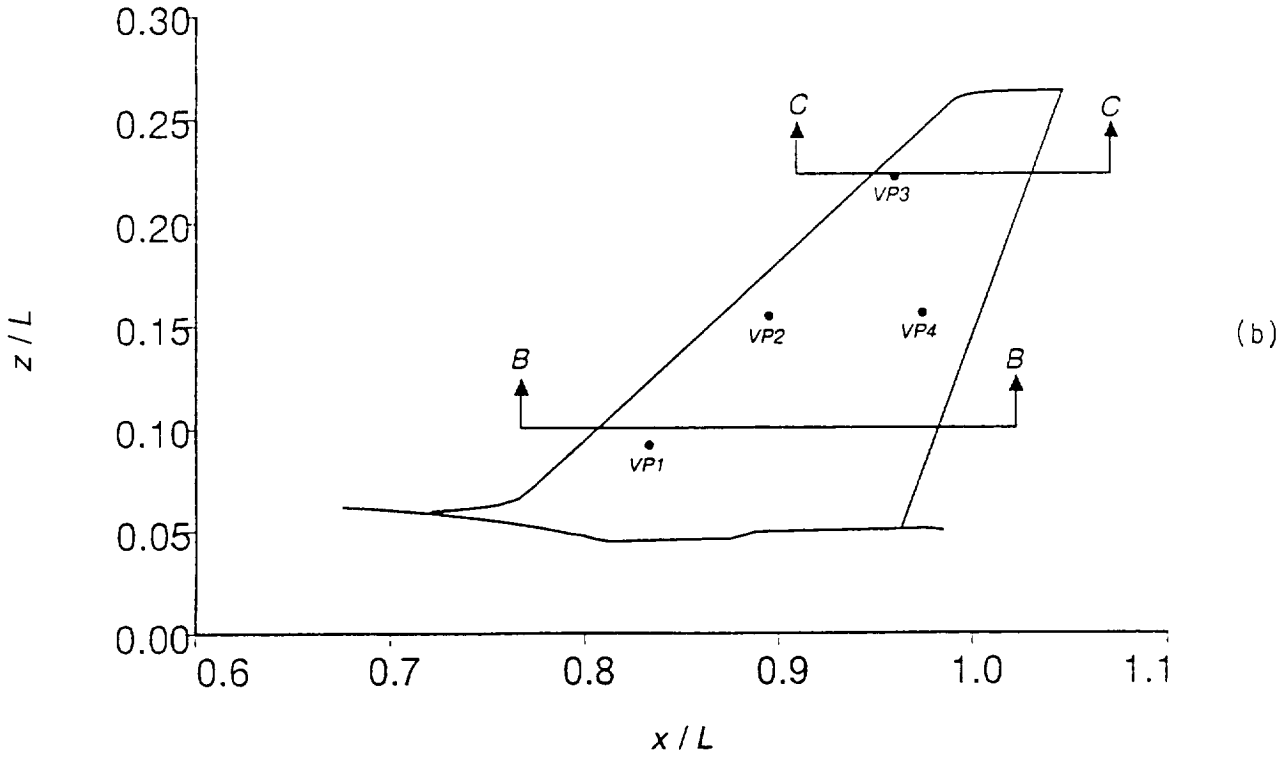

(b)

Fig. 18 Locations of cross-sections BB and CC through the vertical stabilizer and points on its surface: (a) starboard side points VS1 through VS4; (b) port side points VP1 through VP4.

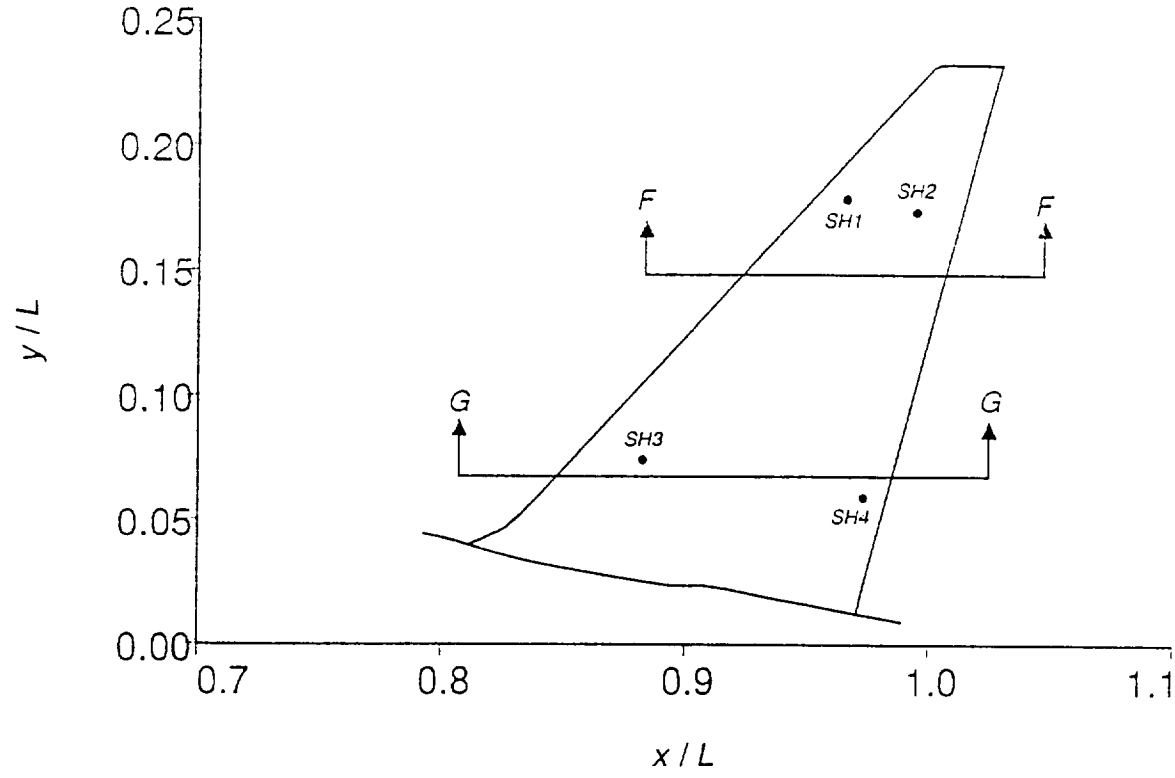

(a)

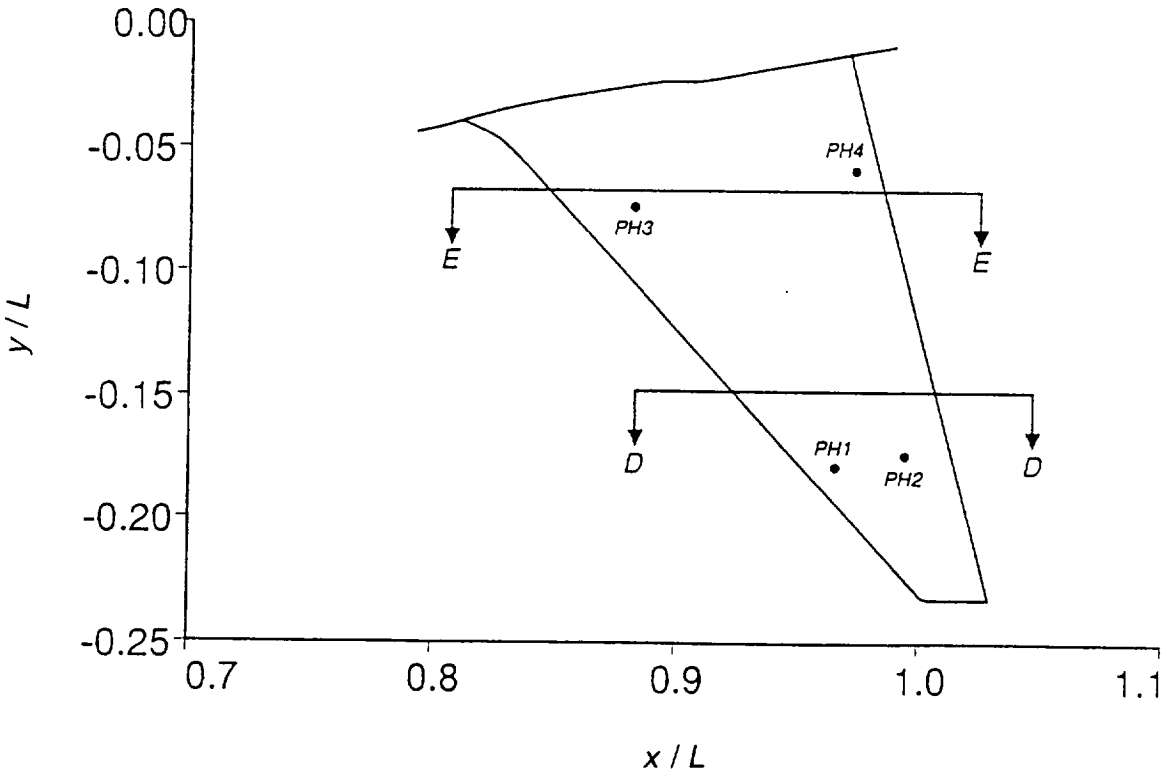

(b)

Fig. 19 Locations of cross-sections through the horizontal stabilizers and points on their surfaces: (a) starboard stabilizer cross-sections FF and GG and points SH1 through SH4; (b) port stabilizer cross-sections DD and EE and points PH1 through PH4.

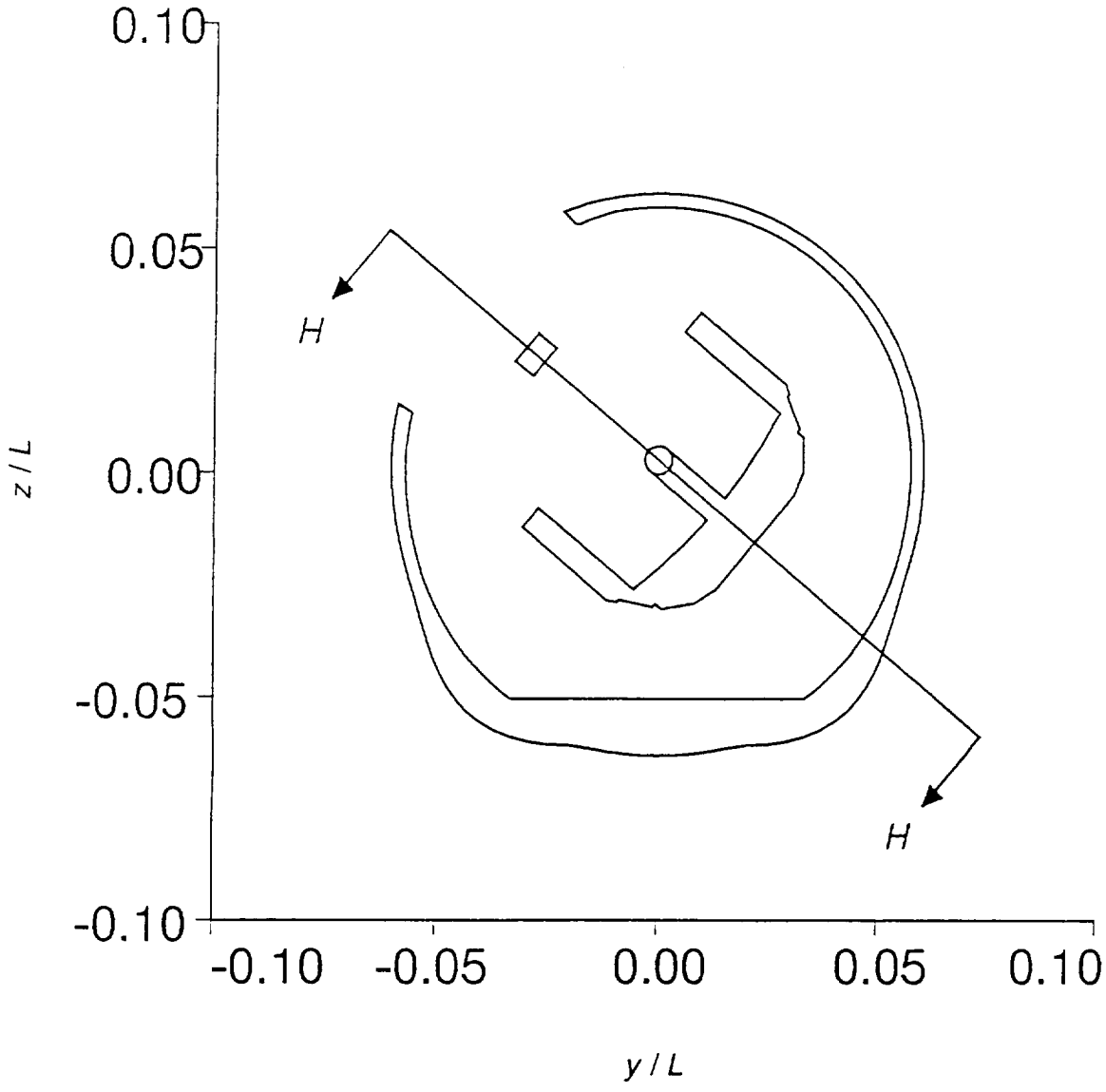

Fig. 20 Cross-section AA through the cavity.

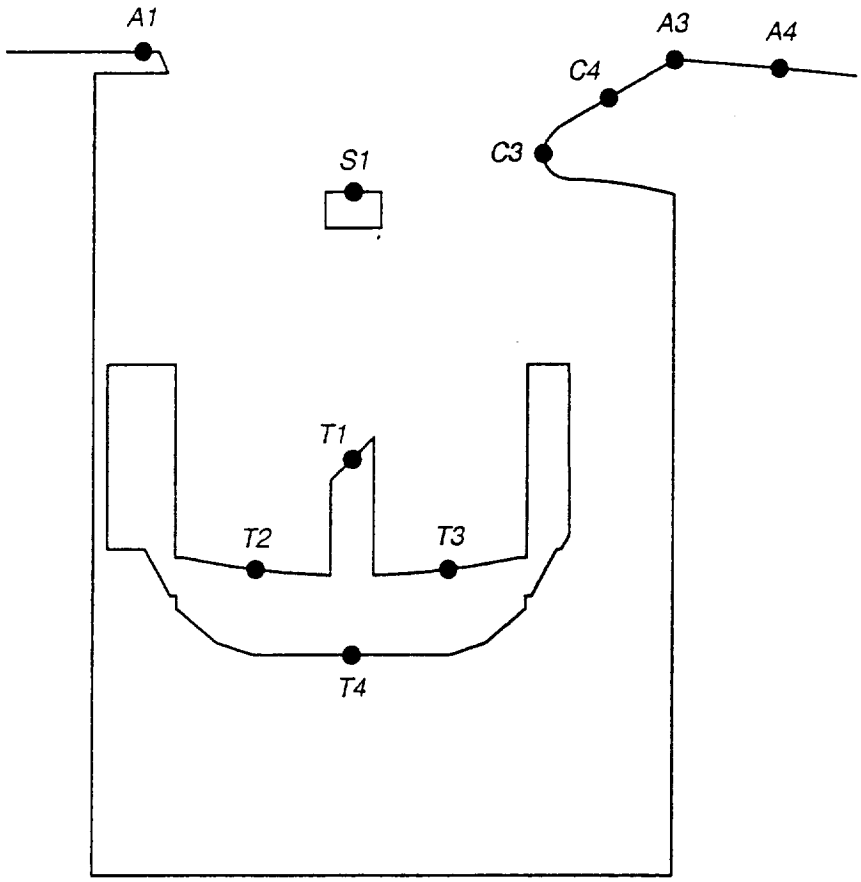

Fig. 21 Cross-section HH through the cavity.

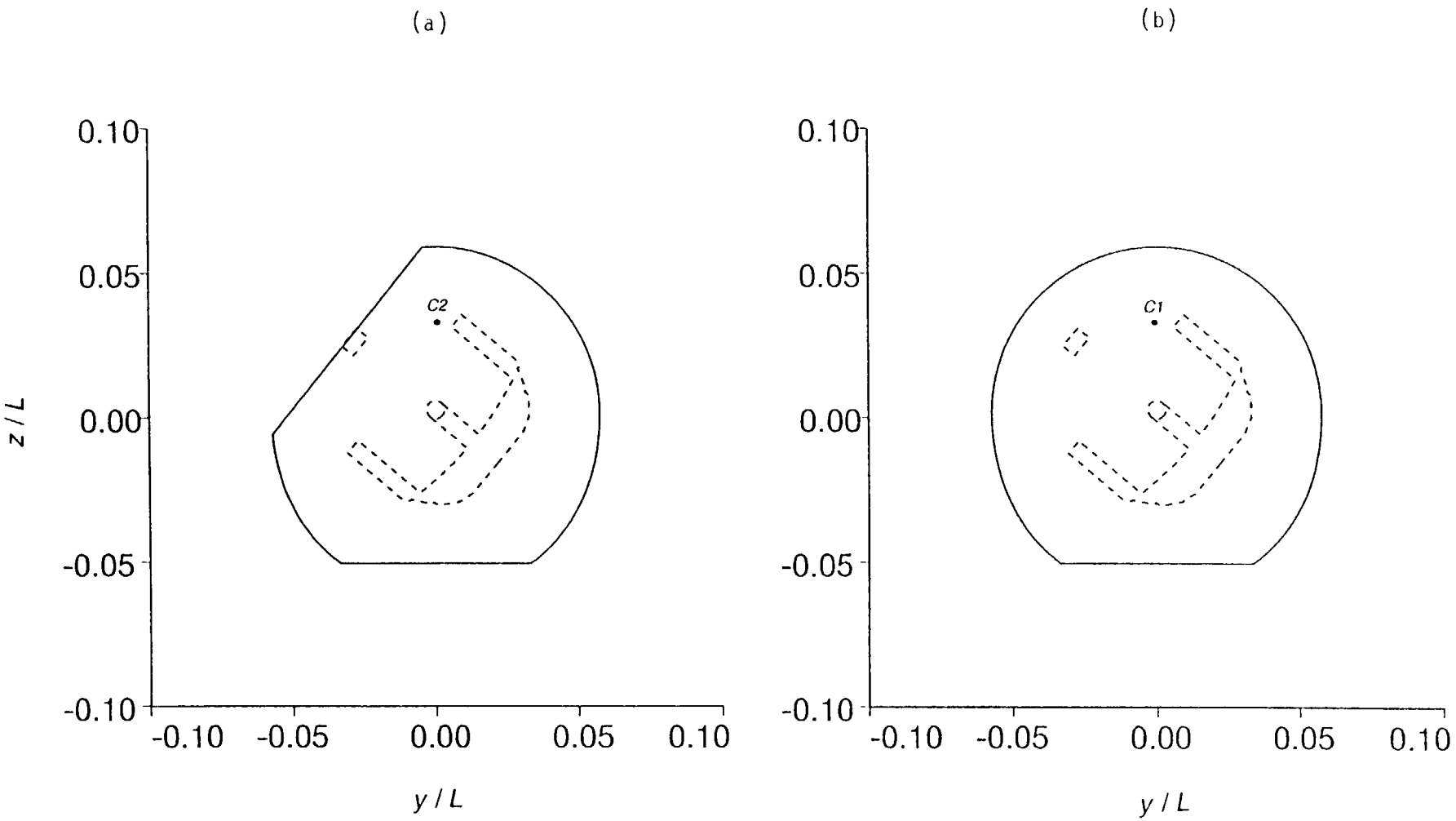

Fig. 22 Locations of (a) point C2 on the aft cavity bulkhead and (b) point C1 on the forward bulkhead.

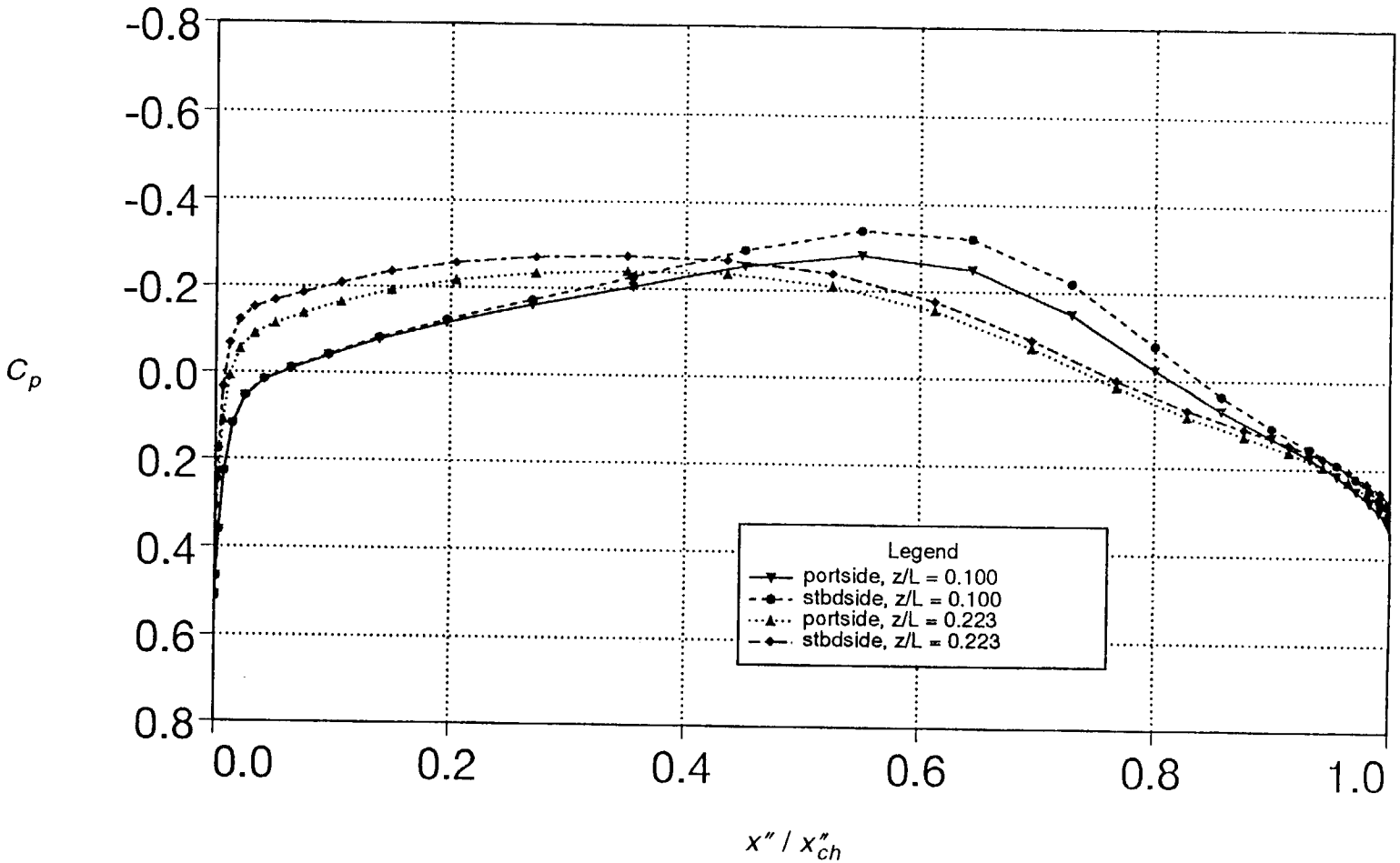

Fig. 23 Vertical stabilizer C_p distributions.

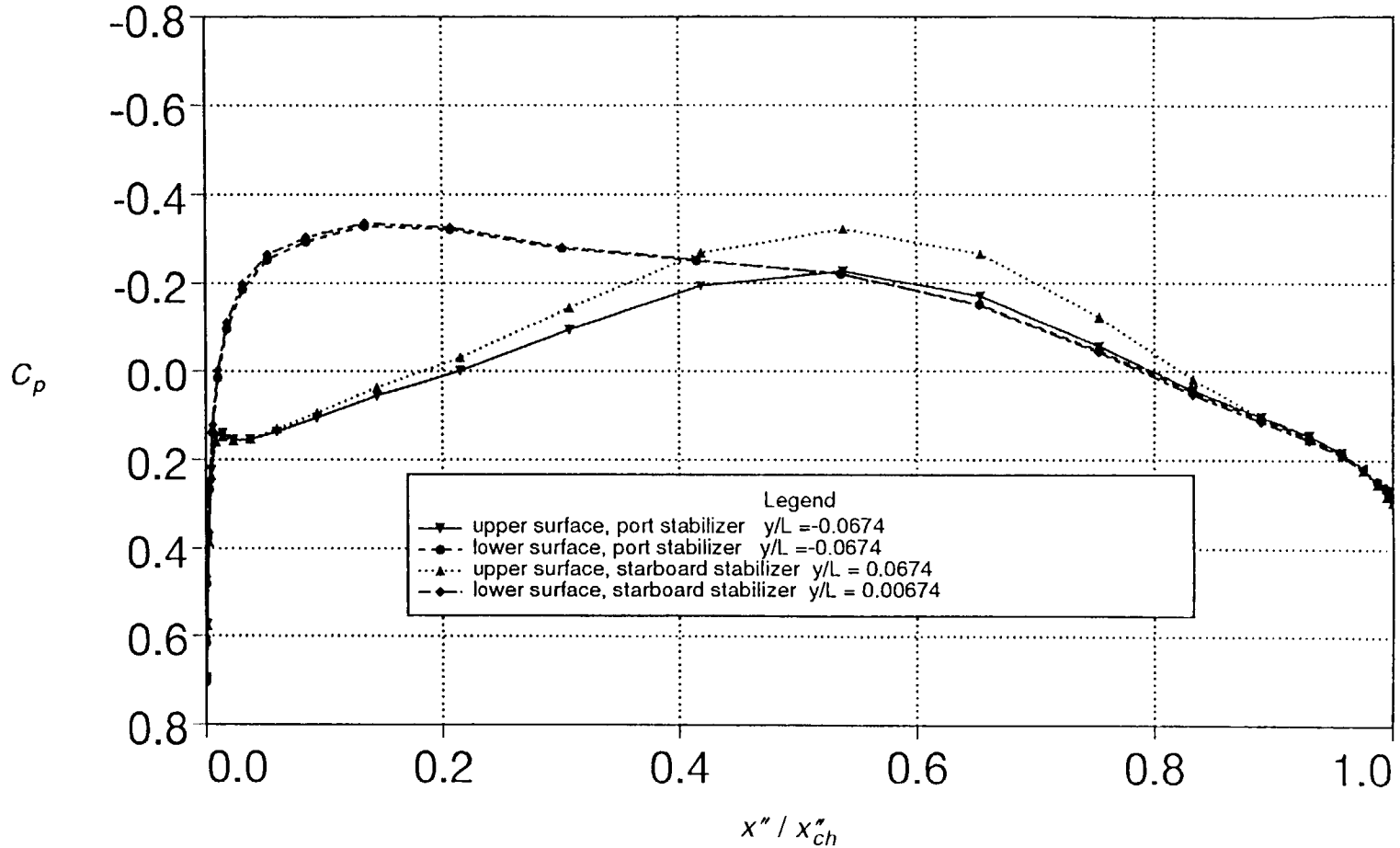

Fig. 24 Horizontal stabilizer C_p distributions on cross-sections EE and GG.

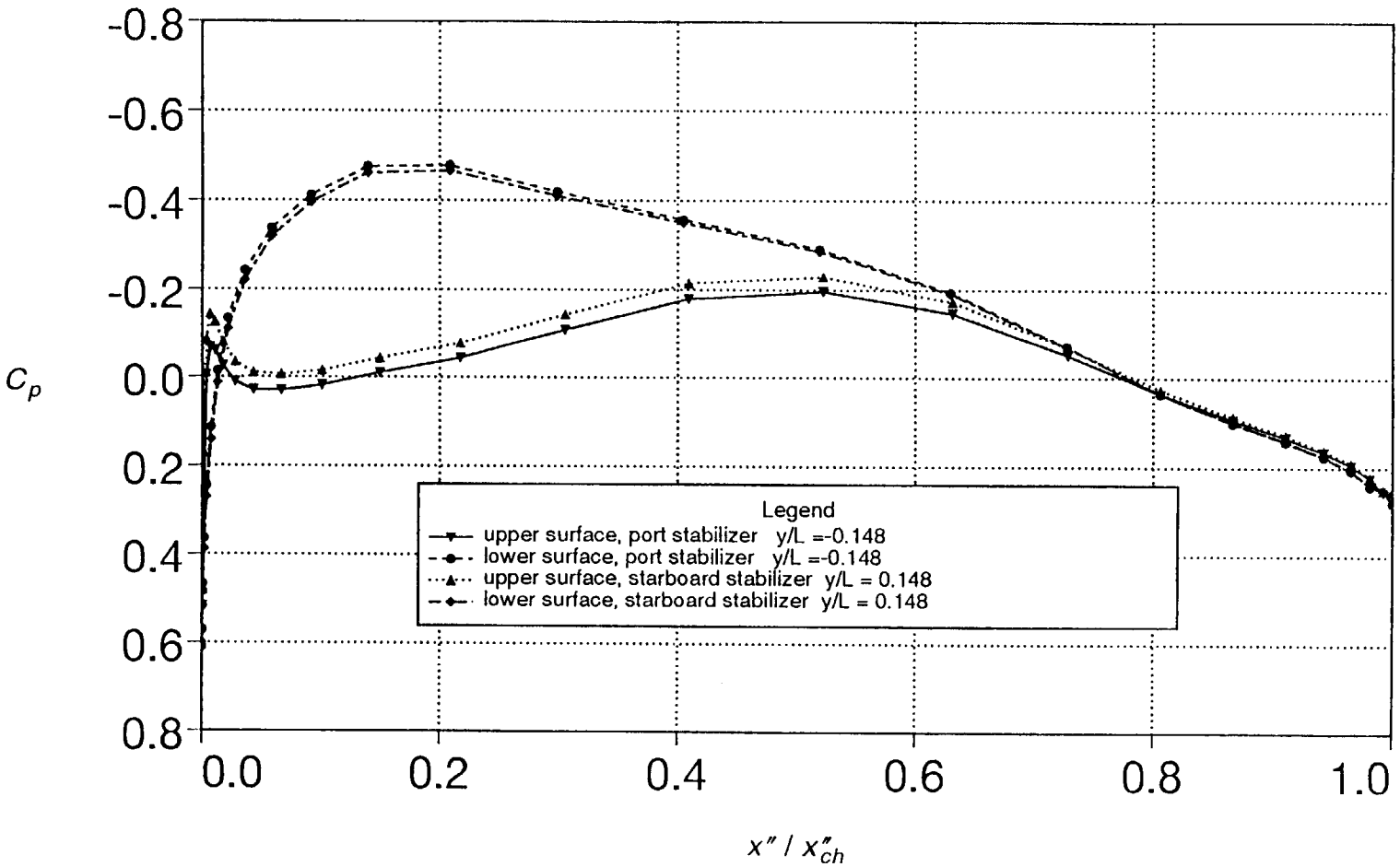

Fig. 25 Horizontal stabilizer C_p distributions on cross-sections DD and FF.

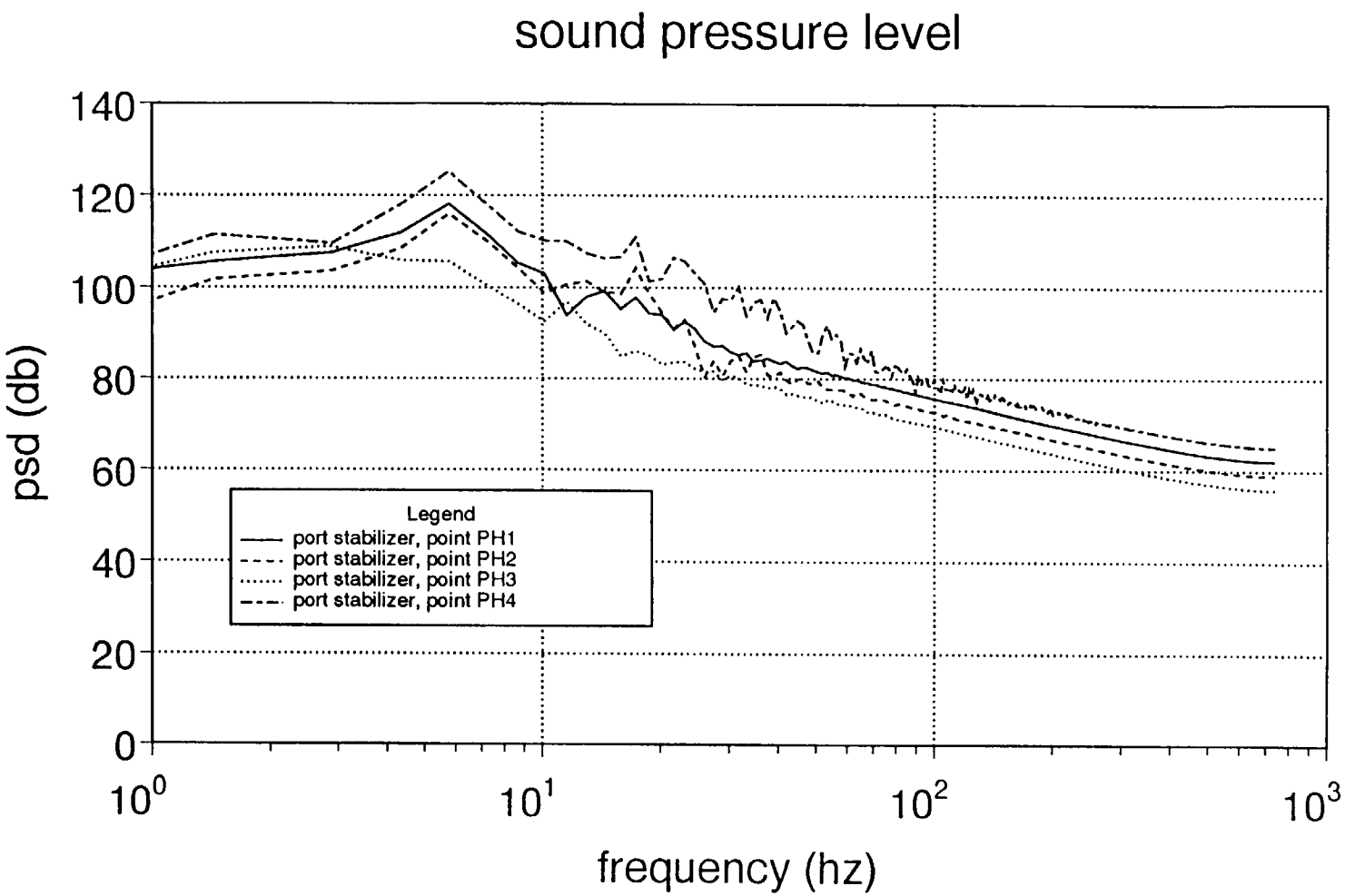

Fig. 26 Spectra of sound pressure levels on the port horizontal stabilizer.

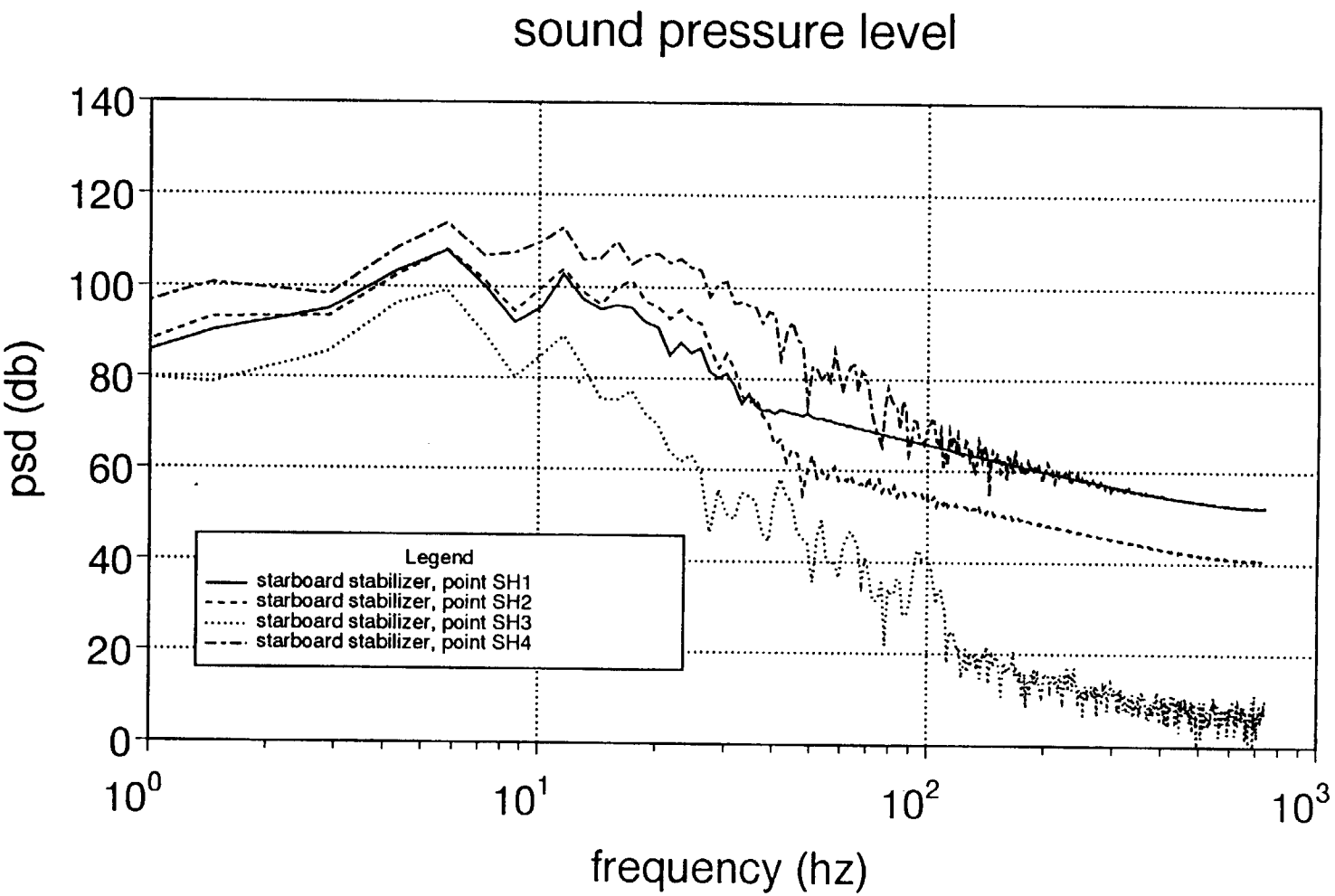

Fig. 27 Spectra of sound pressure levels on the starboard horizontal stabilizer.

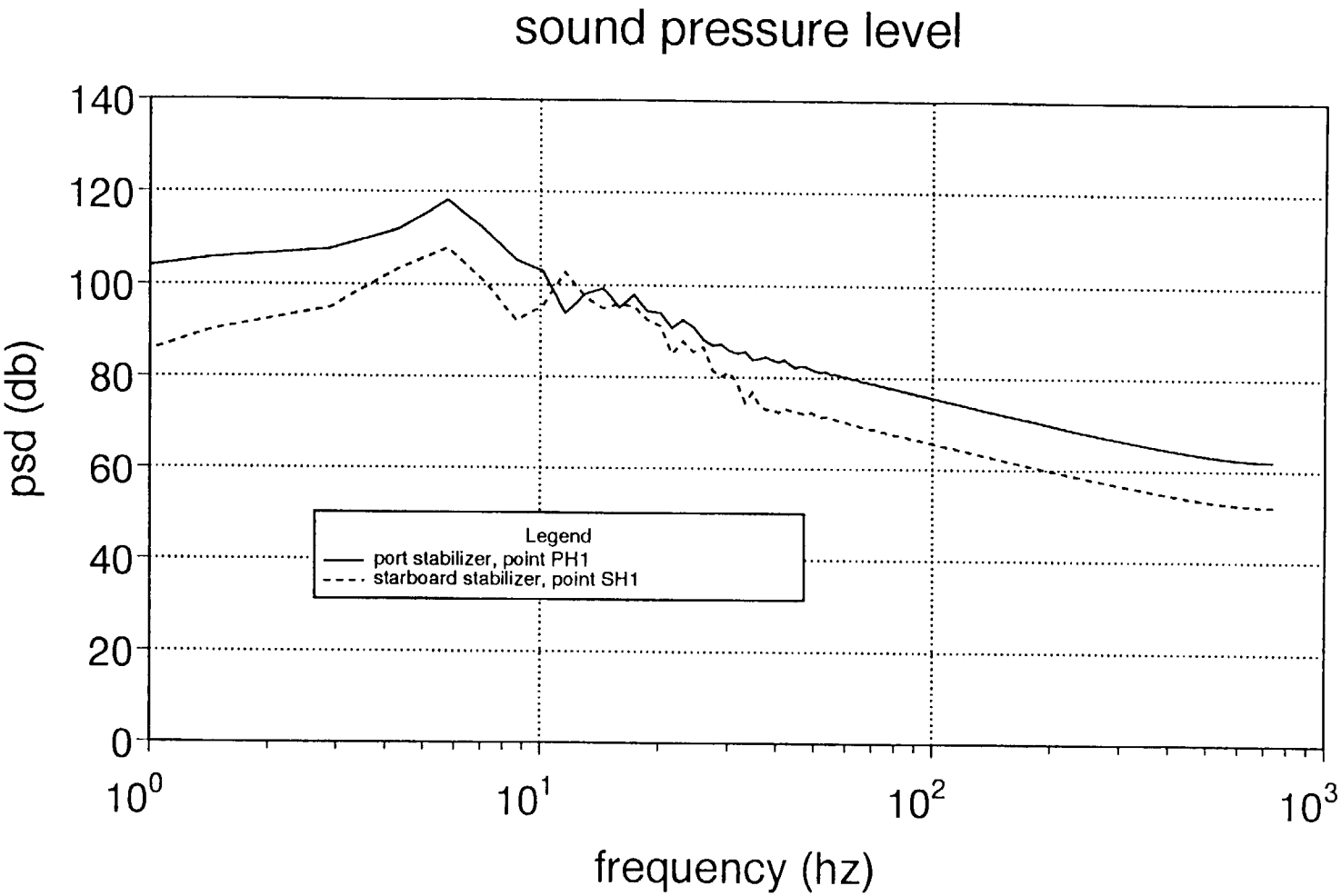

Fig. 28 Spectra of sound pressure levels at points PH1 and ŞH1 on the horizontal stabilizers.

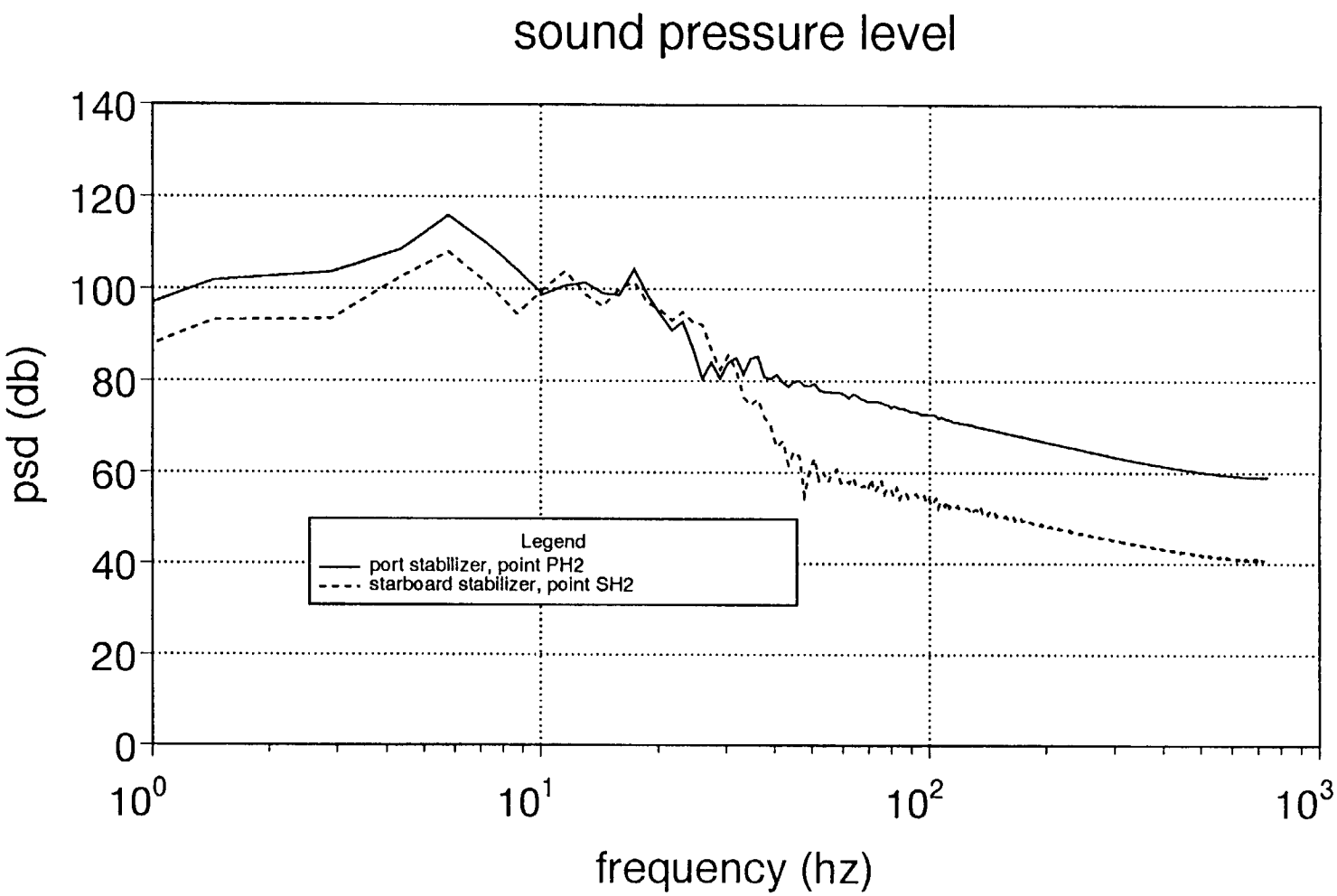

Fig. 29 Spectra of sound pressure levels at points PH2 and SH2 on the horizontal stabilizers.

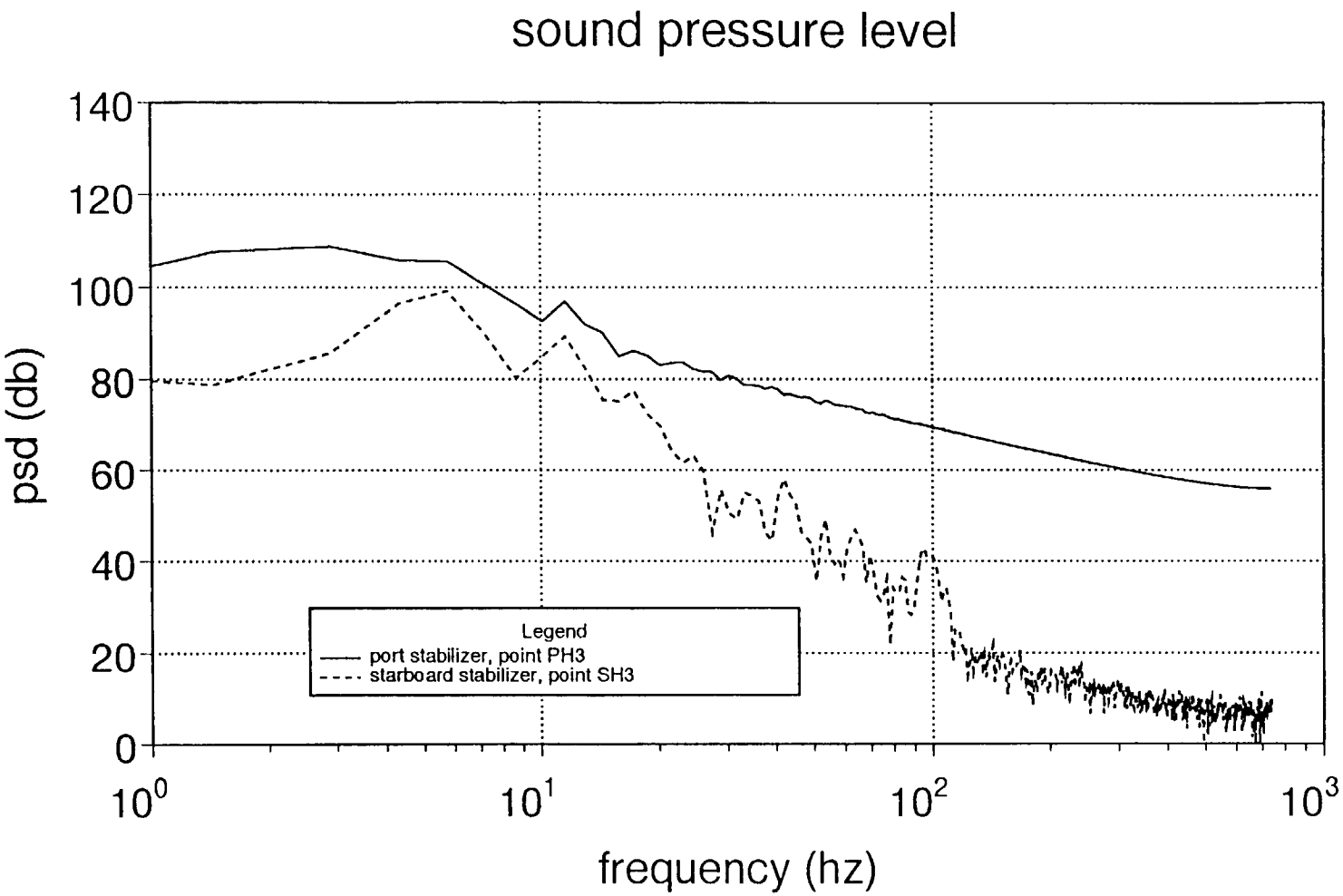

Fig. 30 Spectra of sound pressure levels at points PH3 and SH3 on the horizontal stabilizers.

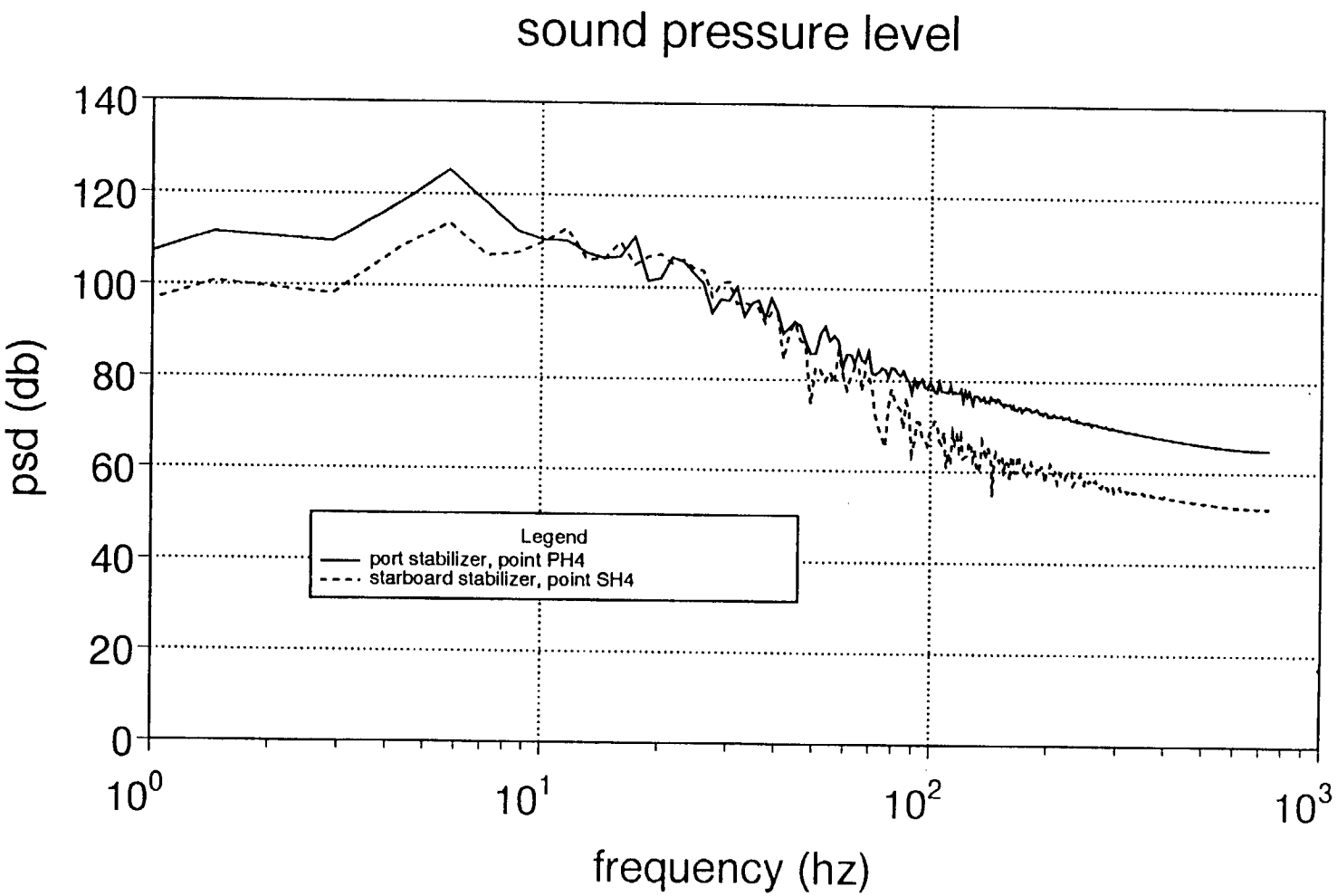

Fig. 31 Spectra of sound pressure levels at points PH4 and SH4 on the horizontal stabilizers.

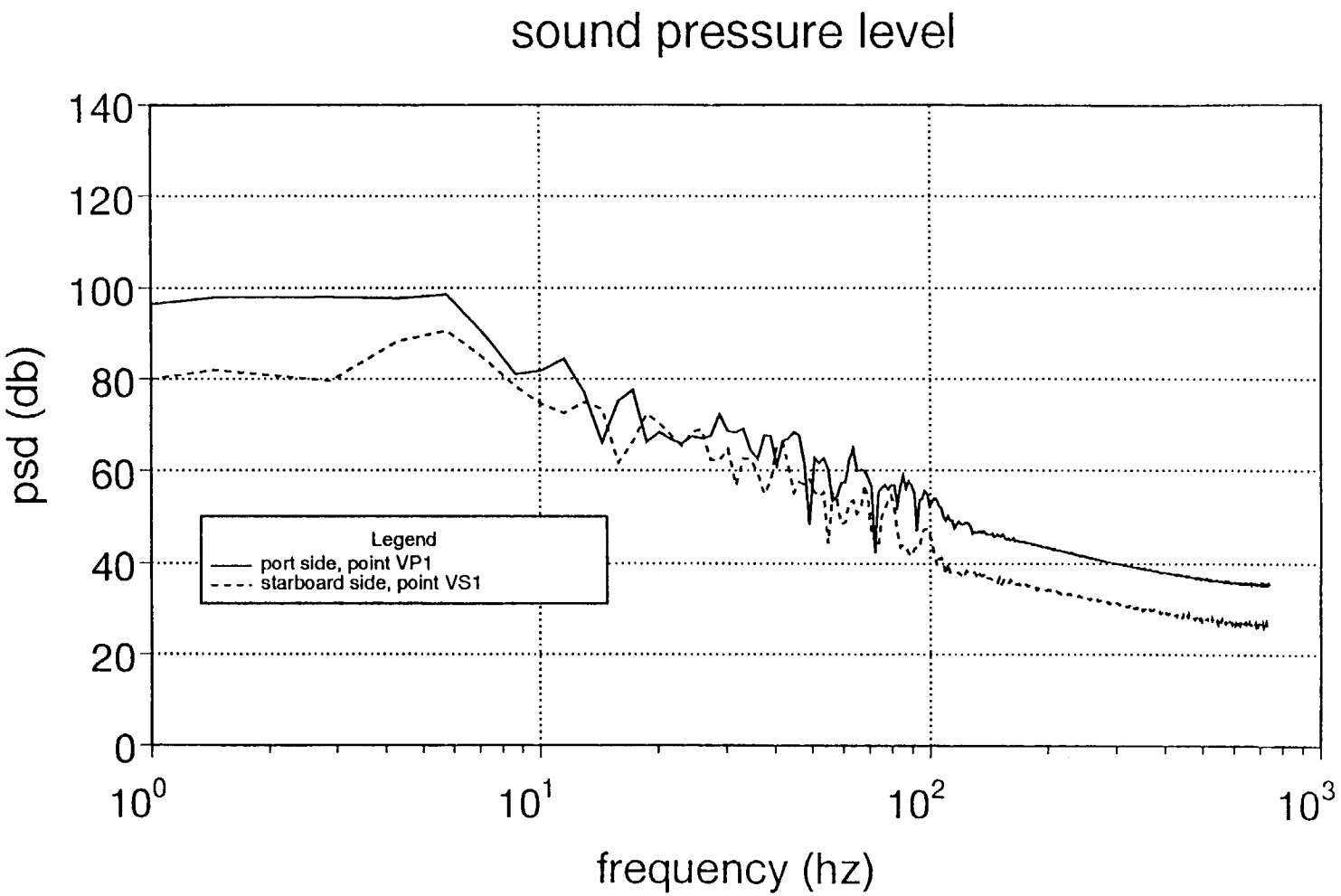

Fig. 32 Spectra of sound pressure levels at points VP1 and VS1 on the vertical stabilizer.

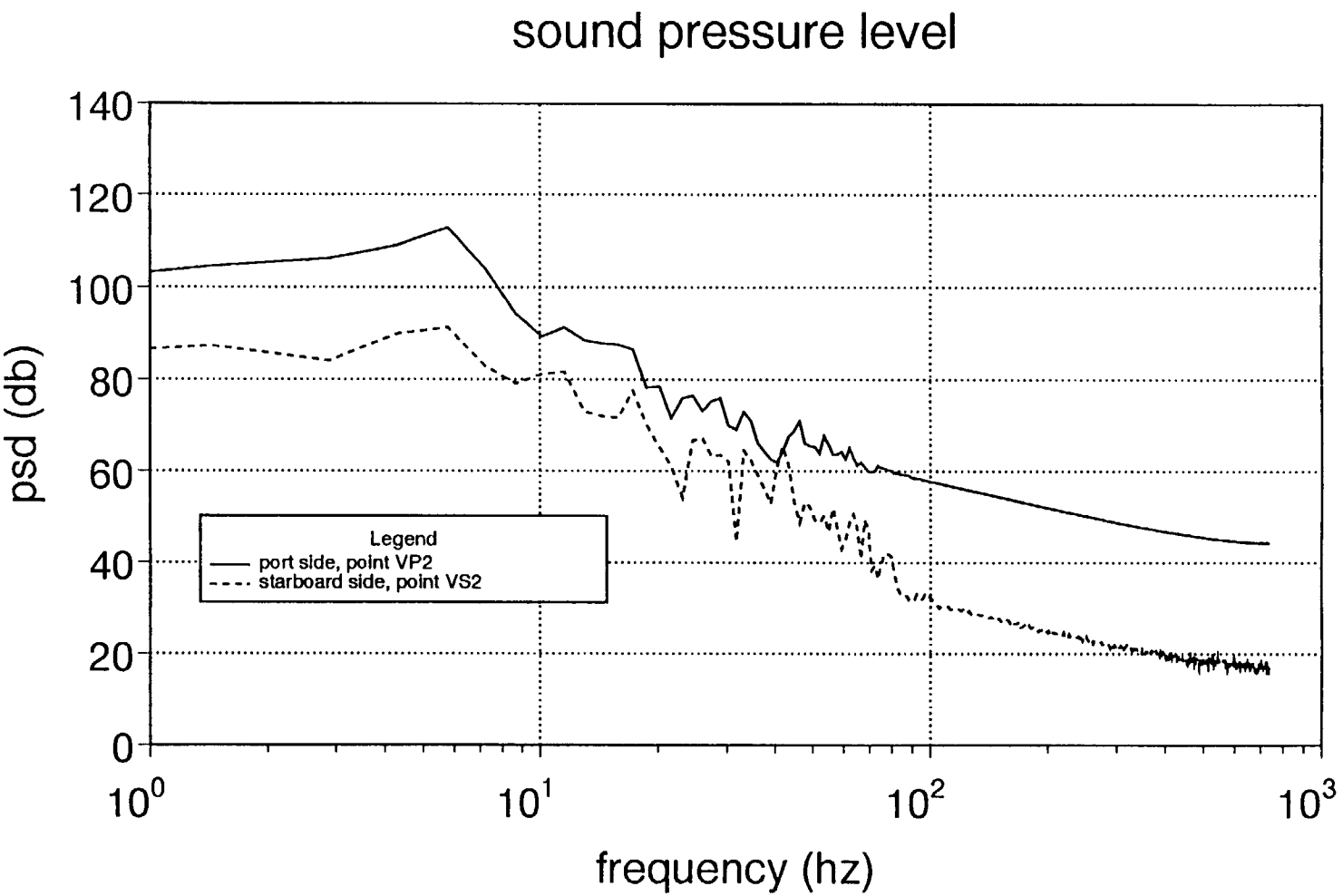

Fig. 33 Spectra of sound pressure levels at points VP2 and VS2 on the vertical stabilizer.

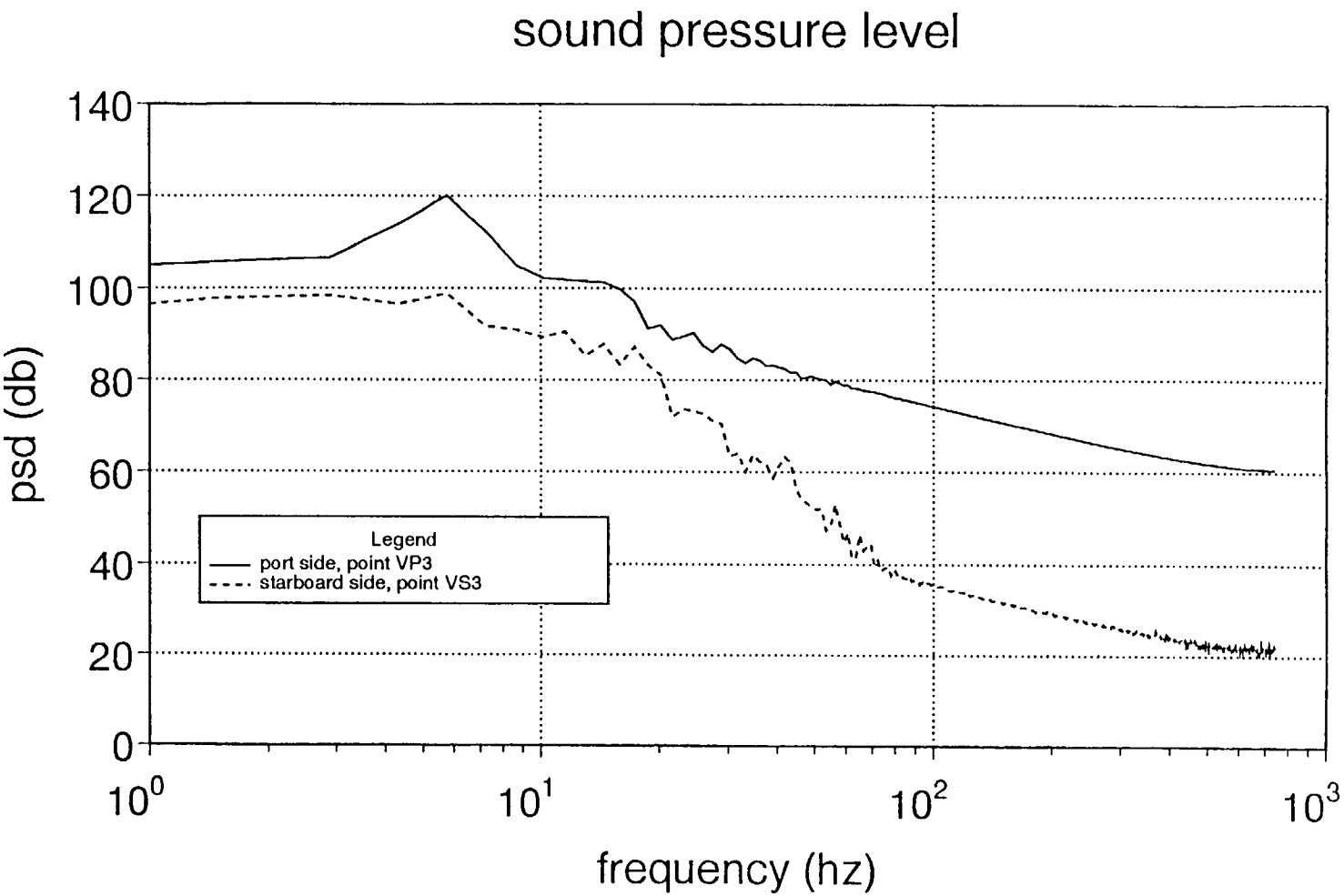

Fig. 34 Spectra of sound pressure levels at points VP3 and VS3 on the vertical stabilizer.

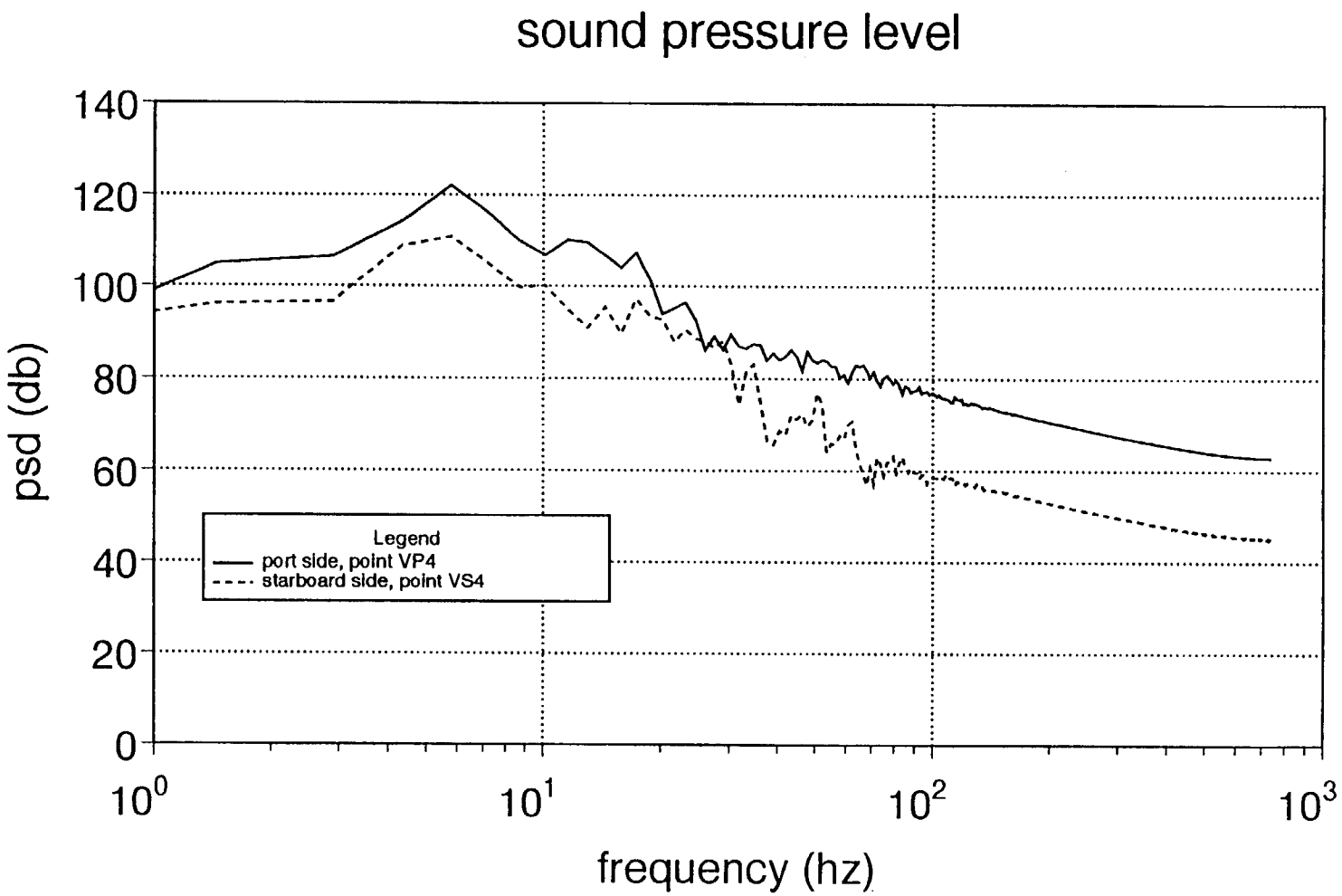

Fig. 35 Spectra of sound pressure levels at points VP4 and VS4 on the vertical stabilizer.

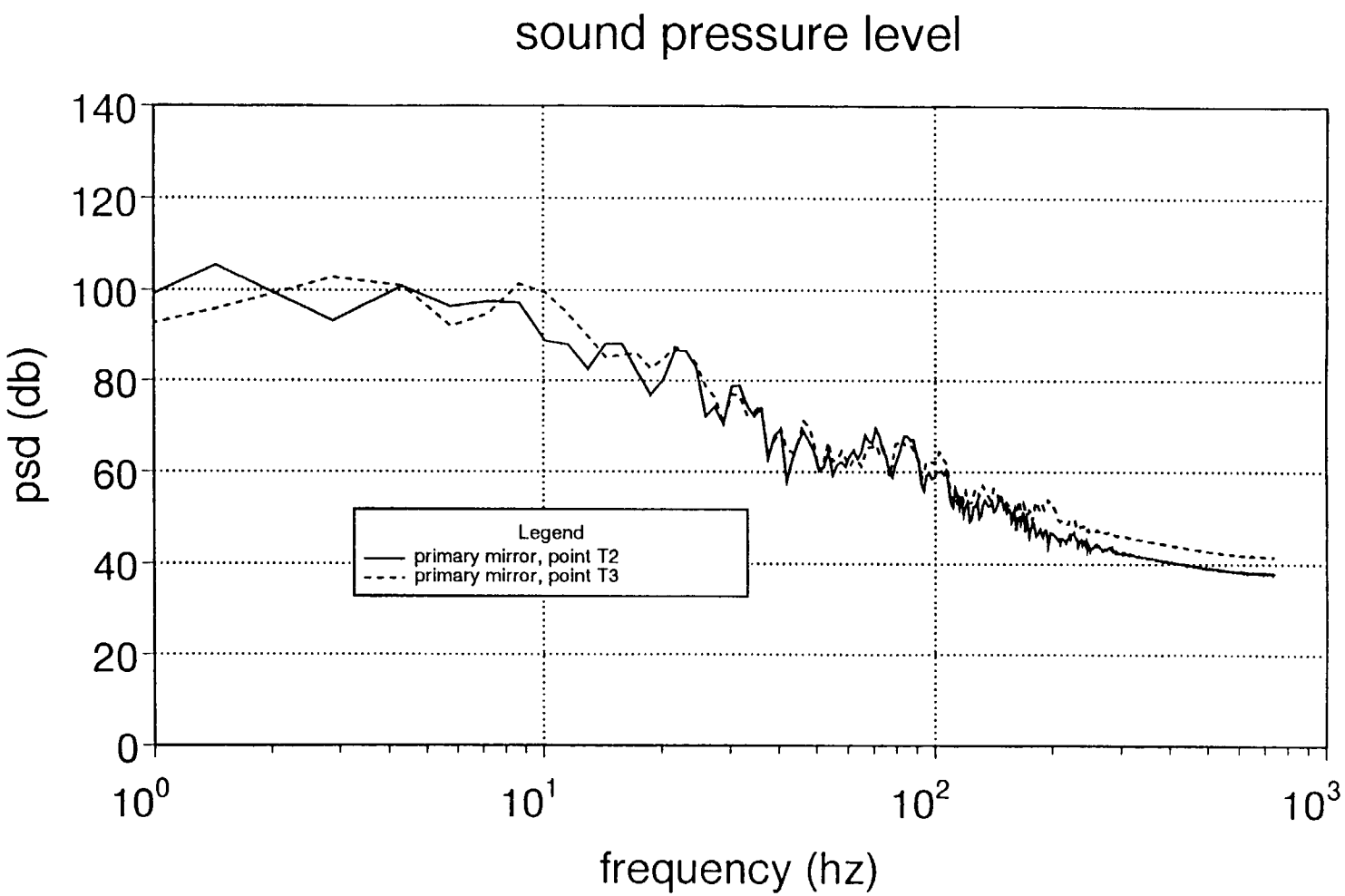

Fig. 36 Spectra of sound pressure levels at points T2 and T3 on the primary mirror of the telescope.

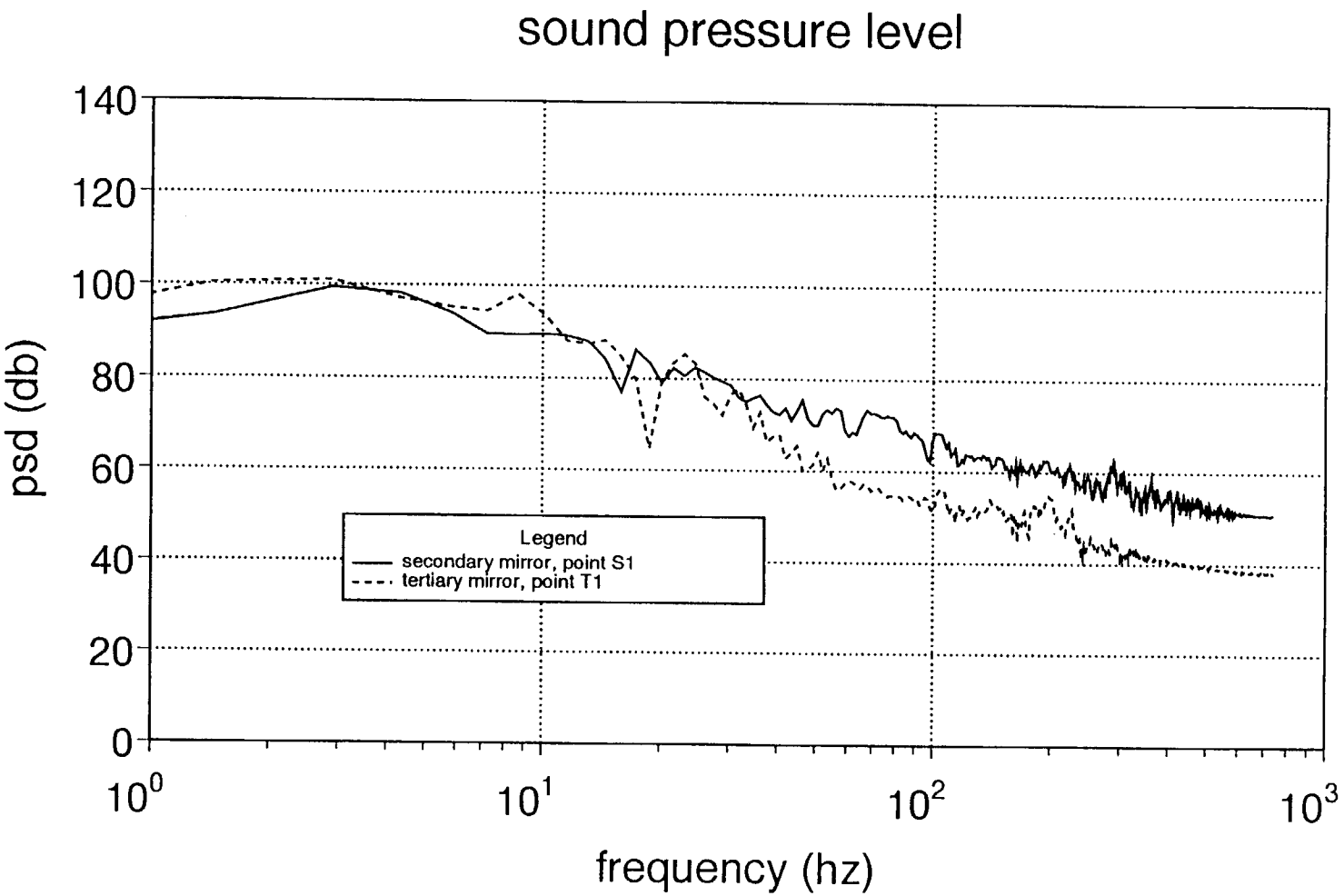

Fig. 37 Spectra of sound pressure levels at points S1 and T1 on the secondary and tertiary telescope mirrors, respectively.

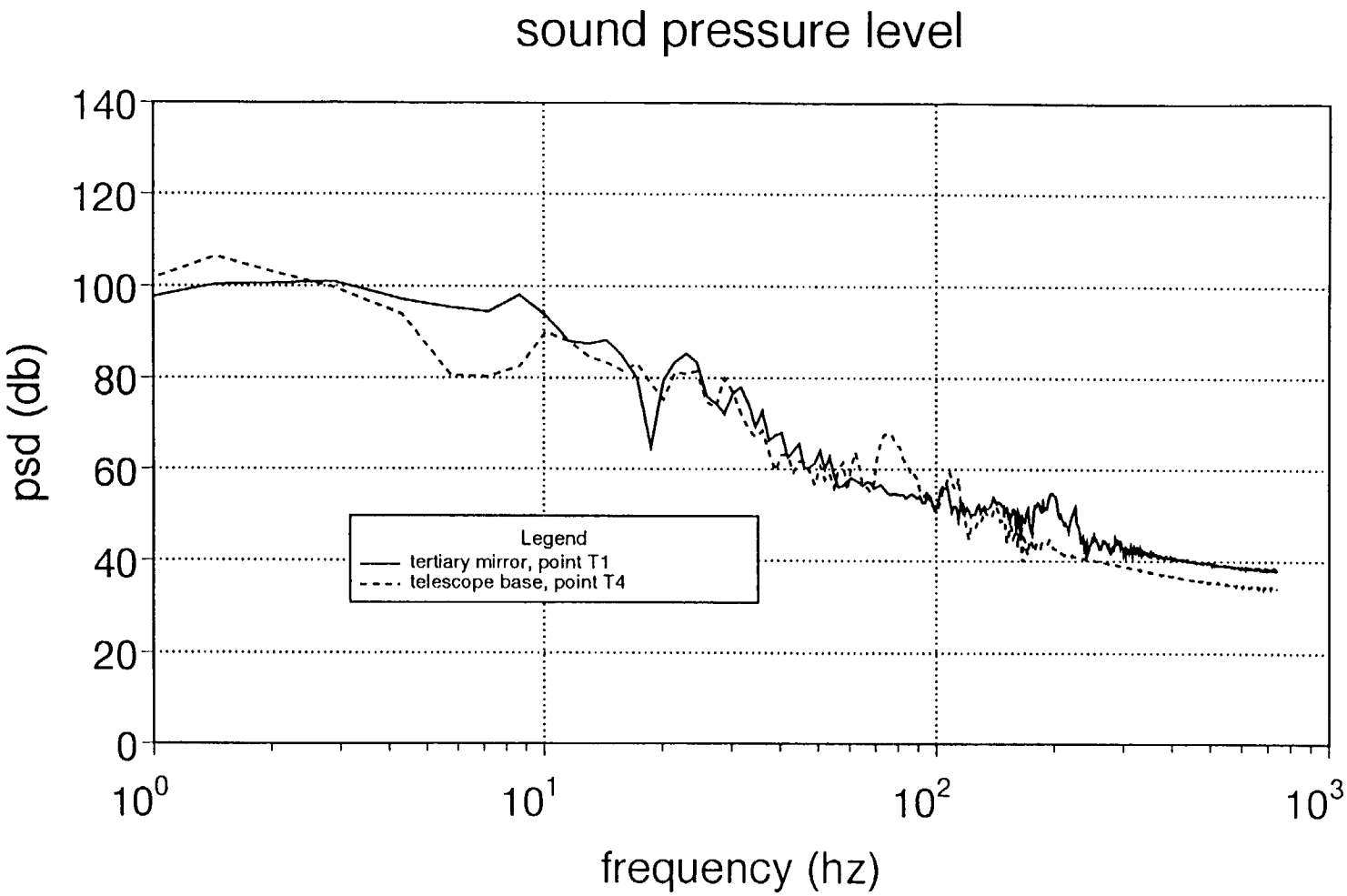

Fig. 38 Spectra of sound pressure levels at points T1 and T4 on the telescope.

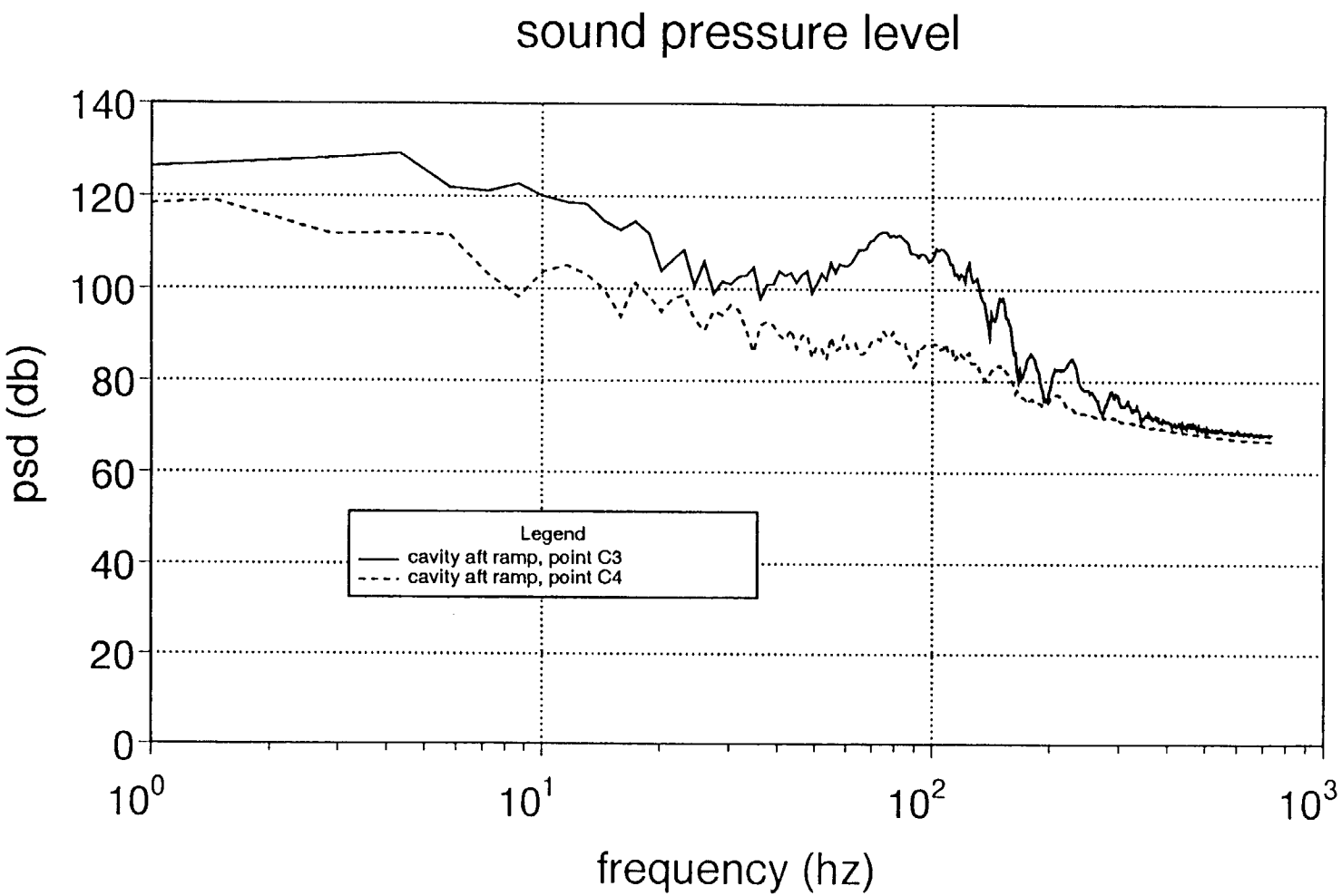

Fig. 39 Spectra of sound pressure levels at points C3 and C4 on the cavity aft ramp.

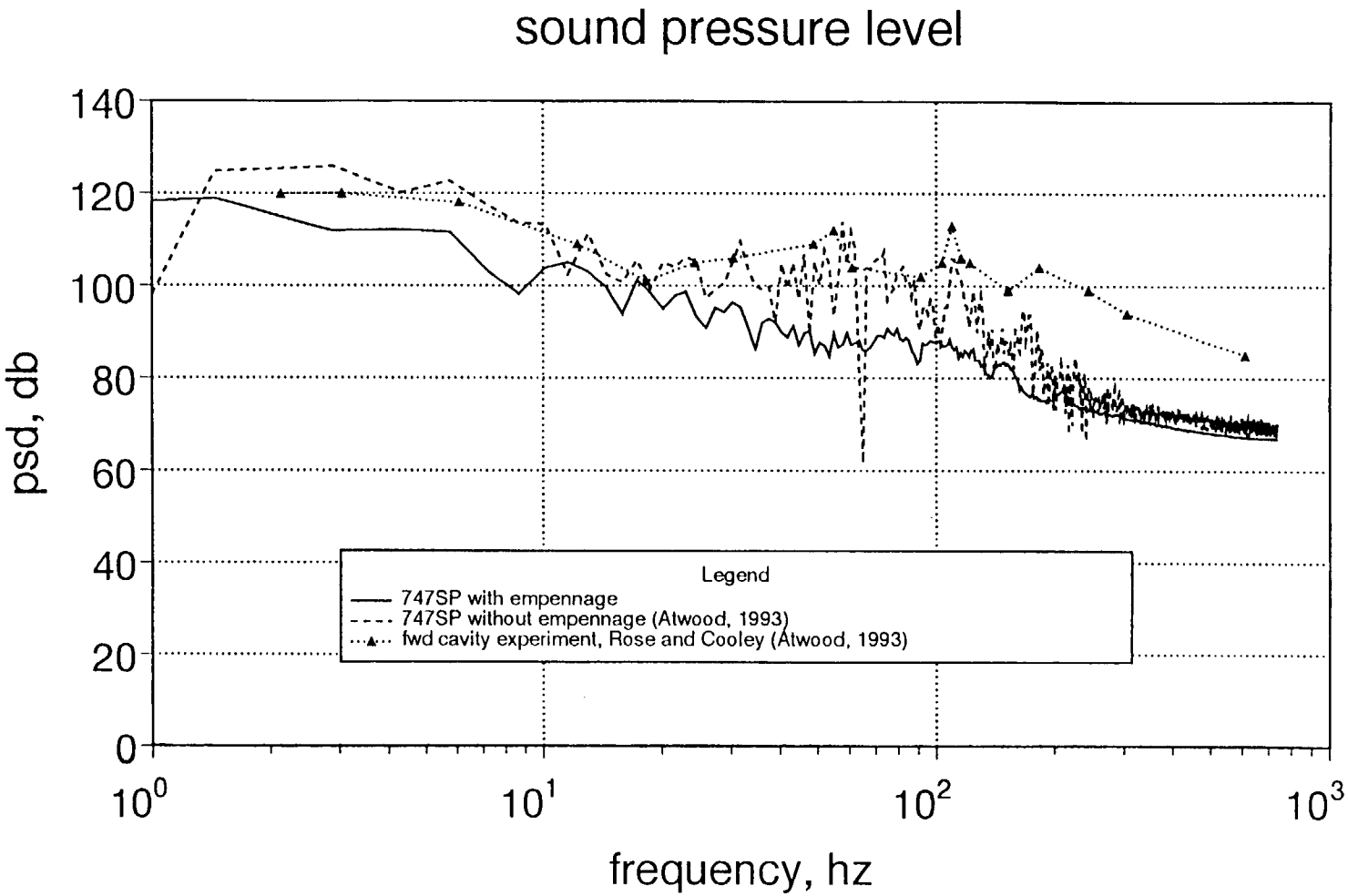

Fig. 40 Measured and computed spectra of sound pressure levels at point C4 on the cavity aft ramp.

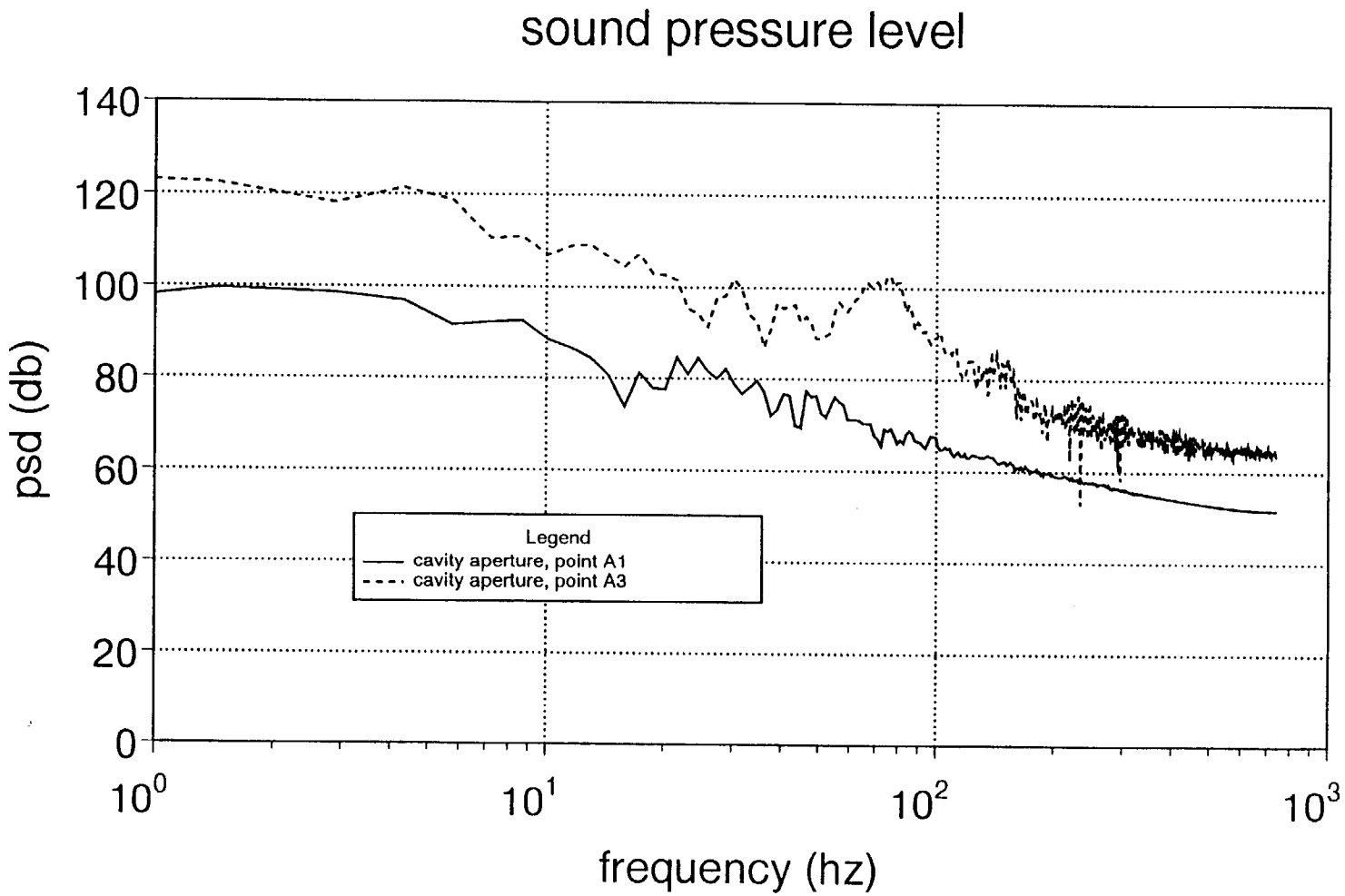

Fig. 41 Spectra of sound pressure levels at points A1 and A3 on the fuselage near the rim of the cavity.

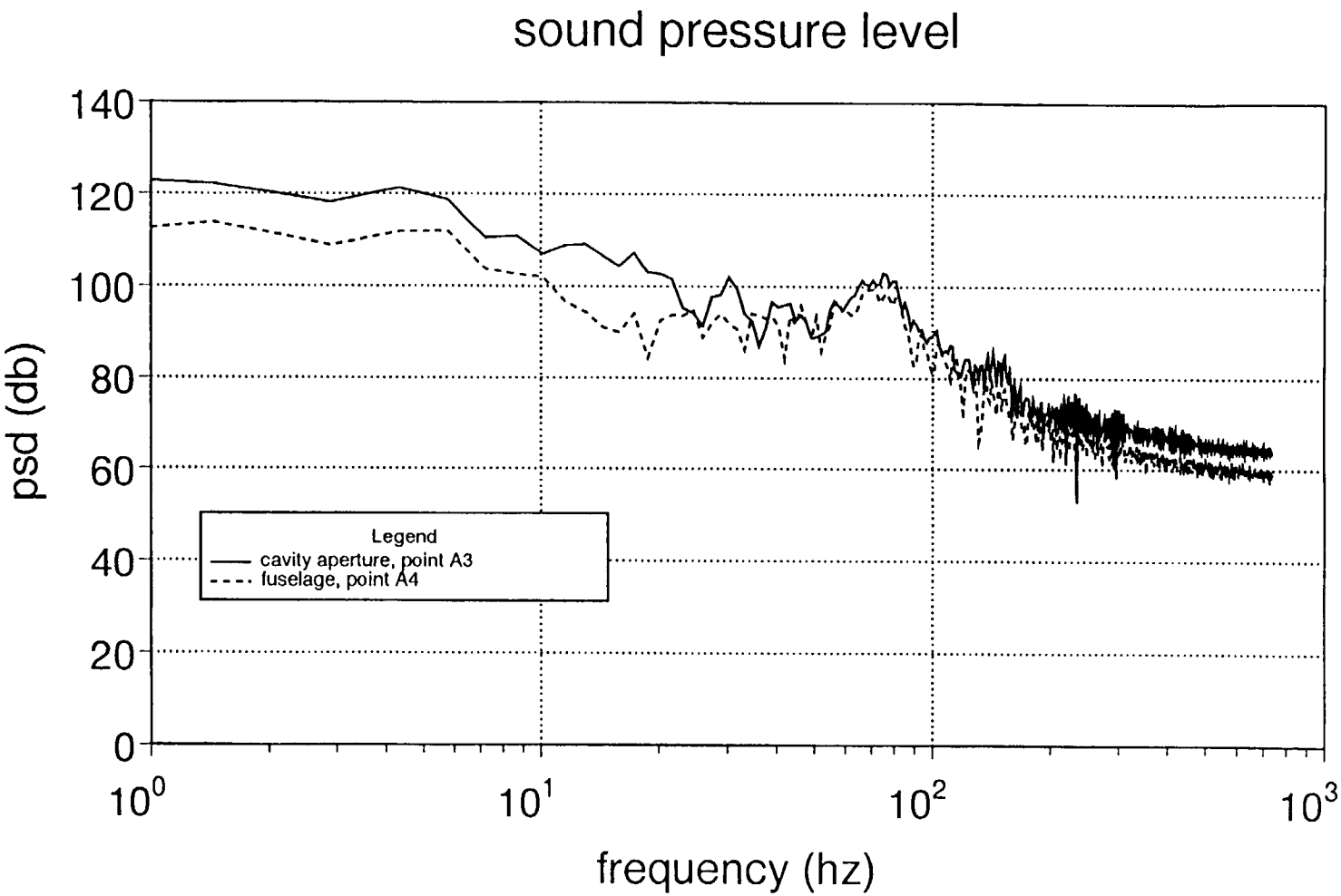

Fig. 42 Spectra sound pressure levels at points A3 and A4 on the fuselage downstream of the cavity.

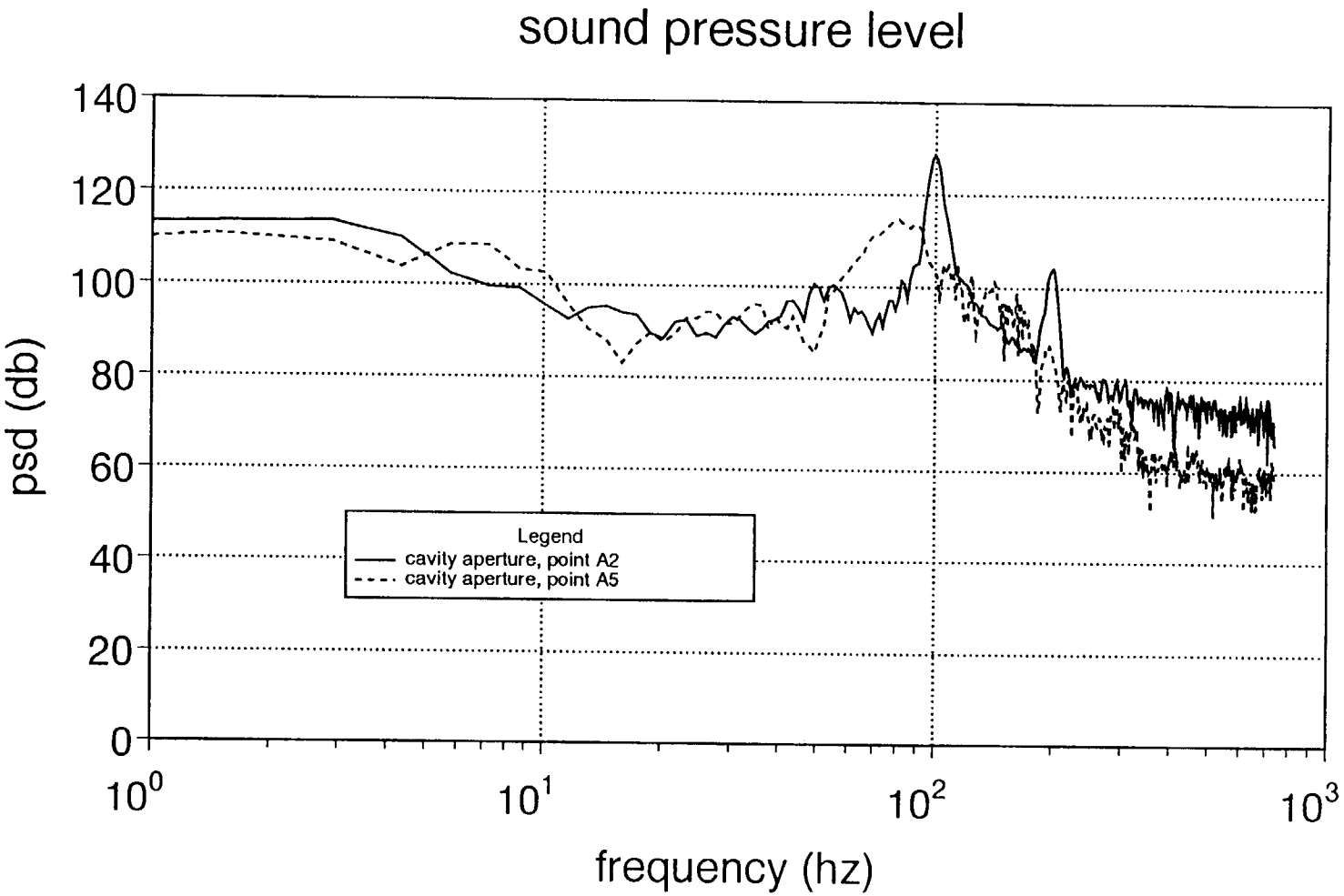

Fig. 43 Spectra of sound pressure levels at points A2 and A5 on the rim of the cavity.

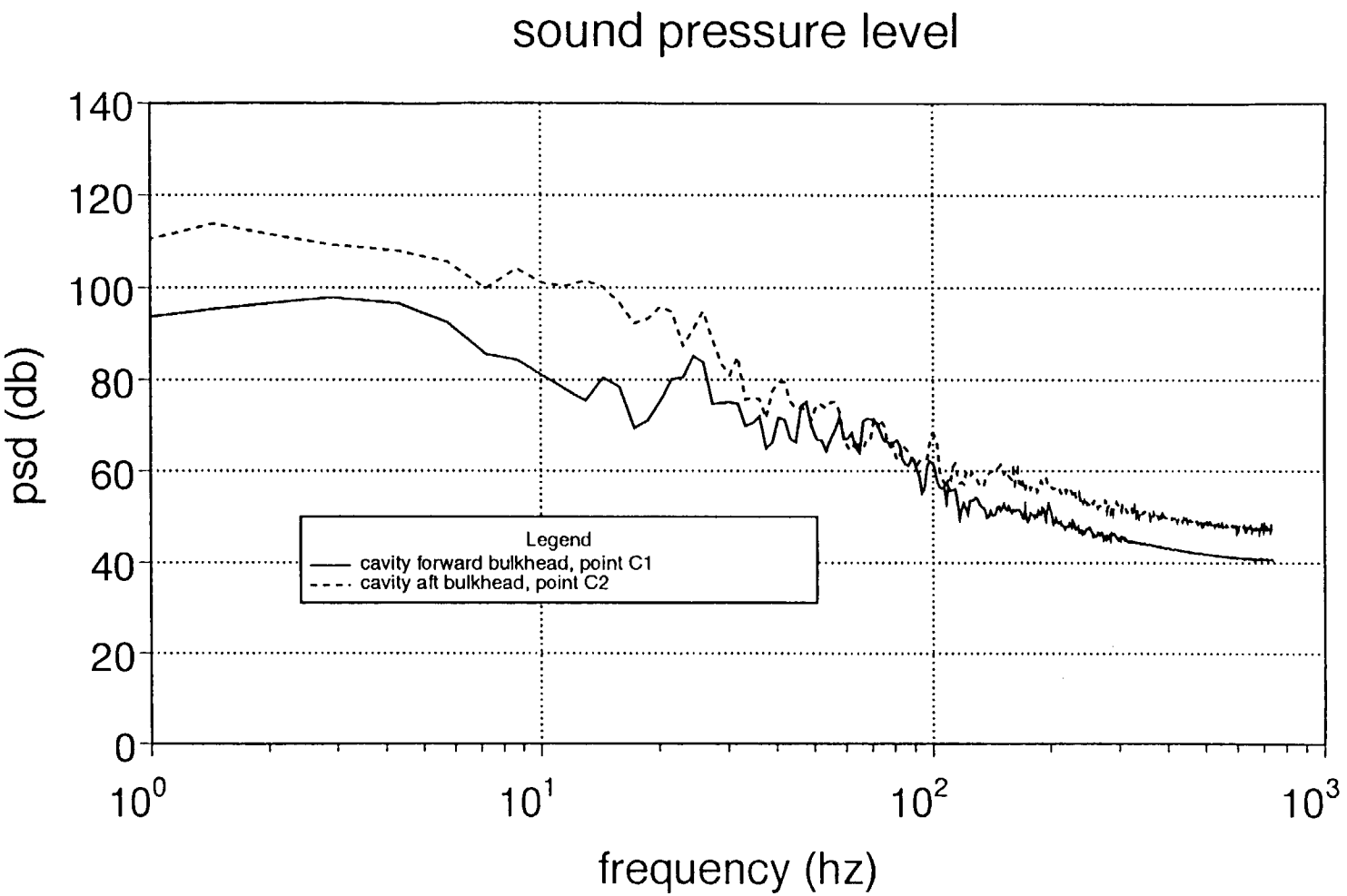

Fig. 44 Spectra of sound pressure levels at points C1 and C2 on the cavity forward and aft bulkheads, respectively.

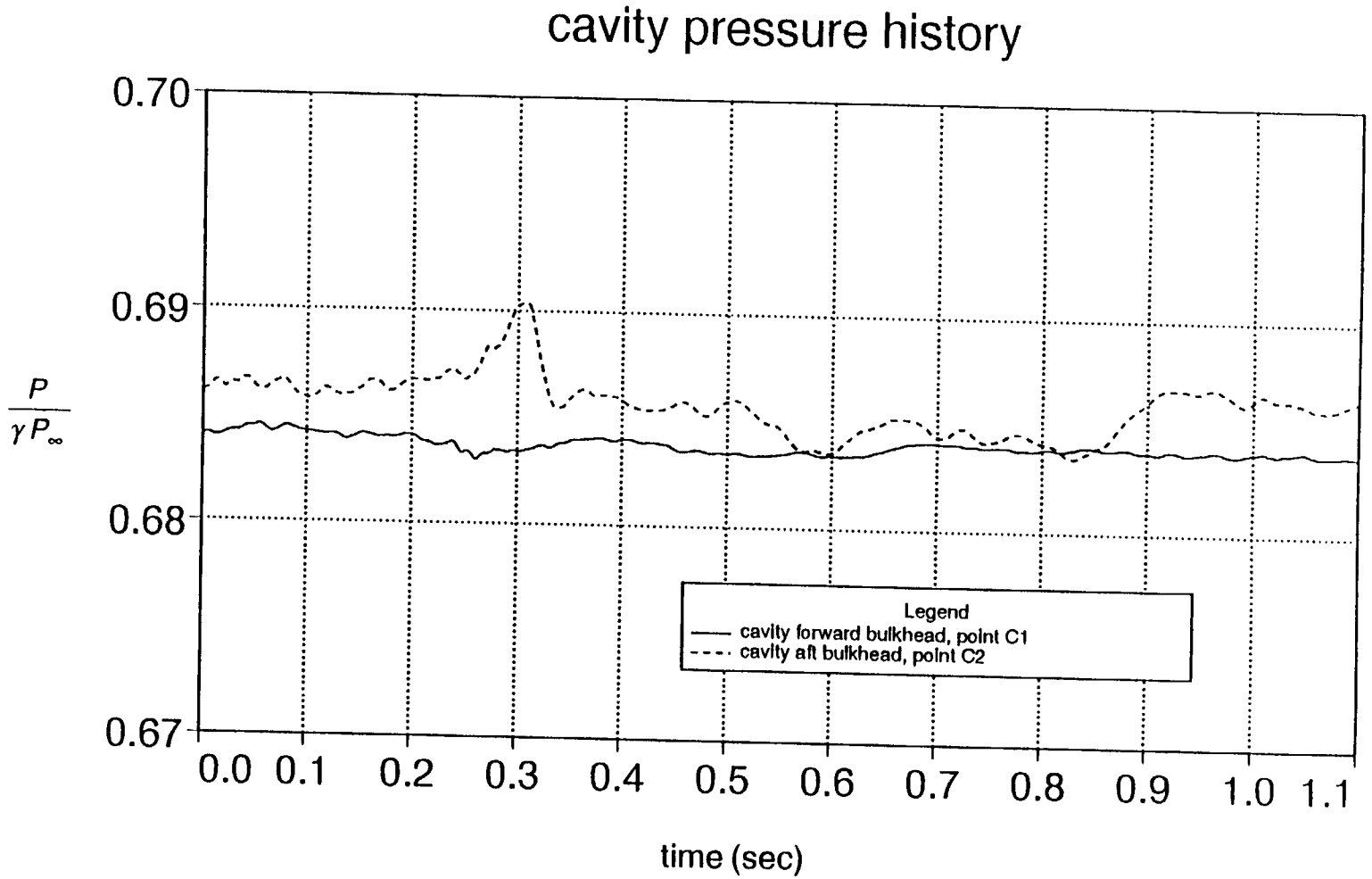

Fig. 45 Time histories of the normalized pressure at points C1 and C2 on the cavity bulkheads.

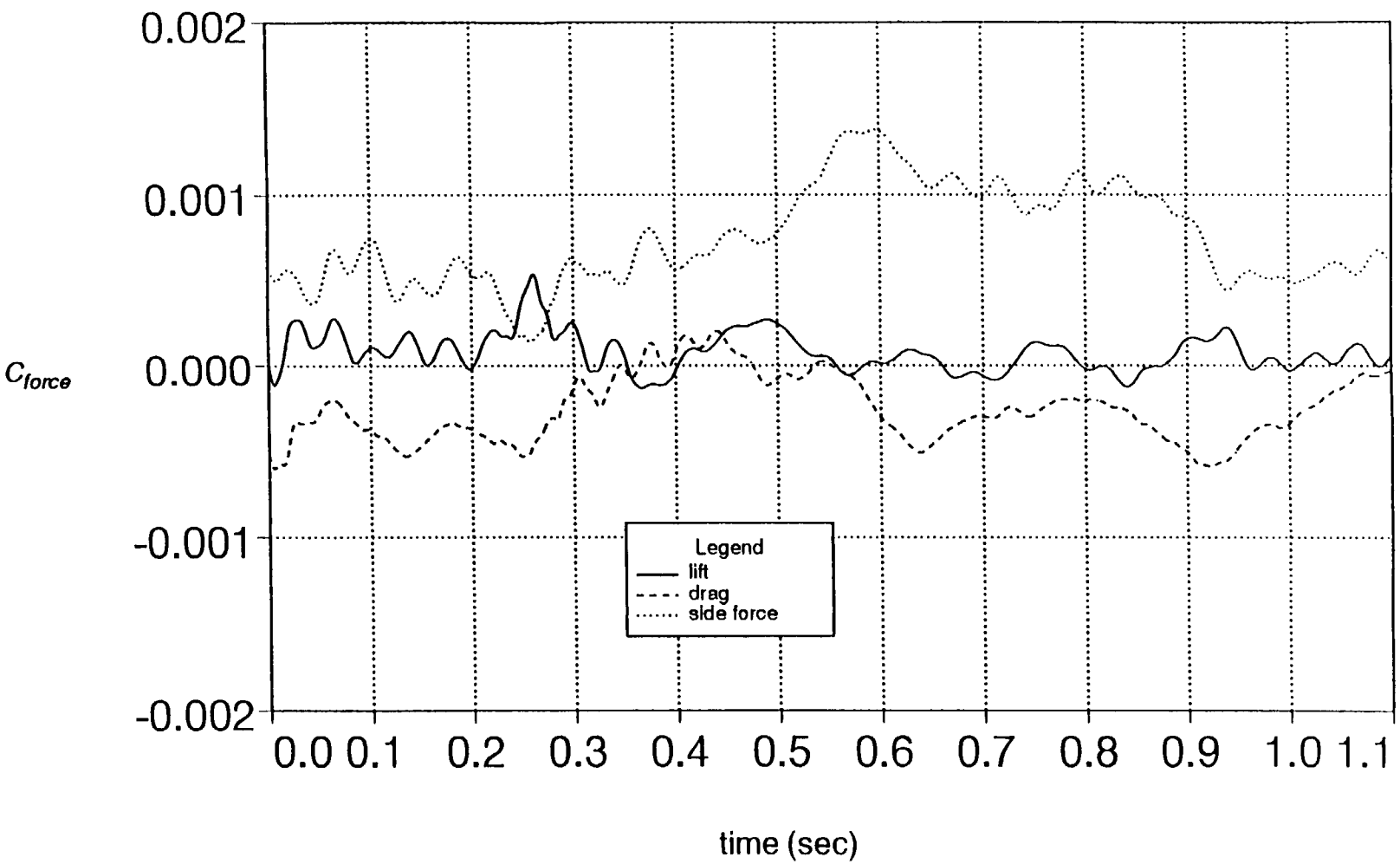

Fig. 46 Time histories of the telescope lift, drag, and side force coefficients.

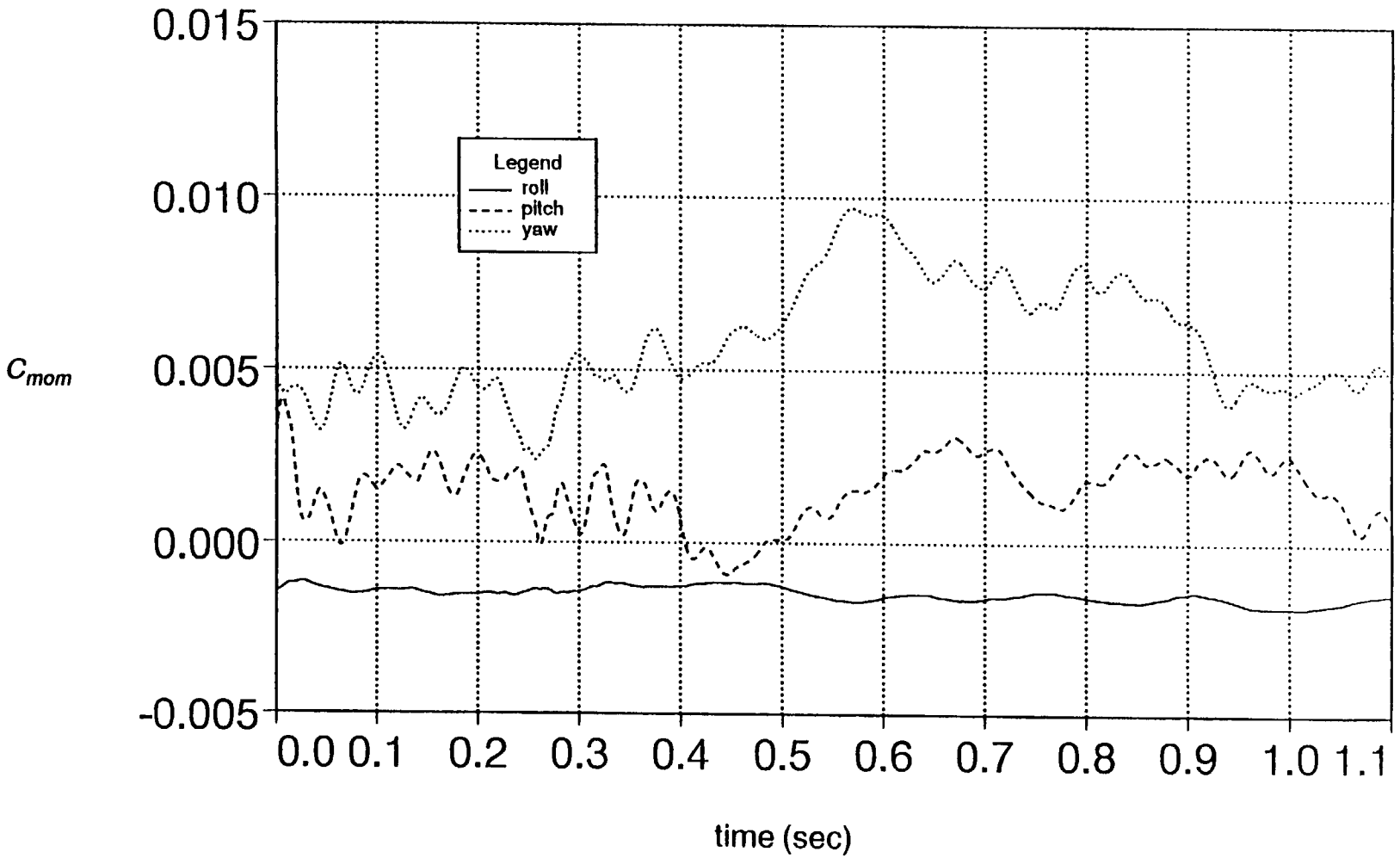

Fig. 47 Time histories of the telescope roll, pitch, and yaw coefficients.

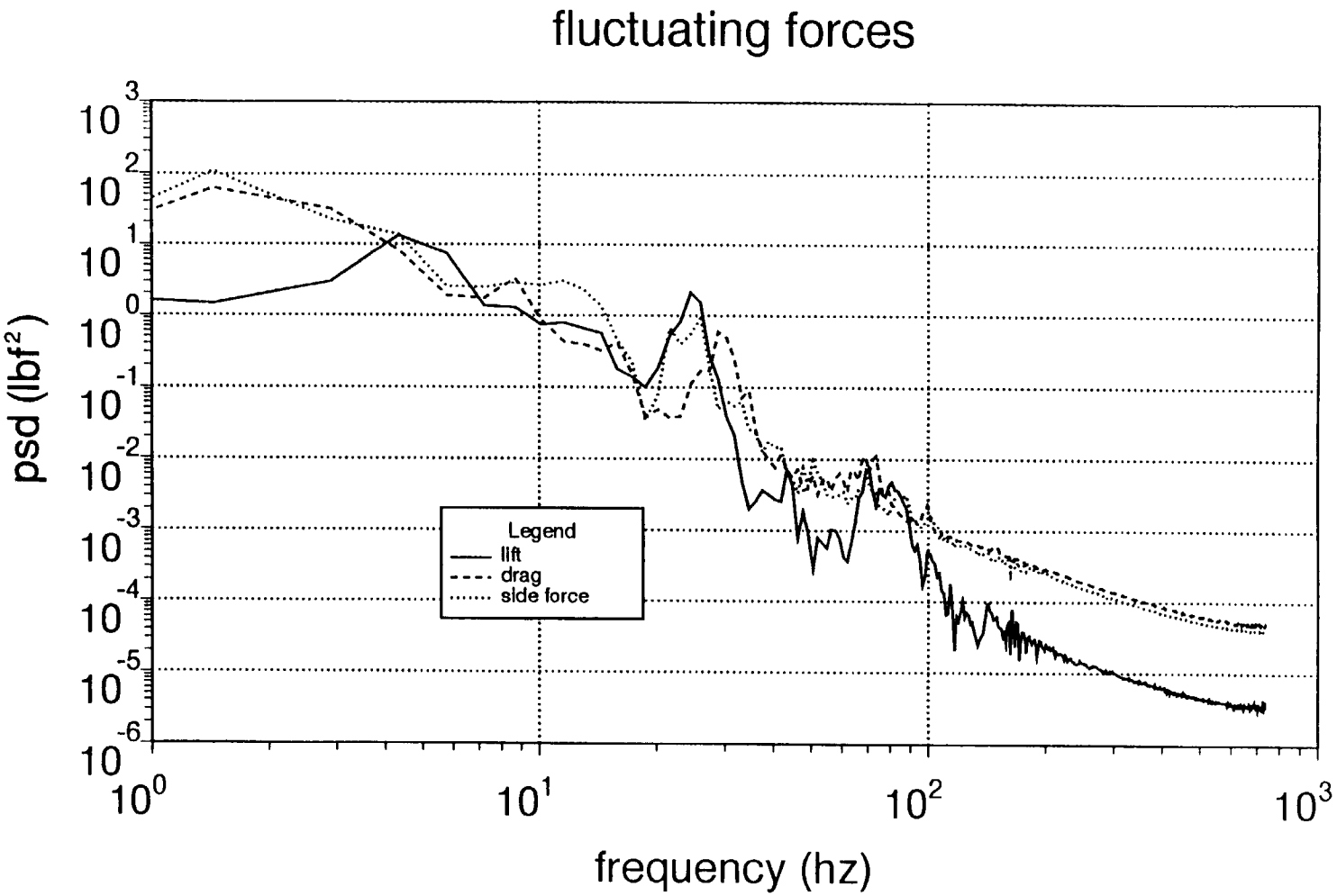

Fig. 48 Power spectra of telescope fluctuating forces.

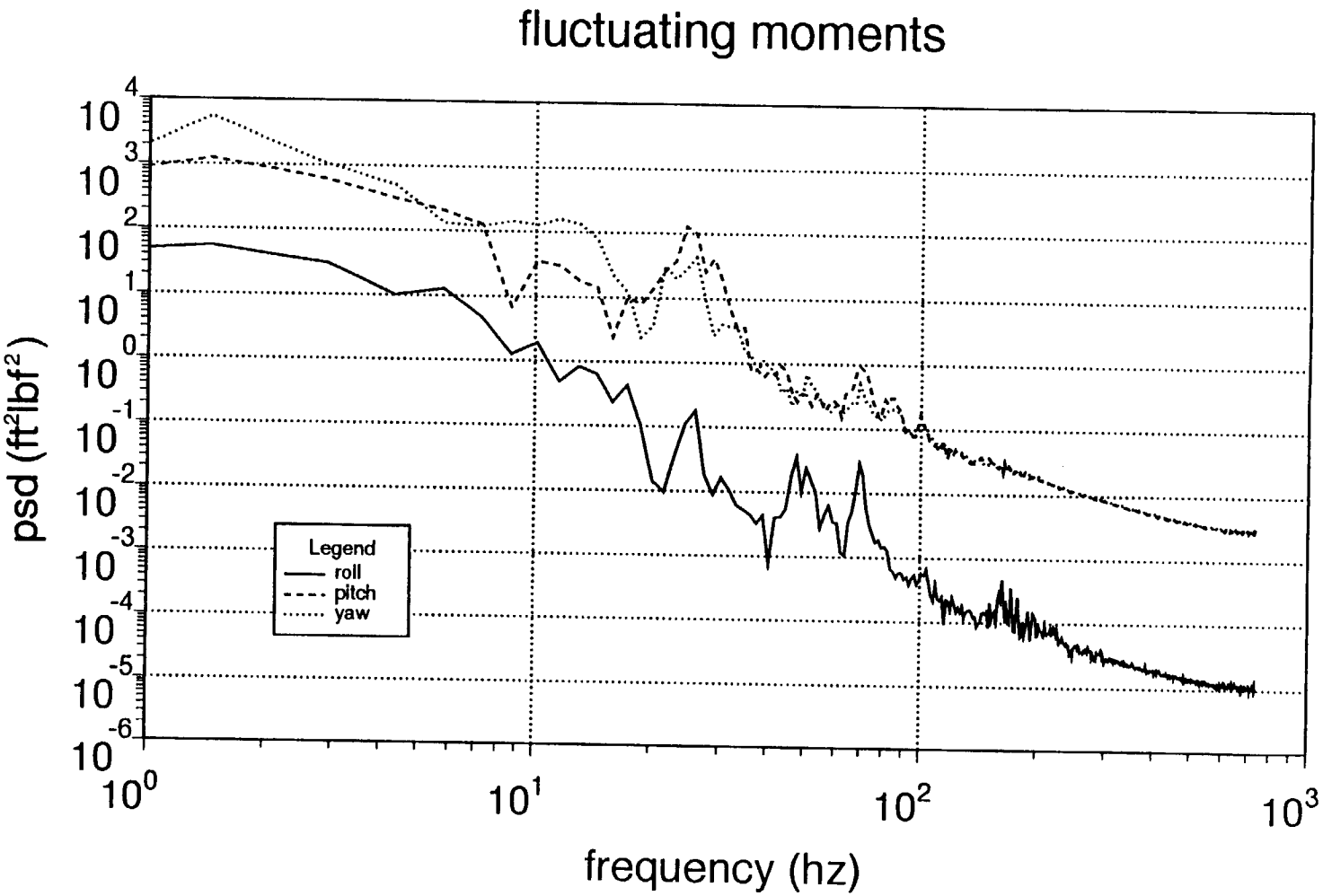

Fig. 49 Power spectra of telescope fluctuating moments.